

Slow Earthquakes: Tremor, Low-frequency Earthquakes and Slow Slip Events

Ariane Ducellier

A dissertation
submitted in partial fulfillment of the
requirements for the degree of

Doctor of Philosophy

University of Washington

2022

Reading Committee:

Kenneth C. Creager, Chair

David A. Schmidt

J. Michael Brown

Program Authorized to Offer Degree:

Earth and Space Sciences

© Copyright 2022

Ariane Ducellier

University of Washington

Abstract

Slow Earthquakes: Tremor, Low-frequency Earthquakes and Slow Slip Events

Ariane Ducellier

Chair of the Supervisory Committee:
Professor Kenneth C. Creager
Department of Earth and Space Sciences

The focus of this thesis is slow earthquakes, that is earthquake-like events that release energy over a period of hours to months, rather than the seconds to minutes characteristic of a typical earthquake. Slow slip events were discovered in many subduction zones during the last two decades thanks to recordings of the displacement of Earth's surface by Global Navigation Satellite Systems (GNSS) networks. As ordinary earthquakes, slow slip events are caused by slip on a fault (for instance, the plate boundary between a tectonic plate subducting under another tectonic plate). However, they take a much longer time (several days to several years) to happen relative to ordinary earthquakes, they have a relatively short recurrence time (months to years), compared to the recurrence time of regular earthquakes (up to several hundreds of years), and the seismic waves they generate are much weaker than the seismic waves generated by ordinary

earthquakes and may not be detectable. A slow slip event is inferred to happen when there is a reversal of the direction of motion at GNSS stations, compared to the inter-seismic motion of the surface displacement. In many places, tectonic tremor is also observed in relation to slow slip. Tremor is a long (several seconds to many minutes), low amplitude seismic signal, with emergent onsets, and an absence of clear impulsive phases. Tectonic tremor has been explained as a swarm of small, low-frequency earthquakes (LFEs), that is small magnitude earthquakes ($M \sim 1$) with frequency content (1-10 Hz) lower than for ordinary earthquakes (up to 20 Hz). Low-frequency earthquakes are usually grouped into families of events, with all the earthquakes of a given family originating from the same small patch on the plate interface and recurring more or less episodically in a bursty manner.

Due to the lack of clear impulsive phases in the tremor signal, it is difficult to determine the depth of the tremor source and the distance of the source to the plate interface with great precision. The thickness of the tremor region is also not well constrained. The tremor may be located on a narrow fault as the low-frequency earthquakes appear to be or distributed over a few kilometers wide low shear-wave velocity layer in the upper oceanic crust, which is thought to be a region with high pore-fluid pressure. In the second chapter of this thesis, I compute lag times of peaks in the cross-correlation of the horizontal and vertical components of tremor seismograms, recorded by small-aperture arrays in the Olympic Peninsula, Washington, and interpret them to be S minus P times. I estimate tremor depths from these S minus P times using epicenters from a previous study using a multibeam back-projection method. The tremor is located close to the plate boundary in a region no more than 2-3 kilometers thick and is very close to the depths of low-frequency earthquakes. The tremor is distributed over a wider depth range than the low-

frequency earthquakes. However, due to the uncertainty on the depth, it is difficult to conclude whether the source of the tremor is located at the top of the subducting oceanic crust, in the lower continental crust just above the plate boundary, or in a narrow zone at the plate boundary.

In the third chapter of this thesis, I extend the LFE catalog obtained by Plourde et al. (2015) during an episode of high tremor activity in April 2008, to the 8-year-long period 2004-2011. All of the tremor in the Boyarko et al. (2015) catalog south of 42 degrees North has associated LFE activity, but I have identified several other, mostly smaller, clusters of LFEs, and extend their catalog forward and backward by a total of about 3 years. As in northern Cascadia, the down-dip LFE families have recurrence intervals several times smaller than the up-dip families. For the April 2008 Episodic Tremor and Slip event, the best recorded LFE families exhibit a strong tidal Coulomb stress sensitivity starting 1.5 days after the rupture front passes by each LFE family. This behavior is very similar to what has been observed in northern Cascadia, even though the predicted Coulomb stress is about half the magnitude in the south. The southernmost LFE family, which has been interpreted to be on the subduction plate boundary, near the up-dip limit of tremor, has a very short recurrence time. Also, these LFEs tend to occur during times when predicted tidal Coulomb stress is discouraging slip on the plate boundary. Both observations suggest this LFE family may be on a different fault, perhaps a crustal fault.

In many places, tectonic tremor is observed in relation to slow slip and can be used as a proxy to study slow slip events of moderate magnitude where surface deformation is hidden in GNSS noise. However, in places where no clear relationship between tremor and slow slip occurrence is observed, these methods cannot be applied, and we need other methods to be able to better detect

and quantify slow slip. In the fourth chapter of this thesis, I use the Maximal Overlap Discrete Wavelet Transform (MODWT) to analyze GNSS time series and seismic recordings of slow slip events in Cascadia. I use detrended GNSS data, apply the MODWT transform and stack the wavelet details from several neighboring GNSS stations. As an independent check on the timing of slow slip events, I also compute the cumulative number of tremors in the vicinity of the GNSS stations, detrend this signal, and apply the MODWT transform. I then assume that there is a transient, interpreted as a slow slip event, whenever there is a positive peak followed by a negative peak in the wavelet signal. I verify that there is a good agreement between slow slip events detected with only GNSS data, and slow slip events detected with only tremor data. The wavelet-based detection method detects well events of magnitude higher than 6 as determined by independent event catalogs (Michel et al., 2019).

Acknowledgements

I would like to thank my advisor Kenneth Creager for making me discover the fascinating world of tremor, low-frequency earthquakes and slow slip events. It has been wonderful to spend the last five years working on such an exciting research topic. I also would like to thank my PhD committee: David Schmidt, Michael Brown and Aleksandr Aravkin, for their advice and feed-back throughout my PhD studies.

I would like to thank Donald Percival for introducing me to wavelet methods for time series analysis. Without the class that he taught in Spring 2018, the last chapter of this dissertation would not exist. I am grateful for all the resources provided by University of Washington, in particular the eScience Institute, the Winter Incubator program and Scott Henderson, the Integral Big Data Research Fund of the College of the Environment, and the Research Computing Club.

I would like to thank Hormoz Modaressi, without whom I would never have discovered seismology. I also would like to thank Hideo Aochi and Hiroshi Kawase, with whom I wrote my first research papers.

I would like to thank the staff members of the Department of Earth and Space Sciences, in particular Noéll Bernard-Kingsley, Eunice Yang and Kathy Gabriel, for helping me navigate all sorts of administrative questions. I would like to thank Ellen Reynolds from the Department of Statistics for helping me applying to and graduating with an MSc in Statistics in parallel to my PhD studies.

I would like to thank all the people who helped put in place the new data science option just in time for my graduation.

I would also like to thank Thomas Richardson and Daniela Witten for their support throughout my graduate studies.

Finally I would like to thank my family: my husband Zaïd for his constant love and support during all these years of graduate school, my parents and particularly my mother for all the help she gave me when our children were born, when I took my general exam and when I wrote the final parts of this dissertation, and my children Giselle and Michel for all the joy they bring into our lives. I also would like to thank the staff of UW Children Center at Laurel Village for their dedication in providing child care in all circumstances.

Contents

Acknowledgements	i
1 Introduction	1
2 Depth and thickness of tectonic tremor in the northeastern Olympic Peninsula	7
2.1 Introduction	8
2.2 Data	12
2.3 Method	12
2.4 Results	16
2.5 Discussion	19
2.6 Conclusion	26
3 An eight-year-long low-frequency earthquake catalog for Southern Cascadia	31
3.1 Introduction	32
3.2 Data	34
3.3 Method	34
3.4 Results	38
3.5 Discussion	40
3.6 Conclusion	45
4 Detection of slow-slip events using wavelet analysis of GNSS recordings	47
4.1 Introduction	48
4.2 Data	50
4.3 Method	51
4.3.1 The Maximal Overlap Discrete Wavelet Transform	51
4.3.2 Application to synthetic data	52
4.3.3 MODWT of GPS and tremor data	54
4.4 Results	58
4.5 Discussion	61
4.6 Conclusion	67
5 Perspectives	69
A Supplement for Chapter 2	71
B Supplement for Chapter 3	81
Bibliography	87

List of Figures

2.1	Map of the Array of Arrays	13
2.2	Envelopes of cross-correlations for a single grid cell	14
2.3	Stacks of the cross-correlations for the two clusters	17
2.4	Stacks of envelopes for the Big Skidder array	18
2.5	Map of the uncertainty on the depth of the source of the tremor	20
2.6	Map of the depth of the source of the tremor	21
2.7	Cross-sections of the locations of the source of the tremor	22
2.8	Map of the distance to the plate boundary of the source of the tremor	23
2.9	Differences in S-minus-P times	25
2.10	Variations of the depth of the source of the tremor	26
2.11	Map of the thickness of the tremor layer	27
2.12	Map of the residuals from a linear regression	28
3.1	Location of the LFE families	35
3.2	Cross-correlation values	36
3.3	LFE and tremor detections as a function of time and latitude	37
3.4	LFE template for station WDC and family A	38
3.5	Normalized cumulative number of LFEs	39
3.6	LFE and tremor detections as a function of time and latitude	40
3.7	LFE and tremor detections for six ETS events	41
3.8	Daily number of LFEs for several families	43
3.9	Average time between LFE clusters as a function of distance	44
3.10	Number of LFEs for each stress bin of tidal Coulomb stress change	46
4.1	MODWT of synthetic time series	53
4.2	MODWT with missing values	55
4.3	MODWT for station PGC5	56
4.4	Map of tremor and GPS stations	57
4.5	MODWT of the cumulative tremor count	59
4.6	8th level detail of the MDWT of the displacement and the tremor count	60
4.7	7th level detail of the MDWT of the displacement and the tremor count	62
4.8	6th level detail of the MDWT of the displacement and the tremor count	63
4.9	ROC curve of the slow-slip event detector	65
4.10	Sum of the 6th, 7th and 8th level details of the MDWT	66
4.11	5th level detail of the MDWT of the displacement	68
A.1	Stacks of envelopes for the Burnt Hill array	73
A.2	Stacks of envelopes for the Cat Lake array	74
A.3	Stacks of envelopes for the Danz Ranch array	75
A.4	Stacks of envelopes for the Gold Creek array	76
A.5	Stacks of envelopes for the Lost Cause array	77
A.6	Stacks of envelopes for the Port Angeles array	78
A.7	Stacks of envelopes for the Three Bumps array	79

A.8	Variations of the time lags of the time windows for a single grid cell	80
B.1	LFE and tremor detections as a function of time and latitude	82
B.2	LFE and tremor detections as a function of time and latitude	82
B.3	Evolution of the number of channels available	83
B.4	Evolution of the number of channels available	83

List of Tables

2.1	Summary of distances to the plate boundary	29
3.1	Main LFEs episodes between 2004 and 2011	41
3.2	Nearby regional earthquakes between 2004 and 2011	41
3.3	Teleseismic earthquakes between 2004 and 2011	42
4.1	M > 6 events identified by MODWT	61
4.2	Magnitude 5 slow-slip events	67
A.1	Depths, thicknesses and S-to-P time lags	71
B.1	Temporary stations used for the 2007-2009 catalog	81
B.2	Permanent stations used for the 2004-2011 catalog	84
B.3	Thresholds used to clean the catalogs	85

Dedicated to my mother ...

Chapter 1

Introduction

The largest earthquakes on Earth occur in subduction zones, where large segments of the boundary between the subducting tectonic plate and the overlying plate can store energy for centuries and then release it in minutes during an earthquake. To better assess seismic hazard, it is thus necessary to improve our understanding of subduction zone processes. Following the 1995 Kobe earthquake, the Japanese government has invested in the deployment of large earthquake monitoring networks, in particular the high-sensitivity seismograph network Hi-net. In the following years, a new generation of dense and sensitive networks has been deployed around the world, including densely spaced seismic networks, high-sensitivity borehole seismometer arrays and continuously recording Global Navigation Satellite System (GNSS) networks. The large amount of earthquake-related data made available by these instruments has led to the discovery of a large new class of earthquake-like phenomena (e.g. slow-slip events, tectonic tremor, low-frequency earthquakes, very low-frequency earthquakes) all around the world (Beroza and Ide, 2011).

Slow-slip events were first observed in the late 1990s. Hirose et al. (1999) observed anomalies in the GPS data in the Bungo Channel region, southwest Japan. They modeled them as a slow thrust slip event lasting about three hundred days from March to December 1997. Although two magnitude 6.7 earthquakes occurred nearby in October and November 1996, the slow thrust slip event was located two hundred kilometers from the epicenters, close to the downdip extent of the rupture area of the 1946 Nankaido earthquake. The slip velocity was about 10^{-6} mm/s, much lower than the previous slow earthquakes discussed by Beroza and Jordan (1990). Slow-slip events were first observed in Cascadia by Dragert, Wang, and James (2001). During summer 1999, they observed a reversal of the horizontal displacement measured at seven GNSS stations in northern Cascadia of about two to four millimeters and lasting six to fifteen days. They explained this displacement by aseismic slip on the subduction interface equivalent to an earthquake of moment magnitude 6.7. No seismic activity was observed at the time. Miller et al. (2002) then observed eight slow-slip events recorded by GNSS stations between 1992 and 2002. These slow-slip events occurred along the plate interface more or less regularly every fourteen months. Since then, slow-slip events have been observed in many places, such as Cascadia, Nankai, Alaska, Costa Rica, Mexico, and New Zealand (Beroza and Ide, 2011; Audet and Kim, 2016). Two of their main characteristics are that they take a *much longer time* (several days to several years) to happen relative to ordinary earthquakes and they have a relatively *short recurrence time* (months to years) compared to the recurrence time of regular earthquakes (up to several hundreds of years).

Non-volcanic tremor were first observed in southwest Japan by Obara (2002).

He identified simultaneously at several seismic stations a low amplitude signal lasting from a few minutes to a few days, with predominant frequency ranging from one to ten Hertz, and without clear P- or S-wave onsets. The source of the tremor was distributed along the strike of the plate boundary over a length of six hundred kilometers extending from the Tokai area to the Bungo channel, at about thirty kilometers depth. Volcanic tremor has been known to occur in magmatic systems for decades and the term tectonic tremor is often used to distinguish tremor not related to volcanic systems from volcanic tremor. Tremor has since been reported in many subduction zones (Nankai, Cascadia, Mexico, Alaska, Costa Rica, Aleutian Islands, New Zealand), inland convergent areas (Taiwan) and along the San Andreas Fault (Ide, 2012). Tremor propagates in the strike direction at about ten kilometers per day during several weeks. Rapid reversals of the direction of the propagation of the tremor are also reported, with tremor reversal lasting a few hours and propagating at about ten kilometers per hour (Houston et al., 2011). Faster migration also occurs in the updip and downdip directions of the slab at about twenty-five to one hundred and fifty kilometers per hour over distances up to twenty kilometers (Shelly, Beroza, and Ide, 2007a; Ghosh et al., 2010b). The polarization direction of tremor recordings in Cascadia suggests that tremor represents shear slip on the plate interface (Wech and Creager, 2007).

Finally, Rogers and Dragert (2003) observed tectonic tremor in conjunction with slow-slip events in Cascadia. The tremor like signals correlated temporally and spatially with six deep slip events occurring between 1996 and 2003. As in Japan, the frequency content of the signal was mainly between one and five Hertz. The tremor migrated along the strike of the plate boundary at a speed of about five to fifteen kilometers per day, the source of the tremor was about twenty to forty kilometers depth, and the duration of the tremor activity in any one region was about ten to twenty days. Rogers and Dragert (2003) called this simultaneous tremor episodes and slow-slip events Episodic Tremor and Slip (ETS). It was later shown by Obara et al. (2004) than ETS are also occurring in southwest Japan, where they observed tilt deformation coincident with major tremor activity, and recurring approximately every six months.

Low-frequency earthquakes (LFEs) are small magnitude earthquakes, with typical magnitude less than 2, and reduced amplitudes at frequencies greater than ten Hertz relative to ordinary small earthquakes. They have been included in the seismicity catalog of the Japan meteorological Agency since 1999 (Katsumata and Kamaya, 2003). They were first detected in the Tokai and Kii regions of the Nankai Trough but have been seen detected in many regions around the world, in correlation with tectonic tremor. Using waveform cross-correlation, Shelly et al. (2006) have relocated LFEs in western Shikoku, Japan, and concluded that the source of the LFEs was located on a dipping plane five to eight kilometers above, and parallel to the lower part of the oceanic crust, where most of the intra-slab seismicity occurs. As many similar LFE events originate from the same location on the plate interface, they produce similar waveforms on seismic recordings that can be stacked to improve the signal-to-noise ratio. It is then possible to determine their focal mechanism. Ide, Shelly, and Beroza (2007) have shown that in southwest Japan, LFEs represent shear slip on a low-angle thrust fault dipping to the northwest, which corresponds to the plate interface. LFEs are usually grouped into families of events, with all the earthquakes of a given family originating from the same small patch on the plate interface.

They occur more or less episodically in a bursty manner, with days of high LFE activity followed by quiet periods. Shelly, Beroza, and Ide (2007b) have shown that tremor could be explained as a swarm of low-frequency earthquakes.

An important feature of slow earthquakes is that they generate a seismic signal with low amplitude compared to the noise recorded by earthquake monitoring networks. Therefore, careful use of signal processing methods is required to detect and locate them. Cross-correlation of seismic waveforms is a standard technique to determine delay times between two phase arrival times (Van Decar and Crosson, 1990). For example, if tremor is occurring in roughly the same place on time scales of a minute or more it would have a very complex source-time function generating both P- and S-waves. For a nearby station with a steep ray path from the source of the tremor, correlating the vertical channel (dominated by P-waves) with one of the horizontal channels (dominated by S-waves) could produce a peak at lag times corresponding to the time difference between the arrival of the direct P-wave and the direct S-wave (S minus P time). High quality observations of S minus P travel times can be especially valuable for constraining tremor depths.

Another possibility is small earthquakes that repeats many times in the same place with the same focal mechanism, as is the case for low-frequency earthquakes. Similar waveforms will be thus seen on the signal recorded by a seismic sensor at different time intervals. The cross-correlation will give the delay time between the wave arrivals, that is the delay times between the LFEs. This method allowed Shelly et al. (2006) to build a catalog of P- and S-wave arrival times and to locate the source of the LFEs. Moreover, by stacking the waveforms corresponding to several LFEs with the same source and the same focal mechanism, we can build a template waveform. It is then possible to detect a subsequent LFE with low amplitude by cross-correlating the seismic signal with this template waveform. The time of the maximum cross-correlation corresponds to the occurrence time of the LFE (Shelly, Beroza, and Ide, 2007b). Finally, by stacking the cross-correlation over several seismic stations, a better detection rate can be achieved (Gibbons and Ringdal, 2006).

Wavelet methods such as the Discrete Wavelet Transform (DWT) and the Maximal Overlap Discrete Wavelet Transform (MODWT) are mathematical tools for analyzing time series simultaneously in the time and the frequency domain by observing how weighted differences of a time series vary from one period to the next. The wavelet transform is thus similar to a narrow-band filter. The main difference with a Fourier analysis is that, when applying the short-time Fourier transform to a signal with low-frequency content, the frequency resolution decreases with the duration of the time windows considered. The great strength of the wavelets over the short-time Fourier transform is that it can analyze simultaneously high-frequency components with high temporal resolution and low-frequency components with low temporal resolution.

In this dissertation, I have used cross-correlation-based signal processing methods to analyze seismic recordings in the second and the third chapter and wavelet-based signal processing methods to analyze GNSS recordings in the fourth chapter.

As tectonic tremor have been explained as a swarm of LFEs, which are located on a narrow fault at the plate boundary, it is assumed that the source of the tectonic tremor is also located close to the plate boundary. However, due to the lack

of impulsive phases in the tremor signal, it is difficult to determine the depth of the tremor source and the distance of the source to the plate interface with great precision. Using a source scanning algorithm, Kao et al. (2005) found that tremor under southern Vancouver Island were distributed across a wide depth range of over forty kilometers, with a peak at the depth of twenty-five to thirty-five kilometers. That would locate the tremor mostly above the plate boundary, in the lower continental crust west to the fore-arc mantle corner. Kao et al. (2009) then further reduced the thickness of the tremor zone to five to ten kilometers and Ide (2012) estimated the uncertainties on the location of the tremor at about 1.5 kilometer in epicenter and 4.5 kilometer in depth. Comparing the depth of the tremor with the depth of the LFEs would provide further evidence for or against the hypothesis that tremor is the sum of many LFEs. Locating the source of the tremor compared to the regions with high-pore fluid pressure would help understand the mechanism that produces the tremor.

In the second chapter of this dissertation, I have used data from eight small-aperture arrays installed in the eastern part of the Olympic Peninsula, Washington. By computing the cross-correlation of an horizontal component of the seismograms with the vertical component, and stacking over time and seismic stations, I have been able to determine the time lag between the arrival of the direct P-wave and the arrival of the direct S-wave for different locations of the tremor and the arrays. From this, I have been able to determine the depth of the tremor source, the depth extent, and the associated uncertainty. We find that the tremor is within a few kilometers of the late boundary inferred by Preston et al. (2003) with a typical thickness less than three kilometers.

The relatively short recurrence of LFE swarms results in a rich history both in space and time and reveals potential patterns. These event histories could allow scientists to see many complete event cycles, which is typically not possible to explore in traditional earthquake catalogs. However, most of the work on LFEs has been focused on detecting LFEs during periods of high tremor activity, grouping them into families of events, and locating the source of the LFE families. Longer catalogs (several years) have been established for LFE families in Mexico, the San Andreas Fault, Washington State, Vancouver Island, New Zealand and Japan, but only a short catalog (one-month-long) existed for southern Cascadia.

In the third chapter of this dissertation, I have used the templates obtained by Plourde et al. (2015) using data recorded by the FAME network in southern Cascadia during an episode of high tremor activity in April 2008, and I extended their catalog to the whole two years (2007-2009) during which the seismic stations were installed. I then used the two-year-long catalog to create templates for stations from the permanent seismic networks, and used the seismic data recorded by these stations to extend the catalog before and after the FAME experiment, from 2004 to 2011. We detect LFEs every time that there is tectonic tremor on the tremor catalog from Boyarcho et al. (2015). The same pattern observed in northern Cascadia for down-dip / up-dip LFE activity and tidal modulation can also be observed in southern Cascadia.

In subduction zones such as Nankai and Cascadia, tectonic tremor observations are spatially and temporally correlated with slow-slip observations. Due to this correlation, several studies have used tremor as a proxy to observe small slow-slip events that are not directly detectable in the GNSS data. However, these methods cannot be applied to detect slow-slip events in places where tremor and slow-slip

occurrence are not well spatially and temporally correlated, tremor is not abundant, or the seismic network is not robust enough. We thus need other methods to be able to better detect and quantify slow-slip. Better signal processing methods would enable us to extract much more information from the GNSS data currently available. In particular, observing slow-slip events with a large range of magnitudes would help us verify whether a cubic moment-duration scaling law similar to the one established for regular earthquakes is also valid for slow-slip events (Ide et al., 2007). Moreover, to evaluate how much strain from the plate motion is accommodated by the slow-slip, we cannot only focus on the large short-term slow-slip events, we also need to take into account all possible small events.

In the fourth chapter of this dissertation, I have used wavelet methods to analyze GNSS time series and tremor recordings of slow-slip events in Cascadia. In both time series, I could then see simultaneous waveforms whose timing corresponds to the timing of slow-slip events. I assumed that there is a slow-slip event whenever the wavelet signal gets above a threshold. I verified that there is a good correlation between slow-slip events detected with only GNSS data, and slow-slip events detected with only tremor data. The wavelet-based detection method detects well events of magnitude higher than 6 as determined by independent event catalogs (Michel, Gualandi, and Avouac, 2019).

Chapter 2

Depth and thickness of tectonic tremor in the northeastern Olympic Peninsula

Tectonic tremor has been explained as a swarm of low-frequency earthquakes, which are located on a narrow fault at the plate boundary. It is therefore assumed that the source of the tectonic tremor is located close to the plate boundary. However, due to the lack of clear impulsive phases in the tremor signal, it is difficult to determine the depth of the tremor source and the distance of the tremor source to the plate interface with great precision. The thickness of the tremor region is not well constrained either. The tremor may be located on a narrow fault as the low-frequency earthquakes appear to be, or distributed over a few kilometers wide low shear-wave velocity layer in the upper oceanic crust, which is thought to be a region with high pore-fluid pressure. Comparing the depth of the tremor with the depth of the low-frequency earthquakes will provide further evidence for or against the hypothesis that tremor is the sum of many low-frequency earthquakes. Locating the source of the tremor compared to the regions with high-pore fluid pressure will help understand the mechanism that produces the tremor. In this chapter, lag times of peaks in the cross-correlation of the horizontal and vertical components of tremor seismograms, recorded by small-aperture arrays in the Olympic Peninsula, Washington, are interpreted to be S-minus-P times. Tremor depths are estimated from these S-minus-P times using epicenters from a previous study using a multibeam backprojection method. The tremor is located close to the plate boundary in a region no more than 2-3 kilometers thick and is very close to the depths of low-frequency earthquakes. The tremor is distributed over a wider depth range than the low-frequency earthquakes. However, due to the uncertainty on the depth, it is difficult to conclude whether the source of the tremor is located at the top of the subducting oceanic crust, in the lower continental crust just above the plate boundary, or in a narrow zone at the plate boundary.

This chapter has been published in Journal of Geophysical Research: Solid Earth:

Ducellier, A., & Creager, K. C. (2022). Depth and thickness of tectonic tremor in the northeastern Olympic Peninsula. *Journal of Geophysical Research: Solid Earth*, 127, e2021JB022708. <https://doi.org/10.1029/2021JB022708>.

I would like to thank Abhijit Ghosh for sharing his tremor catalog. I also would like to thank Charles Sammis and an anonymous reviewer whose reviews have helped improve this chapter. This project was funded by NSF grant EAR-1358512. I would like to thank the Integral Environmental Big Data Research Fund from the

College of the Environment of University of Washington, which funded cloud computing resources to carry out the data analyses. The seismic recordings used for this analysis can be downloaded from the IRIS website using network code XG, 2009-2011. Most of the figures were done using GMT (Wessel and Smith, 1991). The Python scripts used to analyze the data and make the figures can be found on my Github account, accessible through Zenodo (Ducellier, 2021).

2.1 Introduction

Tremor is a long (several seconds to many minutes), low amplitude seismic signal, with emergent onsets, and an absence of clear impulsive phases. Tectonic tremor has been explained as a swarm of small, low-frequency earthquakes (LFEs) (Shelly, Beroza, and Ide, 2007b), that is small magnitude earthquakes ($M \sim 1$) where frequency content (1-10 Hz) is lower than for ordinary small earthquakes (up to 20 Hz). The source of the LFEs is located on or near the plate boundary, and their focal mechanisms represent shear slip on a low-angle thrust fault dipping in the same direction as the plate interface (Ide, Shelly, and Beroza, 2007; Royer and Bostock, 2014). The polarization of tremor in northern Cascadia is also consistent with slip on the plate boundary in the direction of relative plate motion (Wech and Creager, 2007). Due to the lack of clear impulsive phases in the tremor signal, it is difficult to determine the depth of the tremor source with the same precision. In subduction zones such as Nankai and Cascadia, tectonic tremor observations are spatially and temporally correlated with geodetically observed slow-slip (Obbara, 2002; Rogers and Dragert, 2003). Due to this correlation, these paired phenomena have been called Episodic Tremor and Slip (ETS).

The occurrence of tremor seems to be linked to low effective normal stress or high fluid pressure near the location of the tremor. Indeed, Shelly et al. (2006) have observed a high P-wave to S-wave velocity ratio in the subducting oceanic crust near the location of the LFEs in western Shikoku, Japan. In Cascadia, Audet et al. (2009) have computed teleseismic receiver functions in Vancouver Island, and analyzed the delay times between the forward-scattered P-to-S, and back-scattered P-to-S and S-to-S conversions at two seismic reflectors identified as the top and bottom of the oceanic crust. It allowed them to compute the P-to-S velocity ratio of the oceanic crust layer and the S-wave velocity contrast at both interfaces. The very low Poisson's ratio of the layer could not be explained by the mineral composition, and they interpreted it as evidence for high pore-fluid pressure. The link between tremor and high pore fluid pressure is also supported by the influence of tidal cycles on the variations of tremor occurrence. Nakata, Suda, and Tsuruoka (2008) noticed that tremor swarms often exhibit occurrences with a periodicity of about 12 or 24 h, and concluded that they are probably related to Earth tides. Their occurrence is also well correlated with time evolution of Coulomb failure stress (CFS) and CFS rate. However, tremor occurrences are advanced by a few hours relative to CFS, from which they conclude that a simple Coulomb threshold model is not sufficient to explain tremor occurrence. This discrepancy can be explained by using a rate-and state-dependent friction law. Thomas, Nadeau, and Bürgmann (2009) have also observed that tremor occurrence on the deep San Andreas fault are correlated with small, tidal shear stress changes. They explain it by a very weak fault zone with low effective normal stress, probably due to near-lithostatic pore pressures at the depth

of the tremor source region.

Two scenarii could explain the generation of tectonic tremor by highly pressured fluids (Shelly et al., 2006). A first possibility is that tremor is generated by the movement of fluids at depth, either by hydraulic fracturing or by coupling between the rock and fluid flow. The accompanying slip could be triggered by the same fluid movement that generates the tremor or, alternatively, the fluid flow could be a response to changes in stress and strain induced by the accompanying slip. The second possibility is that tremor is generated by slow otherwise aseismic shear slip on the plate interface as slip locally accelerates owing to the effects of geometric or physical irregularities on the plate interface. Fluids would then play an auxiliary role, altering the conditions on the plate interface to enable transient slip events, without generating seismic waves directly.

The source of the fluids could be the dehydration of hydrous minerals within the subducting oceanic crust (Shelly et al., 2006). Fagereng and Diener (2011) computed the equilibrium mineral assemblages at different P-T conditions, and compared it to the P-T path of the subducting oceanic crust in Shikoku and Cascadia. They noted that for most of the P-T path, there are no dehydration reactions and the slab remains fluid-absent, except for depths between 30 and 35 km for Shikoku, and depths between 30 and 40 km for Cascadia, where the mineral model predicts significant water release. These depth ranges coincide with the depth range where tremor has been observed. They concluded that abundant tremor activity requires metamorphic conditions where localized dehydration occurs during subduction, which explains why the generation of tectonic tremor is restricted to a small range of depth along the plate boundary. In subduction zones where dehydration reactions are more widely distributed, there would be a more diffuse pattern of tremor activity that would be harder to detect.

Large amounts of fluids could be available at the fore-arc mantle corner. First, the bending of the subducting plate at the ocean trench may introduce water in the upper oceanic mantle, resulting in extensive serpentinization (Hyndman et al., 2015). Second, the serpentinization of the fore-arc mantle corner may decrease the vertical permeability of the boundary between the oceanic plate and the overriding continental crust while keeping a high permeability parallel to the fault. It would thus channel all the fluid updip in the subducting oceanic crust, and explain the sharp velocity contrast observed by Audet et al. (2009) on top of the oceanic crust layer. At greater depth, the large volume reduction and water release accompanying eclogitization in the subducted oceanic crust, and the large volume expansion accompanying serpentinization in the mantle wedge, could increase the permeability of the plate boundary through fracture generation. A possible cause of ETS events could thus be periodic cycles of steady pore-fluid pressure build-up from dehydration of subducted oceanic crust, fluid release from fracturing of the interface during ETS, and subsequent precipitation sealing of the plate boundary (Audet et al., 2009).

Whereas the position of the subduction zone ETS does not seem to coincide with a specific temperature or dehydration reaction (Peacock, 2009), there seems to be a good coincidence between the location of the fore-arc mantle corner, and the location of ETS (Hyndman et al., 2015). The generation of slow-slip and tectonic tremor could then be related to the presence of quartz in the overriding continental crust. Using receiver functions of teleseismic body waves, and data from the literature,

Audet and Bürgmann (2014) observed that the recurrence time of slow earthquakes increases linearly with the V_p / V_s ratio of the forearc crust. They also noticed that along a margin-perpendicular profile from northern Cascadia, the V_p / V_s ratio of the forearc, and the recurrence time of ETS events, decrease with increasing depth. Likewise, Hyndman et al. (2015) pointed out that the deep fore-arc crust has a very low Poisson's ratio (less than 0.22), and that the only mineral with a very low Poisson's ratio is quartz (about 0.1), which led them to conclude that there may be a significant amount of quartz (about 10% by volume) in the deep fore-arc crust above the fore-arc mantle. Audet and Bürgmann (2014) explained the presence of quartz in the forearc by the enrichment of forearc minerals in fluid-dissolved silica derived from the dehydration of the down-going slab. As the solubility of silica increases with temperature, fluids generated at depth and rising up the subduction channel should be rich in silica (Hyndman et al., 2015).

Quartz veins have indeed been observed in exhumed subduction zones. For instance, Fagereng, Hillary, and Diener (2014) have studied an exhumed shear zone representing the subduction megathrust before its incorporation into the accretionary prism. They focused their study on a 30 m high by 80 m long cliff exposure where foliation has developed as a result of shearing along the subduction thrust interface. They identified two groups of quartz veins, foliation-parallel veins, and discordant veins, that must have formed for an extended time before, during, and after foliation development. They interpret the foliation-parallel veins as having been formed by viscous shear flow, and note that the shear strain rate due to the flow may be high enough to accommodate a slow-slip strain rate of 10^{-9} s^{-1} , for a typical subduction thrust thickness of 30 m (Rowe, Moore, and Remitti, 2013). They interpret the discordant veins as having been formed by brittle deformation caused by locally elevated fluid pressure. The size of the structures where brittle deformation is observed (meters to hundreds of meters) is compatible with the size of the asperity rupturing during an LFE. Tremor and slow-slip may thus be a manifestation of brittle-viscous deformation in the shear zone.

However, several constraints remain to be explained. Audet and Bürgmann (2014) estimated that the fluid flux required for the formation of quartz veins was two orders of magnitude greater than the fluid production rates estimated from the dehydration of the slab. They hypothesized that silica-saturated fluids may originate from the complete serpentinization of the mantle near the wedge corner. They suggested that higher temperature and quartz content at depth may lead to faster dissolution - precipitation processes and more frequent slip events. Their model could also explain the global variation in recurrence time, with mafic silica-poor regions having longer ETS recurrence times than felsic silica-rich regions.

Moreover, the zone with high low Poisson's ratio observed by Hyndman et al. (2015) has a large vertical extent (about 10 kilometers). If the whole zone is associated with quartz deposition and tectonic tremor generation, we should also observe a large vertical distribution of the source of the tremor. Kao et al. (2006) have used a Source Scanning Algorithm to detect and locate tremor, and have indeed located tremor in the continental crust, with a wide depth range of over 40 km. They noted that this wide depth range could not arise from either analysis uncertainties or a systematic bias in the velocity model they used. Uncertainties on the location of the tremor have been estimated by Ide (2012) at about 1.5 km in epicenter and 4.5 km in depth. A follow-up study by Kao et al. (2009) gave a thickness of the tremor

zone of 5-10 km. This depth range is inconsistent with the depth of the LFEs, which have been located on a thin band at or near the plate interface with a rupture mechanism that corresponds to the thrust dip angle (Ide, Shelly, and Beroza, 2007). In the Olympic Peninsula, LFE families have been identified and located by Chestler and Creager (2017a) and Chestler and Creager (2017b), and all LFE families were located near the plate interface. Further study is thus needed to narrow the uncertainty on the depth of the source of the tremor, and verify whether tremor occurs in a wider zone than LFEs.

Several methods have been developed to detect and locate tectonic tremor or LFEs using the cross-correlation of seismic signals. The main idea is to find similar waveforms in two different seismic signals, which could correspond to a single tremor or LFE recorded at two different stations, or two different tremors or LFEs with the same source location but occurring at two different times and recorded by the same station. A first method consists in comparing the envelopes of seismograms at different stations (Obara, 2002; Wech and Creager, 2008), or directly the seismograms at different stations (Rubin and Armbruster, 2013). For instance, Wech and Creager (2008) computed the cross-correlations of envelope seismograms for a set of 20 stations in western Washington and southern Vancouver Island. Then, they performed a grid search over all possible source locations to determine which one minimizes the difference between the maximum cross-correlation and the value of the correlogram at the lag time corresponding to the S-wave travel time difference between two stations.

A second method is based on the assumption that repeating tremor or LFEs with sources located nearby in space will have similar waveforms (Bostock et al., 2012; Royer and Bostock, 2014; Shelly et al., 2006; Shelly, Beroza, and Ide, 2007b). For instance, Bostock et al. (2012) looked for LFEs by computing autocorrelations of 6-second long windows for each component of 7 stations in Vancouver Island. They then classified their LFE detections into 140 families. By stacking all waveforms of a given family, they obtained an LFE template for each family. They extended their templates by adding more stations and computing cross-correlations between station data and template waveforms. They used P- and S-travel-time picks to obtain a hypocenter for each LFE template. By observing the polarizations of the P- and S-waveforms of the LFE templates, they computed focal mechanisms and obtained a mixture of strike slip and thrust mechanisms, corresponding to a compressive stress field consistent with thrust faulting parallel to the plate interface. Further study showed that the average double couple solution is generally consistent with shallow thrusting in the direction of plate motion (Royer and Bostock, 2014).

Finally, a third method uses seismograms recorded across small-aperture arrays (Ghosh et al., 2010a; La Rocca et al., 2009). For instance, La Rocca et al. (2009) stacked seismograms over all stations of the array for each component, and for three arrays in Cascadia. They then computed the cross-correlation between the horizontal and the vertical component, and found a distinct and persistent peak at a positive lag time, corresponding to the time between P-wave arrival on the vertical channel and S-wave arrival on the horizontal channels. Using a standard layered Earth model, and horizontal slowness estimated from array analysis, they computed the depths of the tremor sources. They located the sources near or at the plate interface, with a much better depth resolution than previous methods based on seismic signal envelopes, source scanning algorithm, or small-aperture arrays. They concluded that

at least some of the tremor consisted in the repetition of LFEs as was the case in Shikoku. A drawback of the method was that it could be applied only to tremor located beneath an array, and coming from only one place for an extended period of time.

In this study, we extend on the method used by La Rocca et al. (2009) using the cross-correlation between horizontal and vertical components of seismic recordings to estimate the depth of the source of the tectonic tremor, and the depth extent of the region from which tremor originates. If indeed tremor is made of swarms of LFEs, and both represent the regions of deformation during ETS events, we would expect the thickness of the tremor to be the same as the thickness of the LFEs. If not, tremor may be occurring where LFEs are harder to detect because they are either smaller in amplitude, or spread out over continuous space and not as clearly repeating.

2.2 Data

The data were collected during the 2009-2011 Array of Arrays experiment. Eight small-aperture arrays were installed in the northeastern part of the Olympic Peninsula, Washington. The aperture of the arrays was about 1 km, and station spacing was a few hundred meters. Arrays typically had ten 3-component seismometers, augmented by an additional 10 vertical-only sensors during the 2010 ETS event. The arrays were around 5 to 10 km apart from each other (Figure 2.1). Most of the arrays recorded data for most of a year, between June 2009 to September 2010, and captured the main August 2010 ETS event. The arrays also recorded the August 2011 ETS event with a slightly reduced number of stations. Ghosh, Vidale, and Creager (2012) used a multibeam backprojection (MBBP) technique to detect and locate tremor. They bandpass filtered the vertical component between 5 and 9 Hz and divided the data into one-minute-long time windows. They performed beam forming of vertical component data in the frequency domain at each array to determine the slowness vectors, and backprojected the slownesses through a 3-D wavespeed model (Preston et al., 2003) to locate the source of the tremor for each time window. This produced 28902 tremor epicenters for one-minute-long time windows during June, 2009 - September, 2010 and 5600 epicenters during August - September, 2011.

2.3 Method

For each array, and every 5 km by 5 km grid cell located within 25 km, we analyze the one-minute-long time windows corresponding to all the tremor epicenters located within the grid cell. For each three-component seismic station and each channel, we detrended the data, tapered the first and last 5 seconds with a Hann window, removed the instrument response, bandpass filtered between 2 and 8 Hz, and resampled the data to 20 Hz. All these preprocessing operations were done with the Python package obspy. For each seismic station and each one-minute-long time window, we cross correlated the vertical component with the East-West component and with the North-South component. Then, we stacked the cross correlation functions over all the seismic stations of the array. We call this stack $S_{ij}(\tau)$ for time lag τ , the i -th channel ($i=1$ or 2 for the North or East channel) and the j -th one-minute-long time window for a given epicenter grid/array pair. At each step of this method we experimented with a linear stack, a n th-root stack, and a phase-weighted stack (Schimmel and Paulssen, 1997) and found that the phase-weighted stack worked

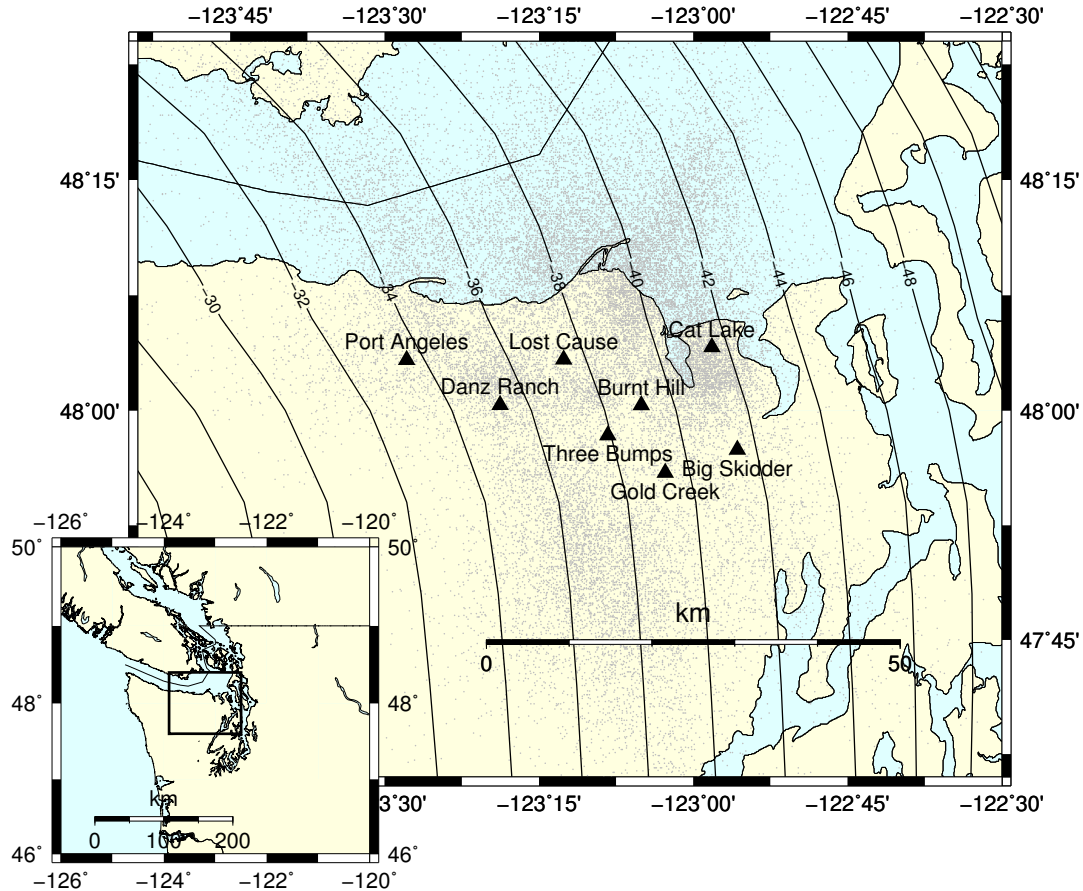


FIGURE 2.1: Map showing the location of the eight arrays (black triangles) used in this study and tremor locations (grey dots) located using these arrays (Ghosh, Vidale, and Creager, 2012). Inset shows the study area with the box marking the area covered in the main map. Contours represent a model of the depth of the plate interface (McCrory et al., 2006).

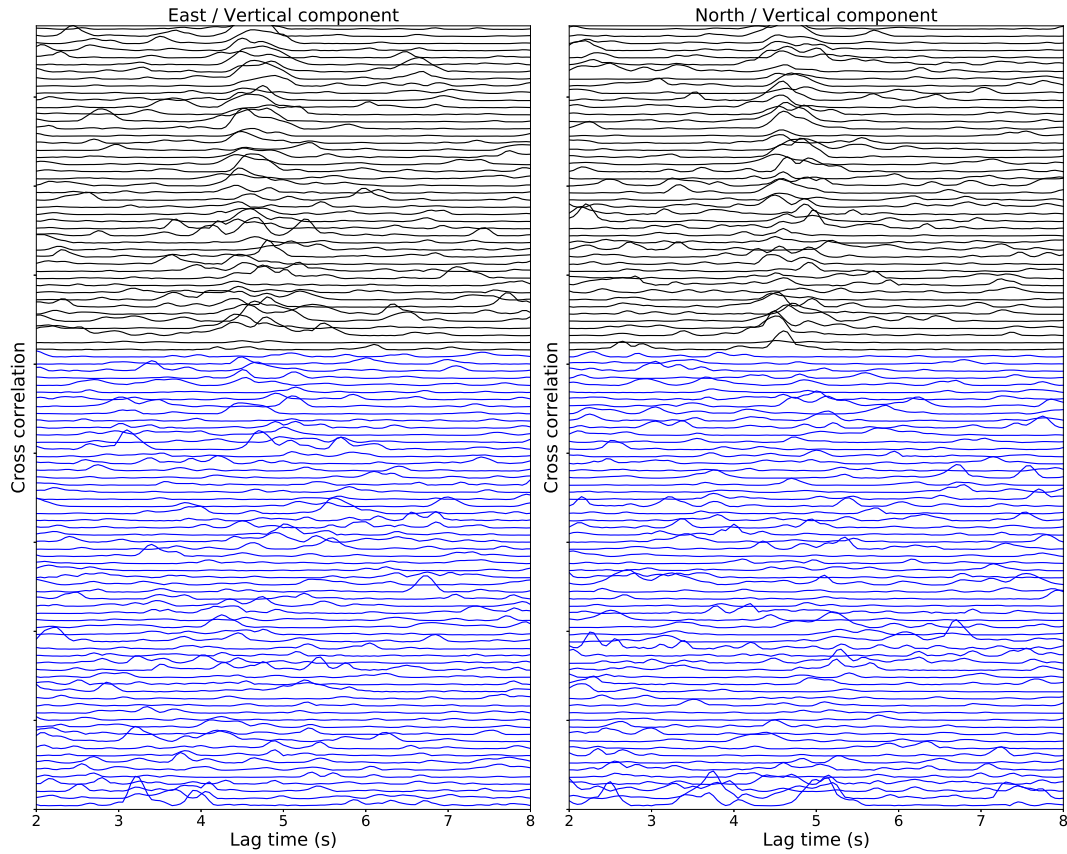


FIGURE 2.2: Envelopes of the stacked cross-correlation functions for the Big Skidder array for the 110 one-minute long time windows when tremor was detected in a 5 km by 5 km grid cell located 7 kilometers southwest of the array. Top shows time windows (black) that fit the stack well. Bottom shows time windows (blue) that do not fit the stack well. Left panel is the cross-correlation of the EW component with the vertical component, and right panel is the cross-correlation of the NS component with the vertical component. The cross-correlation functions have been cut between 2 and 8 seconds to focus on the time lags around the peaks.

best. So, all the stacks discussed here used the phase-weighted method. Figure 2.2 shows an example of the envelopes of $S_{ij}(\tau)$ for the Big Skidder array for the 110 one-minute-long time windows when tremor was detected in the 5 km by 5 km grid cell located 7 kilometers southwest of the array. For all time windows, there is a peak in the envelopes of the cross-correlation $S_{ij}(\tau)$ at $\tau = 0\text{s}$ (not shown in the figure). Additionally, for about 40% of the time windows, we also see another peak in the envelopes of the cross-correlation $S_{ij}(\tau)$ at about $\tau = 4.5\text{s}$. As the energy of the P-waves is expected to be higher on the vertical component, and the energy of the S-waves to be higher on the horizontal components, we interpret this peak to correspond to the time lag between the arrival of the direct P- and S-waves. This peak is only seen for the positive time lag, and no peak is seen in the negative part of the cross-correlation.

Only about half of the envelopes of the cross-correlation functions have a distinct

peak that coincides with the peak in the stacked cross-correlation. The other cross-correlation functions show either a distinct peak at another time lag, or no clearly visible peak. This may be either because the tremor epicenter was mislocated, or because the signal-to-noise ratio is too low.

To determine which time window to use for further consideration we compute the theoretical value of the time lag between the P- and S-wave arrivals if the source was located on the plate boundary. We then look for the lag time corresponding to the peak of the absolute value of the stack within 1 second of the theoretical lag time. We do this nine times for each combination of 3 stacking methods acting on the stack of stations for each array and on the stacks across each of the one-minute time windows. The stacking methods are a linear stack, a n th-root stack or a phase-weighted stack. We define T_{min} to be the minimum of these 9 lag times minus 1 s and T_{max} to be the maximum of these 9 times plus 1 s. We limit the rest of our analysis to the time window $[T_{min}; T_{max}]$. We define τ_{max} to be the time corresponding to the peak absolute value of the phase-weighted stack within these time limits. τ_{max} turns out to also be the time corresponding to the maximum of the stacked correlations within a fixed wide window from 3-8 s for all the array / grid pairs except for one (BH, grid that is 7 km to the southeast). This suggests that there is very little, if any, bias in our method forcing our final observed S minus P times towards their theoretical values.

To improve the signal-to-noise ratio of the peak in the stacked cross-correlation, we divided the one-minute-long time windows into two clusters, the ones that match the stacked cross-correlations well, and the ones that do not. In order to do the clustering, we stacked the stacked cross-correlation functions, $S_{ij}(\tau)$, over all the one-minute-long time windows to obtain $S_i(\tau)$. For each one-minute time window j we cross-correlated $S_i(\tau)$ with $S_{ij}(\tau)$ to obtain $S_{ij}^c(\tau)$. We want to verify whether the waveform $S_{ij}(\tau)$ around the peak τ_{max} matches well with the stack $S_i(\tau)$. For the cross-correlation between $S_{ij}(\tau)$ and $S_i(\tau)$, we keep only the values of lag times τ between T_{min} and T_{max} . For each i and j we determine 3 numbers from $S_{ij}^c(\tau)$: its value at zero lag time, its maximum absolute value and the time lag at which it takes its maximum absolute value, and we determine one number from $S_{ij}(\tau)$: the ratio of its maximum absolute value $S_{ij}(\tau)_{max}$ to its rms. We considered lag times τ from 12 to 14 seconds to compute the value of the rms of the $S_{ij}(\tau)$. Each one-minute-long time window is thus associated with eight values of quality criteria, four for each of the East and North channels. We then classified each one-minute-long time window into two different clusters, based on the value of these criteria, using a K-means clustering algorithm (function `sklearn.cluster.KMeans` from the Python library SciKitLearn (Pedregosa et al., 2011)). The K-means procedure is as follows: we choose to have 2 clusters, then we arbitrarily choose a center for each cluster. We put each one-minute-long time window into the cluster to which it is closest (based on the values of the eight criteria). Once all one-minute-long time windows have been put in a cluster, we recompute the mean of the eight criteria for each cluster, and iterate the procedure until convergence. On average, about 35% of the time windows fit well with the stack and are kept in the first cluster, while 65% do not fit well with the stack and are removed. For each cluster, we then stacked the envelopes of the cross-correlation functions over all the one-minute-long time windows belonging to that cluster using a phase-weighted stack. We tried using more than 2 clusters, but it did not improve the final stack of the best cluster. Figure 2.3 shows the stack of the envelopes of the $S_{ij}(\tau)$ over the time windows j that correspond to cluster 0 (red)

and cluster 1 (blue). The clustering has greatly improved the amplitude of the peak for cluster 1, and made the peak nearly disappear for cluster 0.

We did this analysis for grid cells located in a 50 km by 50 km area centered on each of the eight arrays. We thus consider up to $11 * 11 * 8 = 968$ values of the time lag between the direct P-wave and S-wave. We assumed that the epicenter is at the center of the grid and determined the depth that satisfies that epicenter and the observed S-minus-P time. The velocity models are taken from the 3D velocity model from Merrill et al. (2020). For each array, we looked for the closest grid point (in terms of latitude and longitude) in the 3D model by Merrill et al. (2020) and used the corresponding layered model of compressional and shear wave speeds to compute the tremor depth. We thus used 8 different 1D velocity models corresponding to the 8 arrays. This allows us to take into account the substantial variations of the Poisson's ratio in the East-West direction.

2.4 Results

To obtain robust results, we limit our analysis to grid cells where there are at least 30 one-minute-long time windows in the best cluster. We assumed that the location of the tremor source is fixed during the one-minute-long time window where we compute the cross-correlation of the seismic signal. However, during an ETS event, rapid tremor streaks have been observed to propagate up-dip or down-dip at velocities ranging on average between 30 and 110 km/h (Ghosh et al., 2010b), which corresponds to a maximum source displacement of 0.9 km updip or downdip during the 30 seconds duration before and after the middle of the time window. The change in predicted S-minus-P time caused by changing source location by 0.9 km in the up- or down-dip direction is small for tremor along strike from the array or in the down dip direction. However, the change in this lag time for tremor sources up-dip from the arrays exceeds one quarter of the dominant period of the tremor signal (period= 0.33 s) for tremor sources more than 18 km updip from an array. Thus, tremors beyond 18 km updip of an array may not add coherently during rapid tremor migrations. This method works best if the P-wave is cleanly recorded on the vertical component and the S-wave on the horizontals, so generally speaking the results are more robust for near vertical ray paths.

Finally, the data from some of the arrays are very noisy, which makes it hard to see a signal emerging when stacking over the one-minute-long time windows. We chose to keep only the locations for which the ratio between the maximum value of the stack of the envelopes of the cross-correlation functions to the root mean square is higher than 5. We compute the root mean square in cluster 1 for a time lag between 12 and 14 s because we do not expect any reflected wave to arrive that late after a direct wave. The corresponding stack of the envelopes of the cross-correlation functions are shown in Figure 2.4 for the East-West component and the North-South component. The grey dashed vertical line shows the theoretical time lag between the arrival of the direct P-wave and the arrival of the direct S-wave using the corresponding 1D velocity model for this array and the plate boundary model from Preston et al. (2003), the grey solid line corresponds to the moment centroid of the

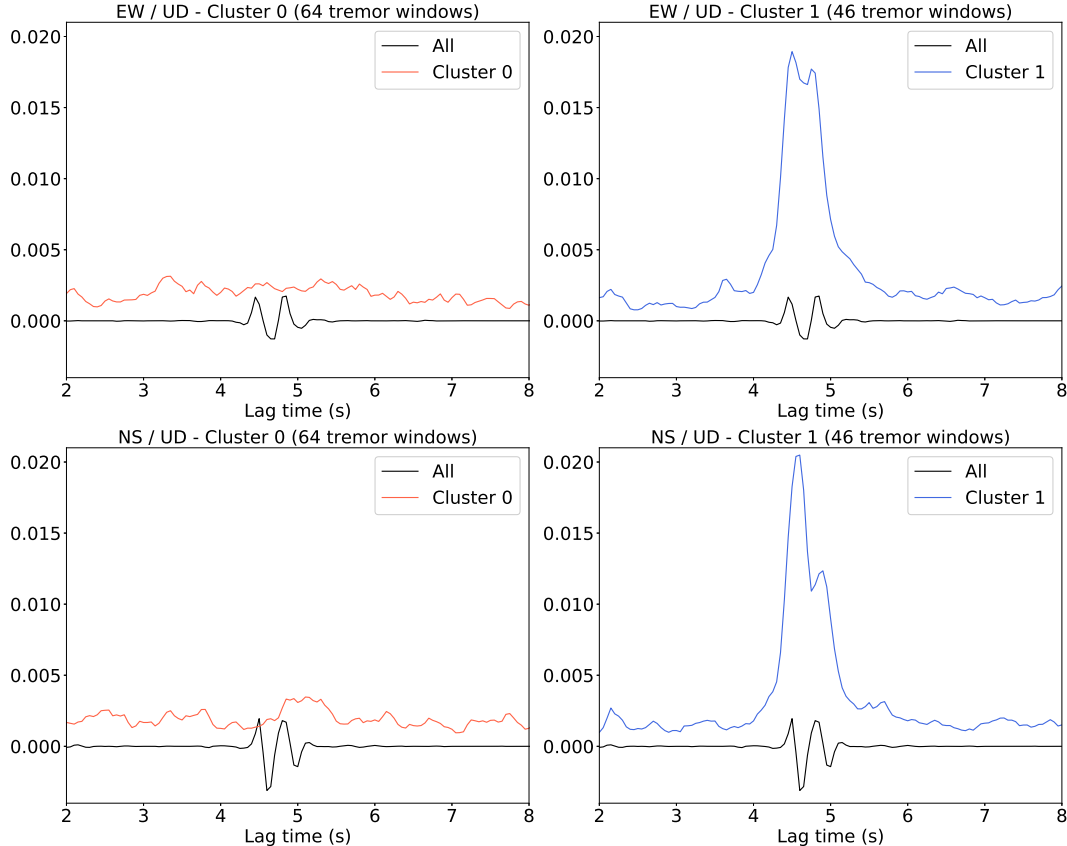


FIGURE 2.3: Stack of the cross-correlation functions over all the 110 time windows from Figure 2.2. The black line is the stack $S_i(\tau)$ over all time windows of the stack of cross-correlation functions over all stations within the array. The red line on the left panels is the stack over all the time windows in cluster 0 of the envelopes of the stack of cross-correlation functions over stations within the array. This corresponds to time windows that do not fit well with the stack. The blue lines on the right panels are the same as the red lines, except it uses time windows in cluster 1 (which contains the time windows that fit well with the stack). Top panels are the cross-correlation of the EW component with the vertical component, and bottom panels are the cross-correlation of the NS component with the vertical component. The stacked cross-correlation function has been cut between 2 and 8 seconds to focus on the time lags around the peak.

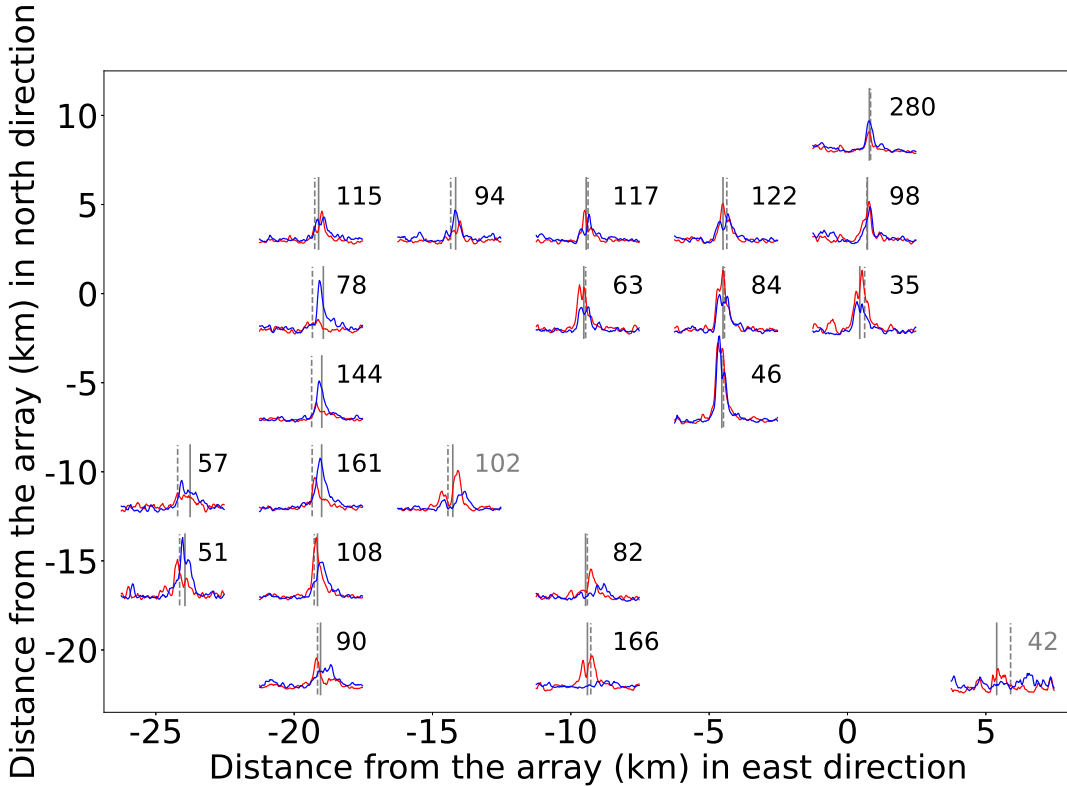


FIGURE 2.4: Stack of the envelopes of the cross-correlation signals for different positions of the tremor source relative to the Big Skidder array showing the cross-correlation between the East-West and the vertical components (red lines) and between the North-South and vertical components (blue lines). The theoretical S-minus-P times (grey dashed line for the Preston model) are generally in good agreement with the centroids in cross-correlation functions (grey solid line). The location of the tremor varies from west to east (left to right) and from south to north (bottom to top). The numbers next to each graph indicate the number of one-minute-long time windows in the best cluster. For clarity, we plotted only the part of the cross-correlation signal corresponding to time lags between 2 and 8 seconds.

stack. There is a good agreement between the timing of the centroid and the theoretical time lag for most of the locations of the source of the tremor.

To compute the depth, we select the EW or the NS component with the larger maximum value of the peak. We focus on the part of the stack of the envelopes of the cross-correlation functions located between 2 seconds before and 2 seconds after the time lag τ_{max} corresponding to the peak obtained earlier. We computed the moment centroid of this part of the stack and assumed that it was equal to the time lag between the arrivals of the direct P-wave and the direct S-wave. We then computed the corresponding depth of the source of the tremor for all the locations of the source of the tremor. To verify the effect of the width of the time window for which we compute the moment centroid, we compute the centroid and the corresponding depth of the source for widths equal to 2 seconds, 4 seconds, and 6 seconds. We compute the variations in depths when decreasing the width from 4 seconds to 2 seconds. 87% of the differences in depth are under 2 kilometers. The median difference is 0.064 km,

so there is no bias towards shallower or deeper depths when we decrease the width of the time window. When we compute the variations in depths when increasing the width from 4 seconds to 6 seconds, 84% of the differences in depth are under 2 kilometers and the median difference is 0.054 km. The corresponding stacks of the envelopes are shown in Figure 2.4 and Figures A.1 to A.7 in Appendix A. For the two arrays Cat Lake and Lost Cause, there are very few source-array locations that have both enough tremor and a high ratio between the peak and the root mean square. Moreover, for the locations where we have a peak, the peak is often not very clear and stretched along the time axis. We did not use data from these two arrays. For the Port Angeles array, there is only a clear peak for a near vertical incidence of the seismic waves. We choose to keep this array in the analysis in order to have two additional data points in the westernmost region of the study area.

To estimate the uncertainty on the depth of the source of the tremor, we computed the width of the stack of the envelopes of the cross-correlation functions at half the maximum of the peak. We then computed the associated depth difference using the 1D velocity model. As we computed the envelopes of the cross-correlation functions before stacking, the peak is large and also the associated uncertainty on the depth. Nevertheless, about 75% of the data points have an uncertainty under 8km (Figure 2.5). The uncertainties are higher for the Burnt Hill array, and are almost always lower than 8km for the five other arrays. We tried different stacking methods, both for the stacking of the correlation functions over all the seismic stations of a given array, and for the stacking of the envelopes of those stacks over the one-minute-long time windows when tremor is detected. We experimented with a linear stack, a n th-root stack, and a phase-weighted stack, and found that using a phase-weighted stack for both the stacking over the stations and the stacking over one-minute-long time windows gave the lower uncertainty on the tremor depth.

In the following, we kept only the data points for which the maximum amplitude of the stack is higher than 0.05. Figures 2.6 and 2.7 show respectively a map and three cross-sections of the depth of the source of the tremor. Figure 2.8 shows a map of the distance between the source of the tremor and the plate boundary from the Preston model, alongside with the depth of the low-frequency earthquake families observed by Sweet et al. (2019) and Chestler and Creager (2017a) and Chestler and Creager (2017b). There is a good agreement between the depth of the source of the tremor, the depth of the low-frequency earthquake families, and the depth of the plate boundary. On the cross-section figures, we compare the distance of the source of the tremor to the plate boundary for different locations of the cross-section. We note that the depth of the tremor matches well the depth of the low-frequency earthquakes.

2.5 Discussion

Previous studies have shown evidence for seismic anisotropy near the slab interface (Nikulin, Levin, and Park, 2009) and in the overriding continental crust (Cassidy and Bostock, 1996). If the source of the tremor is located in or under the anisotropic layer, the time lag between the arrival of the direct P-wave and the arrival of the direct S-wave could be different depending on whether we consider the East-West component or the North-South component. To verify whether possible anisotropy

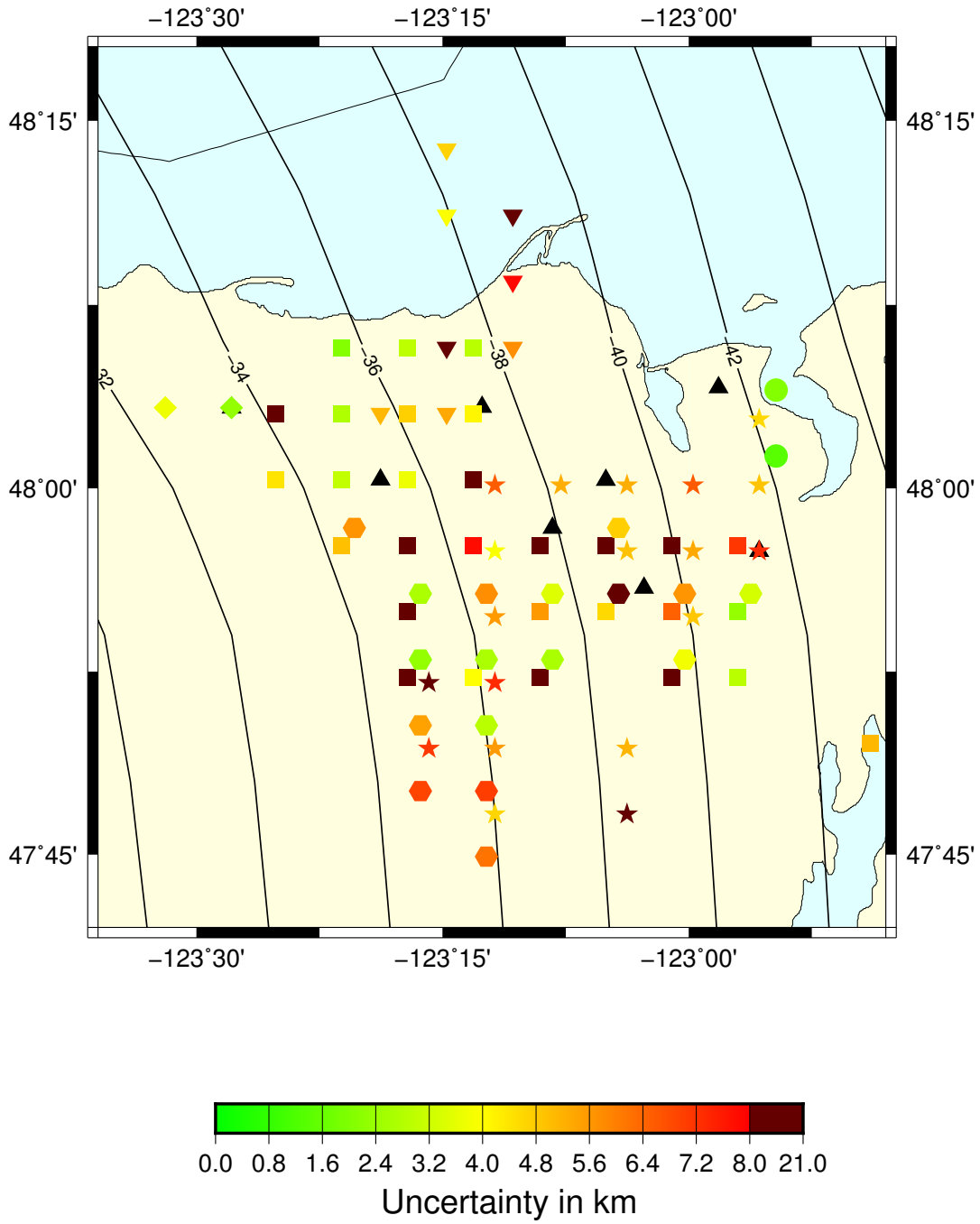


FIGURE 2.5: Map of the uncertainty on the depth of the tremor based on the width of the stack of the envelopes of the cross-correlation functions for arrays Burnt Hill (squares), Big Skidder (stars), Danz Ranch (inverted triangles), Gold Creek (large circles), Port Angeles (diamonds), and Three Bumps (hexagons).

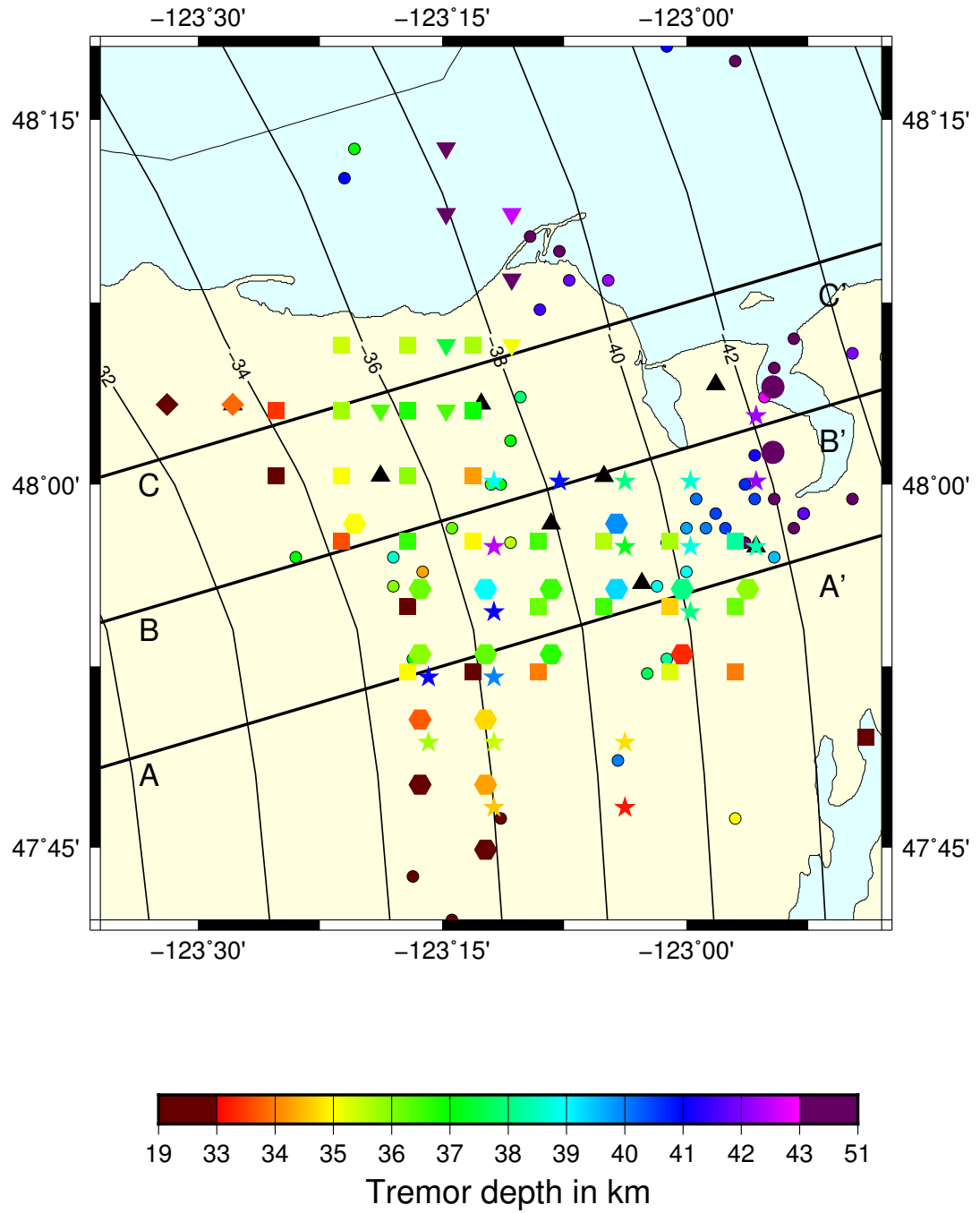


FIGURE 2.6: Map of the depth of the source of the tremor and of the low-frequency earthquake families (small filled circles) identified by Sweet et al. (2019) and Chestler and Creager (2017a) and Chestler and Creager (2017b). The three black lines indicate the positions of the cross-sections shown in Figure 2.7. Tremor depths are from arrays Burnt Hill (squares), Big Skidder (stars), Danz Ranch (inverted triangles), Gold Creek (large circles), Port Angeles (diamonds), and Three Bumps (hexagons).

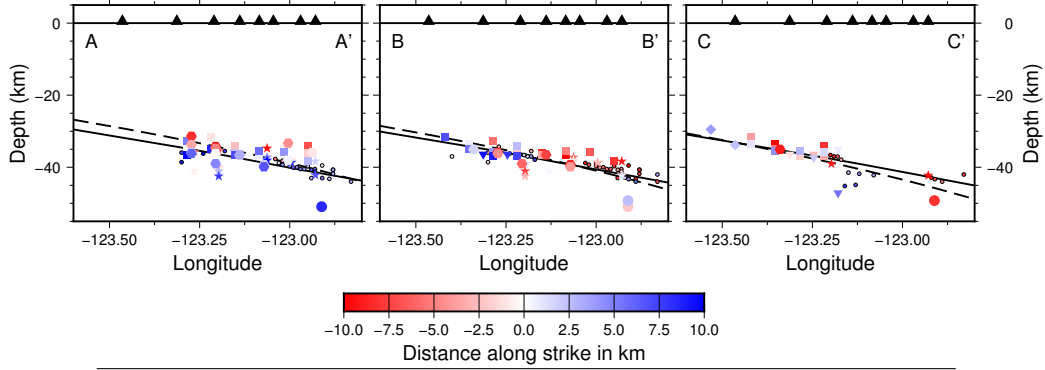


FIGURE 2.7: Cross-sections showing depth of the tremor and of the low-frequency earthquake families (small filled circles) identified by Sweet et al. (2019) and Chestler and Creager (2017a) and Chestler and Creager (2017b) for cross sections A-A', B-B', and C-C' shown in Figure 2.6. The black line corresponds to the plate boundary profile of McCrory et al. (2006) along the southern most black line shown on Figure 2.6, and the dashed line to the plate boundary profile of Preston et al. (2003). The color bar shows the distance of the tremor and the low-frequency earthquakes along the strike. Only tremor and low-frequency earthquakes less than 10 km away from the profile line are shown. Tremor depths are from arrays Burnt Hill (squares), Big Skidder (stars), Danz Ranch (inverted triangles), Gold Creek (large circles), Port Angeles (diamonds), and Three Bumps (hexagons).

could affect our results, we computed the time difference between the timing of the maximum of the stack of the envelopes of the stacked cross-correlation functions between the East-West component and the vertical component, and between the North-South component and the vertical component. We also computed the associated difference in depth of the source of the tremor (see Figure 2.9) for all arrays and all locations of the tremor. The difference in time is generally less than 0.25 s while the difference in depth is generally less than 2 kilometers, which is similar to the uncertainty on the tremor depth. As the time difference between the East-West component and the North-South component due to anisotropy is expected to vary depending on the relative position of the array compared to the source of the tremor, we also plotted the time difference as a function of the distance from source to array, and as a function of the azimuth, as well as the corresponding depth difference (Figure 2.9). The time difference does not increase with the distance from the source to the array, and there is no seismic path orientation that gives bigger time difference. Thus, seismic anisotropy does not seem to have a significant effect on the time lags between the arrival of the direct P-wave and the arrival of the direct S-wave, and can be neglected. Nikulin, Levin, and Park (2009) observed anisotropy in the low-velocity layer beneath station GNW, located in the eastern Olympic Peninsula, south of the eight seismic arrays used in this study. If the tremor is located above the low-velocity layer, we do not expect this source of seismic anisotropy to introduce a significant effect on our measured time lags. Nikulin, Levin, and Park (2009) locate the low-velocity layer above the plate boundary, in the lower continental crust, which is shallower than the location given by Bostock (2013), who locates the low-velocity layer in the upper oceanic crust. However, even if a low-velocity layer with 5 % anisotropy is located in the lower continental crust as indicated by Nikulin, Levin, and Park (2009), the resulting difference in time lags should not be more than

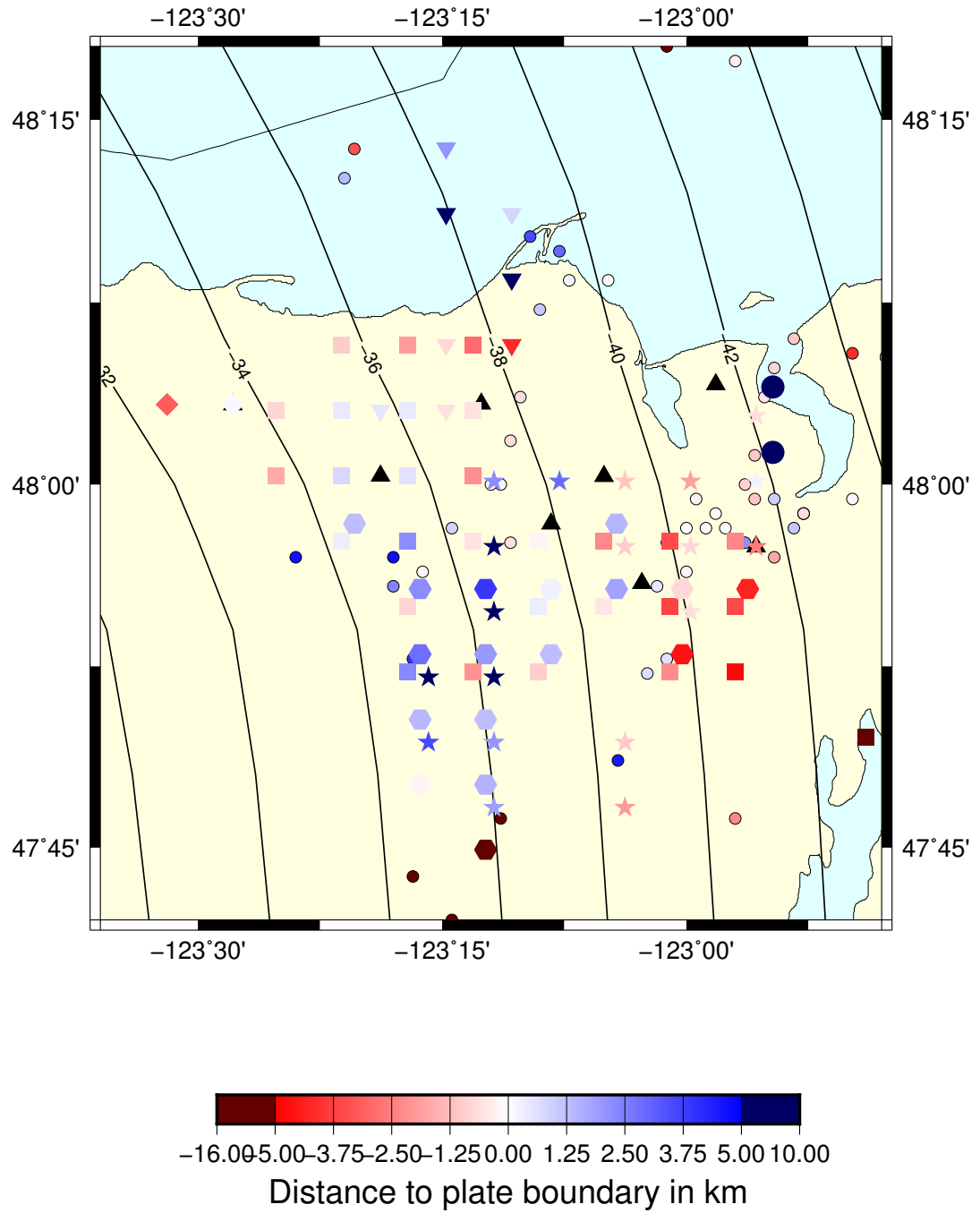


FIGURE 2.8: Map of the distance between the plate boundary (from the Preston model) of the tremor and of the low-frequency earthquake families (filled circles) identified by Sweet et al. (2019) and Chestler and Creager (2017a) and Chestler and Creager (2017b)). Tremor located below the plate boundary is blue, and above is red. Tremor depths are from arrays Burnt Hill (squares), Big Skidder (stars), Danz Ranch (inverted triangles), Gold Creek (large circles), Port Angeles (diamonds), and Three Bumps (hexagons).

a few tenths of a second, and the resulting difference in depth should not be more than 2 kilometers. Cassidy and Bostock (1996) observed anisotropy in the continental crust, especially in the upper 20 kilometers to the north of our arrays. However, the anisotropy resulted in time delays of the seismic waves of no more than 0.32s for deep earthquakes (40-60 km depth) and not more than 0.20s for shallow earthquakes (15-30 km depth). The corresponding difference in tremor depth is similar to the uncertainty.

Several approximations have been made to compute the tremor depth. First, we stacked over all the tremor in 5km by 5km grid cell. The depth difference corresponding to epicentral tremor locations at the center versus the edge of a cell varies from about 1 to 2 km for cells near the array to cells 25 km from an array. Second, the V_p / V_s ratio is not very well known. A variation of about 1% of the V_p / V_s ratio used to compute the depth would lead to a variation of about 1-1.5 km of the corresponding tremor depth (Figure 2.10).

As proposed by Kao et al. (2009), the source of the tremor could be distributed inside a layer that is 15 or more kilometers thick. We have assumed that all the tremor within a given grid cell originate from the same depth, and averaged over all the data to get the tremor depth. However, instead of being located on the same plane near the plate boundary, the tremor may be scattered over a layer surrounding the plate boundary. To compute the thickness of this layer, for each location of the array and the source of the tremor, we computed for each one-minute-long time window for which the cross-correlation function matches well the stacked cross-correlation the time lag between the time corresponding to the maximum absolute value for the cross-correlation function and the time corresponding to the maximum absolute value for the stacked cross-correlation. We thus obtained a distribution of time lags and the corresponding distribution of depths, and we tried to estimate the scale of the interval over which the depths vary. An example of time lags distribution is shown in Figure A.8 of Appendix A. Using the standard deviation could lead to overestimate the width of the interval, and the corresponding thickness of the tremor layer, as the standard deviation is very sensitive to outliers. Instead, we use the Q_n estimator of Rousseeuw and Croux (1993), which is a more robust estimator of scale, similar to the median absolute deviation (MAD). Q_n is equal to the k th order statistic of the $\binom{n}{2}$ interpoint distances where n is the number of points, and $k = \binom{h}{2}$ with $h = [\frac{n}{2}] + 1$ and $[x]$ denote the integer part of x . As the MAD, the Q_n estimator is not very sensitive to outliers, and it has the advantage of being suitable for asymmetric distributions, contrary to the MAD, which attaches equal importance to positive and negative deviations from the median. We then used the scale of the interval over which the tremor depth varies as an estimate of the thickness of the tremor layer (see Figure 2.11). The average thickness of the tremor zone is about 1.6 km, while nearly all the values of the thickness are less than 3km, which is substantially lower than the depth extent from Kao et al. (2009). The smallest values for the thickness are about 0.8-2 kilometers.

Another way of estimating the thickness of the tremor zone is to fit a plane with a linear regression from all the values of the depth and compute the residuals from the regression (Figure 2.12). The Q_n estimator of scale (Rousseeuw and Croux, 1993) for the error between the tremor depth and the fitted plane is only 1.3 km.

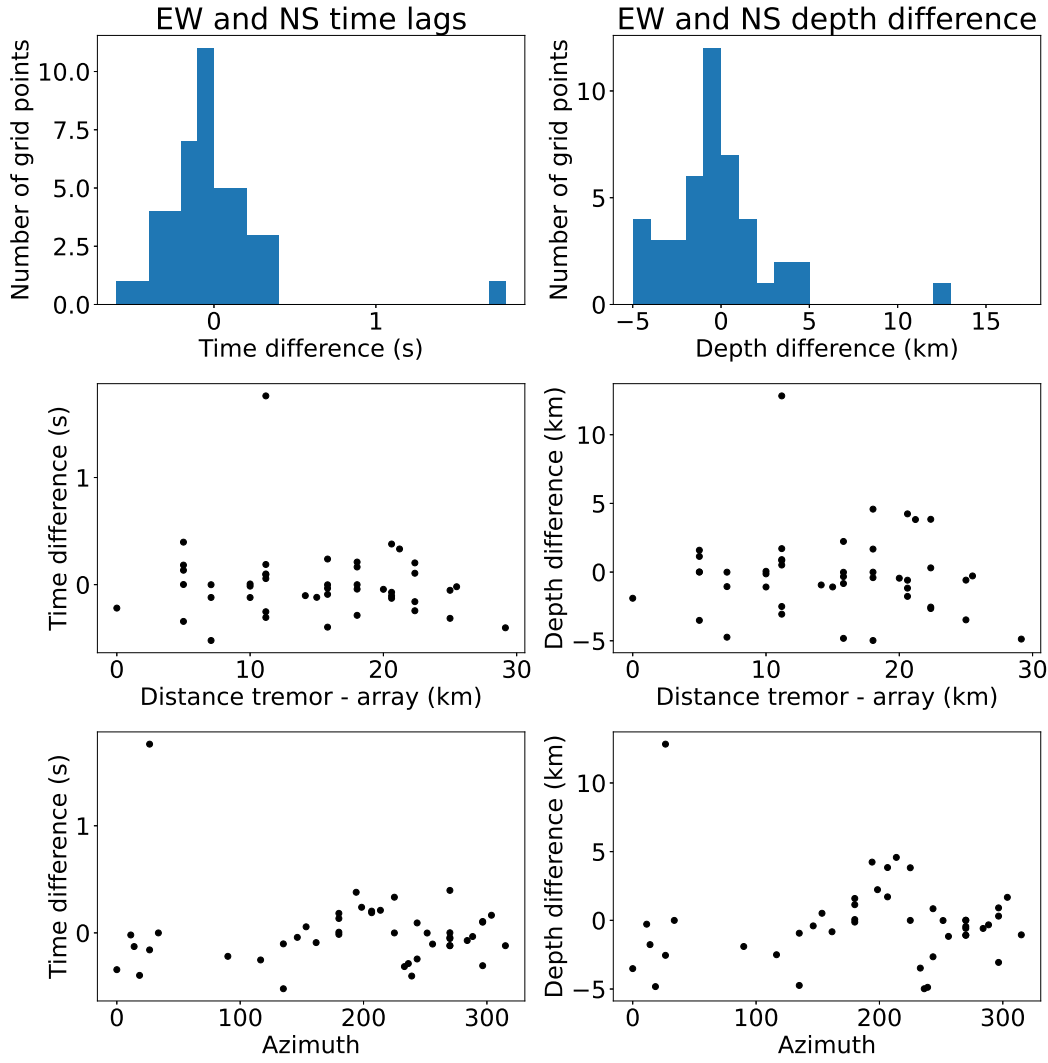


FIGURE 2.9: Left: S-minus-P times measured from envelopes of cross-correlation functions on the East-West component minus those from the North-South component. Right: Corresponding difference in inferred tremor depths. These are plotted as histograms (top), versus epicentral distance between tremors and arrays (middle) and tremor to array azimuth. There is no systematic signal that might be caused by anisotropy.

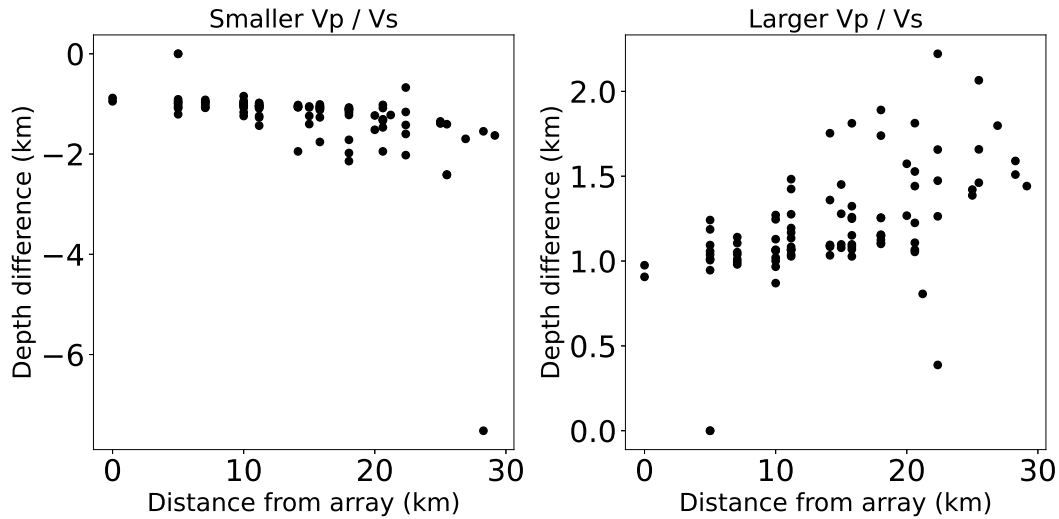


FIGURE 2.10: Variations of the depth of the tremor when we decrease the V_p / V_s ratio by 1% (left) and when we increase the V_p / V_s ratio by 1% (right). A change in the V_p / V_s ratio corresponds to a change in the theoretical time lag between direct P-wave and direct S-wave if the source is located on the plate boundary. Thus, it changes the time interval over which we compute the centroid of the stacked envelopes, and thus the time lag we use to compute the depth.

In Table 2.1, we report the values of the median, the median absolute deviation (MAD), and the Qn estimator of scale for the difference between the depth of the tremor and the low-frequency earthquakes and the depth of the plate boundary, for the McCrory model and for the Preston model. Small negative values of the median correspond to tremor and low-frequency earthquakes located a little bit above the plate boundary. The depth range of the tremor ($Q_n = 1.3$ km) is larger than the depth range of the low-frequency earthquake families from Chestler and Creager (2017a) and Chestler and Creager (2017b) ($Q_n = 0.9$ km). It is also larger than the thickness of the flow channel where Sammis and Bostock (2021) suggest that the LFEs are generated (0.5 to 1.5 km). However, this may be due to the uncertainty on the determination of the tremor depth. The tremor and low-frequency earthquakes are slightly closer to the plate boundary for the Preston model than for the McCrory model. This may be because the P-wave velocity model of Preston et al. (2003) was used as the initial velocity model by Merrill et al. (2020) to compute the full P- and S-wave velocity model that we use to get tremor depth from S minus P times. The Preston P-wave velocity model was also used by Chestler and Creager (2017a) and Chestler and Creager (2017b) to locate the low-frequency earthquake families.

2.6 Conclusion

We developed a method to estimate the depth of the source of the tectonic tremor, and the depth extent of the region from which the tremor originates, using S minus P times determined from lag times of stacked cross-correlations of horizontal and vertical components of seismic recordings from small aperture arrays in the Olympic

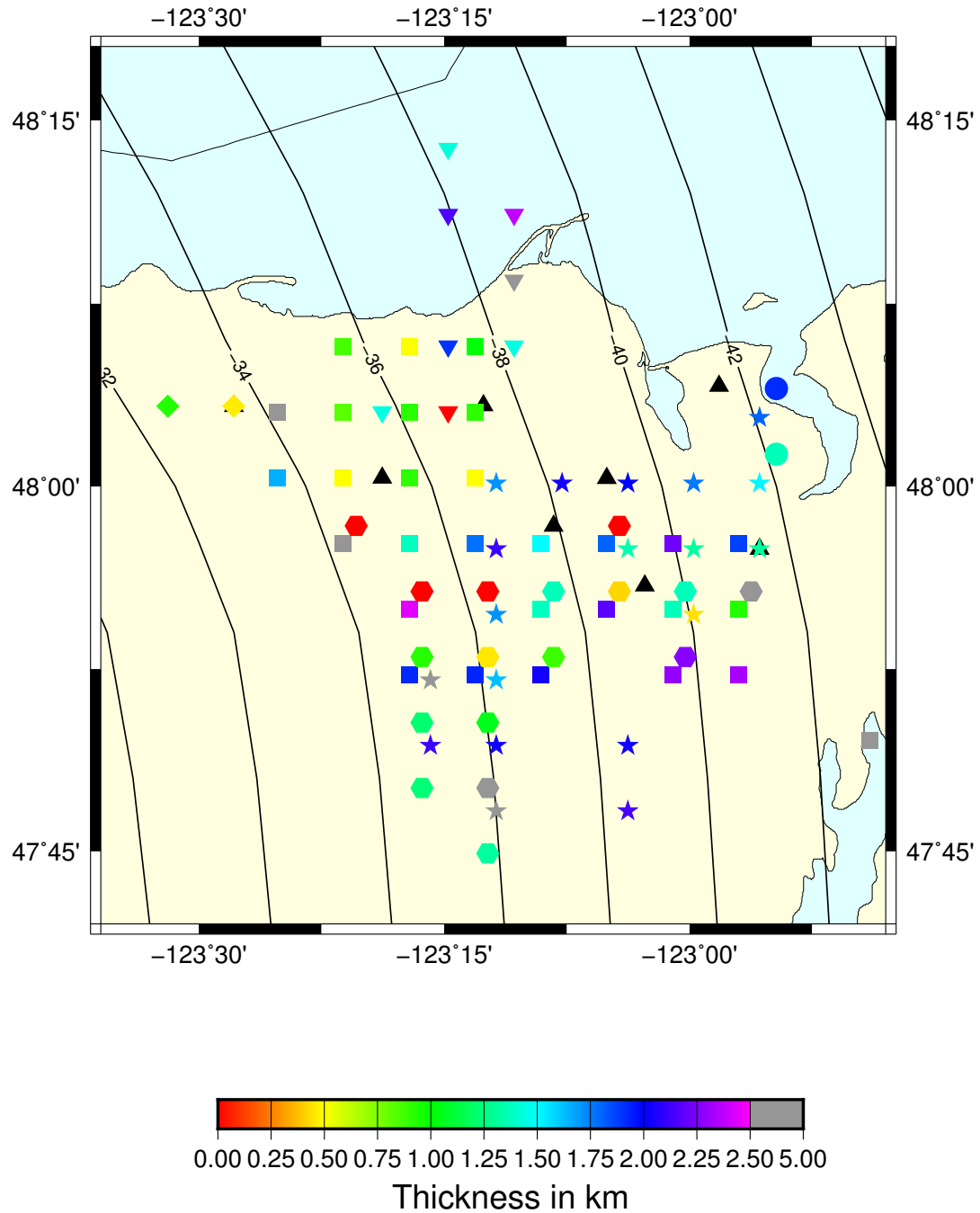


FIGURE 2.11: Map of the thickness of the tremor layer estimated from scatter of individual 1-minute tremor windows. Tremor widths are from arrays Burnt Hill (squares), Big Skidder (stars), Danz Ranch (inverted triangles), Gold Creek (large circles), Port Angeles (diamonds), and Three Bumps (hexagons).

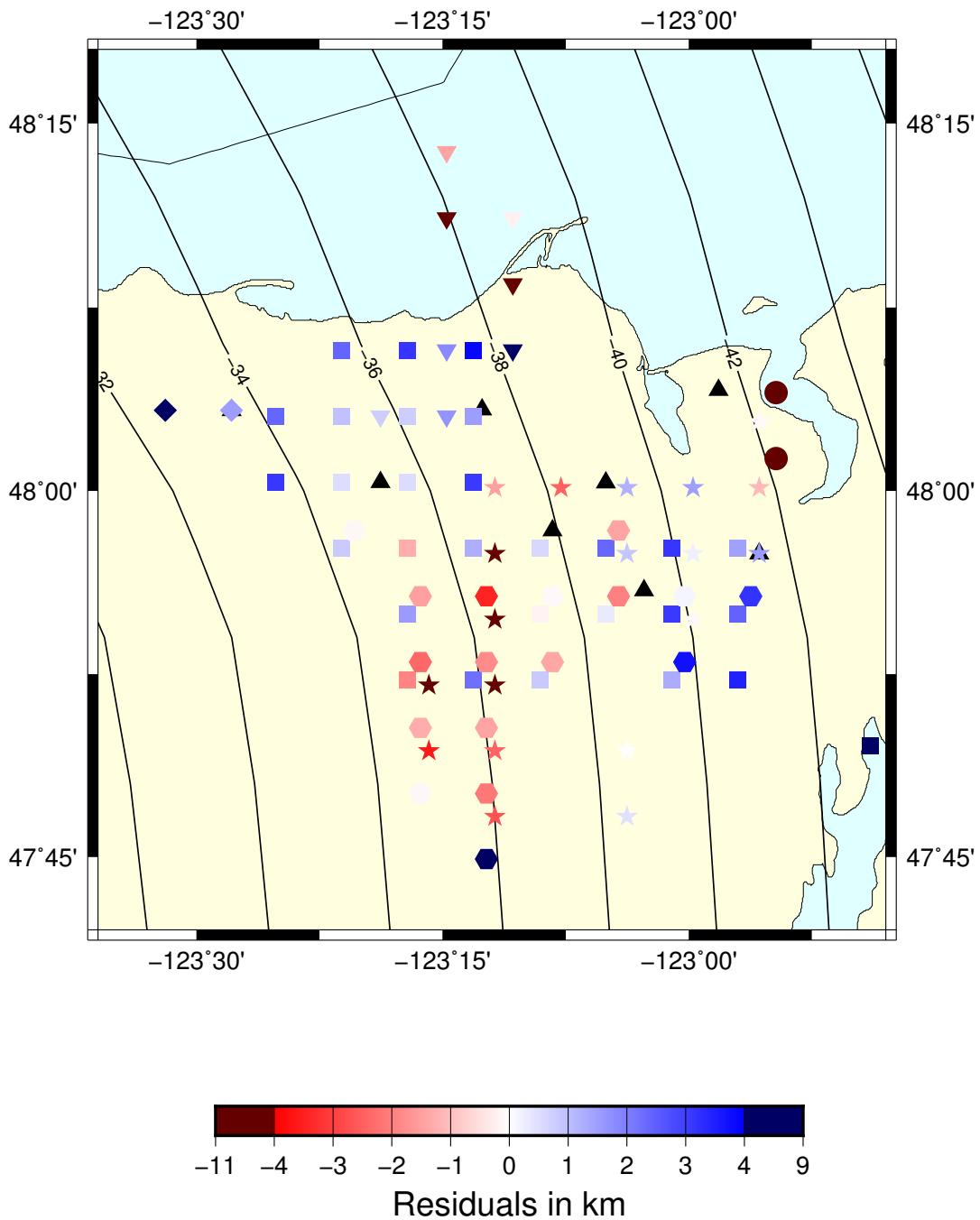


FIGURE 2.12: Map of the residuals from the linear regression fitting all the depths to a plane. Residuals are from arrays Burnt Hill (squares), Big Skidder (stars), Danz Ranch (inverted triangles), Gold Creek (large circles), Port Angeles (diamonds), and Three Bumps (hexagons).

TABLE 2.1: Summary of distances to the plate boundary

	Median	MAD	Qn
Tremor depth - Preston depth	- 0.207 km	2.623 km	1.313 km
Tremor depth - McCrory depth	- 0.850 km	2.429 km	1.390 km
LFE families depth - Preston depth	- 0.189 km	1.312 km	0.871 km
LFE families depth - McCrory depth	- 0.495 km	1.805 km	0.988 km

Peninsula, Washington. We found that the source of the tremor is located close to the plate boundary in a region no more than 2-3 kilometers thick. The source of the tremor is thus distributed over a slightly wider depth range than the low-frequency earthquakes. However, due to the depth uncertainty, it is difficult to conclude whether the tremor is located near the top of the subducting oceanic crust, in the lower continental crust just above the plate boundary, in a layer distributed above and below the plate boundary, or confined to a very narrow plate boundary. The location of the tremor relative to the low-velocity layer also observed near the plate boundary also remains uncertain. Tremor and LFE depths are consistent with filling a volume in the upper subducted crust that is characterized by high fluid pressure and very low S-wave velocities described as the preferred model by Bostock (2013).

Chapter 3

An eight-year-long low-frequency earthquake catalog for Southern Cascadia

Low-frequency earthquakes (LFEs) are small magnitude earthquakes, with typical magnitude less than 2, and reduced amplitudes at frequencies greater than 10 Hz relative to ordinary small earthquakes. Their occurrence is often associated with tectonic tremor and slow-slip events along the plate boundary in subduction zones and occasionally transform fault zones. They are usually grouped into families of events, with all the earthquakes of a given family originating from the same small patch on the plate interface and recurring more or less episodically in a bursty manner. The relatively short recurrence of LFE swarms results in a rich history both in space and time and reveals potential patterns. These event histories could allow scientists to see complete event cycles, which is typically not possible to explore in traditional earthquake catalogs. LFEs can be identified by looking for waveforms repeating simultaneously at several seismic stations. When enough (a few hundred) LFEs have been identified for a given family, a template waveform can be obtained by stacking all the waveforms corresponding to all the LFEs identified. Once a template is available, additional LFEs can be found by cross-correlating seismic data with the template, and assuming that an LFE is occurring whenever the value of the cross-correlation is higher than a chosen threshold. In this chapter, the LFE catalog obtained by Plourde et al. (2015) using seismic recordings from the FAME (EarthScope Flexible Array Mendocino Experiment) network in Northern California during an episode of high tremor activity in April 2008 is used to create templates for the stations of the permanent seismic networks. The one-month-long catalog is then extended to the 8-year period 2004-2011. All of the tremor in the Boyarko et al. (2015) catalog south of 42 degrees North has associated LFE activity, but several other, mostly smaller, clusters of LFEs are identified and their catalog has been extended forward and backward by a total of about 3 years. As in northern Cascadia, the down-dip LFE families have recurrence intervals several times smaller than the up-dip families. For the April, 2008 Episodic Tremor and Slip event, the best recorded LFE families exhibit a strong tidal Coulomb stress sensitivity starting 1.5 days after the rupture front passes by each LFE family. The southernmost LFE family, which has been interpreted to be on the subduction plate boundary, near the up-dip limit of tremor, has a very short recurrence time. Also, these LFEs tend to occur during times when predicted tidal Coulomb stress is discouraging slip on the plate boundary. Both observations suggest this LFE family may be on a different fault.

Research: Solid Earth:

Ducellier, A., & Creager, K. C. An eight-year-long low-frequency earthquake catalog for Southern Cascadia. *Revised manuscript submitted to Journal of Geophysical Research: Solid Earth.*

I would like to thank Alexandre Plourde for sharing his low-frequency earthquake catalog, Devin Boyarko for sharing his tremor catalog, and Heidi Houston for the tidal stress calculation in the Cascadia subduction zone. I would like to thank Alexandre Plourde, an anonymous reviewer and the associate editor whose comments helped improve this chapter. This project was funded by NSF grant EAR-1358512. I would like to thank the Integral Environmental Big Data Research Fund from the College of the Environment of University of Washington, which funded cloud computing resources to carry out the data analyses. The seismic recordings from the FAME experiment used for this analysis can be downloaded from the IRIS website (Levander, 2007). Waveform data from the permanent networks were accessed through the Northern California Earthquake Data Center (NCEDC), doi: 10.7932/NCEDC. The first figure was done using GMT (Wessel and Smith, 1991). All the downloading and preprocessing operations on the seismic waveforms are done with the Python package obspy. The Python scripts used to analyze the data and make the figures can be found on my Github account, accessible through Zenodo (Ducellier, 2022a).

3.1 Introduction

Tectonic tremor is a weak but persistent shaking of the Earth that has been discovered in many subduction zones and some strike-slip faults throughout the world (Beroza and Ide, 2011). Tremor is observed on seismograms as apparent noise whose amplitude is modulated in time in a similar manner at stations that are dozens of kilometers apart from each other (Obara, 2002). It is characterized by a long (several seconds to many minutes), low amplitude seismic signal, emergent onsets, and an absence of clear impulsive phases. Tremor can be explained as a swarm of low-frequency earthquakes (LFEs) (Shelly, Beroza, and Ide, 2007b), that is small magnitude earthquakes ($M \sim 1$) which dominant frequency is clearly low (1-10 Hz) compared with that of ordinary tiny earthquakes (up to 20 Hz). The source of the tremor and the LFEs is located on the plate boundary (Shelly et al., 2006; Bostock et al., 2012; Audet and Kim, 2016), and their focal mechanisms represent shear slip on a low-angle thrust fault dipping in the same direction as the plate interface (Ide, Shelly, and Beroza, 2007; Bostock et al., 2012; Royer and Bostock, 2014). LFEs are usually grouped into families of earthquakes, with all the earthquakes of a given family originating from the same small patch on the plate interface, and recurring more or less episodically in a bursty manner. Dozens of earthquakes are thus recorded within a few hours or days during a burst of LFE activity, followed by weeks or months of quiet, with very few earthquakes. In subduction zones such as Nankai and Cascadia, tectonic tremor and LFE observations are spatially and temporally correlated with slow-slip observations (Rogers and Dragert, 2003; Obara et al., 2004). Due to this correlation, these paired phenomena have been called Episodic Tremor and Slip (ETS).

The relatively short recurrence of slow-slip and tremor events results in a rich history both in space and time and reveals potential patterns. These event histories have allowed scientists to see complete event cycles, which is typically not possible to explore in traditional earthquake catalogs. However, most of the work on LFEs has been focused on detecting LFEs during periods of high tremor activity, grouping them into families of earthquakes, and locating the source of the LFE families. Longer catalogs (several years) have been established for LFE families in Mexico (two-year long catalog by Frank et al. (2014)), the San Andreas Fault (fifteen-year-long catalog by Shelly (2017)), Washington State (five-year-long catalog by Sweet et al. (2019) and two-year-long catalog by Chestler and Creager (2017a) and Chestler and Creager (2017b)), Vancouver Island (ten-year-long catalog by Bostock et al. (2015)), New Zealand (eight-year-long catalog by Baratin et al. (2018)), and Japan (twelve-year-long catalog by Nakamura (2017), eight-year-long catalog by Ohta and Ide (2017), eleven-year-long catalog by Kato and Nakagawa (2020), and Japan Meteorological Agency (JMA) catalog since 1999 (Katsumata and Kamaya, 2003)). These studies have shown that the recurrence behavior of LFE families varies a lot between seismic regions, and inside the same seismic region. In northern Washington, Sweet et al. (2019) have identified and characterized four different LFE families that span the width of the transition zone in the Cascadia Subduction Zone beneath western Washington State. They found that the LFEs swarm duration, recurrence interval, and cluster size decrease systematically with increasing depth. On the San Andreas Fault, Shelly (2017) observed a large diversity of recurrence behaviors among the LFE families, from semicontinuous to highly episodic. Particularly, two families exhibited bimodal recurrence patterns (about 3 and 6 days for the first one, and about 2 and 4 days for the second one). Moreover, he observed an increase in the LFE rate after the 2004 Parkfield earthquake.

Plourde et al. (2015) have detected LFEs in southern Cascadia during the April 2008 ETS event using seismic data from the EarthScope Flexible Array Mendocino Experiment (FAME). They used a combination of autodetection methods and visual identification to obtain the initial templates. Then, they recovered higher signal-to-noise LFE signals using iterative network cross-correlation. They found that the LFE families on the southern Cascadia Subduction Zone were located above the plate boundary model of McCrory et al. (2006), with a large distribution of depths (28-47 km). However, they suggested that this may be because the plate boundary model is biased deep. Three additional LFE families were found on two strike-slip faults, the Maacama and Bucknell Creek faults, which are part of the San Andreas Fault zone.

When the hard work of detecting LFEs and identifying LFE families has been carried out, and enough (a few hundred) LFEs have been identified for a given family, a template waveform can be obtained by stacking all the waveforms corresponding to all the LFEs identified. Once a template is available, additional LFEs can be found by cross-correlating seismic data with the template, and assuming that an LFE is occurring whenever the value of the cross-correlation is higher than a chosen threshold. The signal-to-noise ratios are low, so LFEs can be best identified by stacking the cross-correlation functions of multiple stations. In this study, we first use the catalog established by Plourde et al. (2015) for the months of March and April 2008 to create templates for the temporary seismic stations of the FAME experiment. We then use these templates to extend the catalog to the whole period when the FAME experiment was running, between July 2007 and June 2009. Next, we use the LFE detections from the 2007-2009 period to create templates for the permanent stations

of three seismic networks in northern California. These new templates allow us to extend the LFE catalog to the period 2004-2011.

3.2 Data

We used both seismic data from the temporary EarthScope Flexible Array Mendocino Experiment (FAME) distributed by Incorporated Research Institutions for Seismology (IRIS), and seismic data from three permanent seismic networks distributed by the Northern California Earthquake Data Center (NCEDC). The FAME network was installed in northern California between July 2007 and June 2009. The three permanent networks are Berkeley Digital Seismic Network (BK), Northern California Seismic Network (NC), and Plate Boundary Observatory Strain and Seismic Data (PB). We used both one-component and three-components seismic stations. Depending on availability, we used channels BHZ, EHZ, HHZ, or SHZ as we are mainly interested in the frequency band 1-10Hz. We restricted ourselves to seismic stations less than 100 kilometers away from the epicenter of an LFE family, as we do not expect to have good signal-to-noise ratio for stations located farther away. The complete list of seismic stations and channels used in this study is given in the Appendix B (Tables B1 and B2). Figure 3.1 shows a map of the locations of the LFE families, and of the locations of the seismic stations. We can see that we have a good coverage of the area, and most LFE families are surrounded by several seismic stations.

Plourde et al. (2015) have kindly shared their LFE catalog with us. For each of 66 LFE families they provided hypocentral locations, lists of stations and channels used to detect LFEs, and the timing of all LFE detections. Plourde et al. (2015) have later reduced the number of LFE families to 37, by grouping together families with many common detections, but we chose to use the initial detections to extend the catalog. Using this dataset, we have created LFE templates for each LFE family and each seismic station and channel. For a given LFE family, a given station and a given channel, we downloaded an 80-second-long seismic waveform starting 10 seconds before the LFE detection time, we detrended the data, tapered the first and last 5 seconds of the data with a Hann window, removed the instrument response, bandpassed filter between 1.5 and 9 Hz, resampled the data to 20 Hz, and cut the first and last 10 seconds of data to obtain a one-minute-long template. We then linearly stacked all the waveforms after normalizing each waveform with the root mean square (RMS) to obtain a waveform template for each station and each channel.

3.3 Method

Our ultimate goal is to obtain an eight-year-long LFE catalog using data from permanent seismic networks. The first step is to use the templates from Plourde et al. (2015) and the data from the FAME experiment to get an LFE catalog for 2007-2009. The second step is to use the 2007-2009 FAME catalog to make templates for the seismic stations from the permanent networks. The third step is to use the new templates and the data from the permanent networks to get an LFE catalog for 2004-2011. We used a matched-filter algorithm to detect LFEs. For a given LFE family, we download one hour of seismic data. Then for each station and each channel, we cross-correlate the one-hour long signal with the one-minute-long template for the given station and channel. We scale the correlation coefficient by the standard deviation so the value is 1 if the correlation is perfect. As the signal-to-noise ratio of

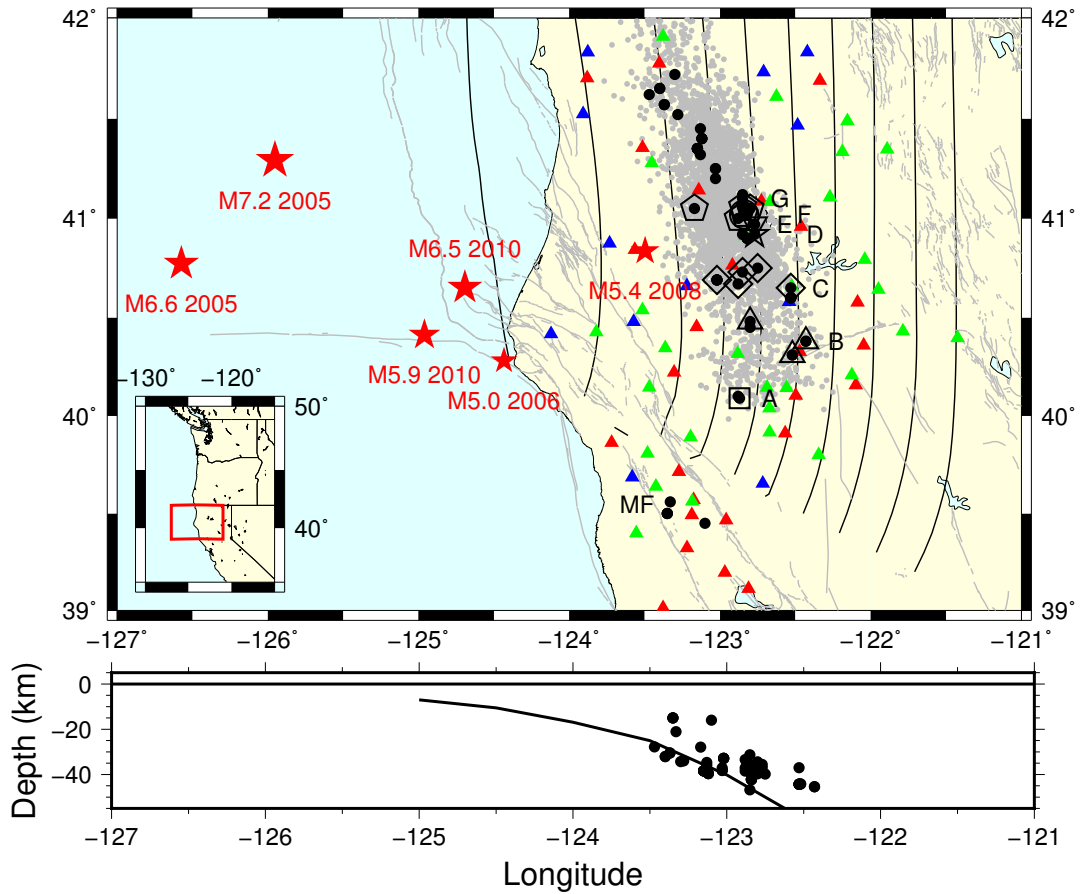


FIGURE 3.1: Map showing the location of the LFE families (black dots) and the seismic stations used in this study. Red triangles are the stations from the FAME experiment, green triangles are one-component permanent stations, blue triangles are three components permanent stations. Red stars are moderate ($M > 5$) nearby earthquakes. The plate boundary from McCrory et al. (2006) is contoured at 10-km intervals starting at 10 km depth. The cross section shows the depth of the LFE families (Plourde et al., 2015) and the plate boundary model from McCrory et al. (2006) at latitude 41 N. MF indicates the Maacama Fault.

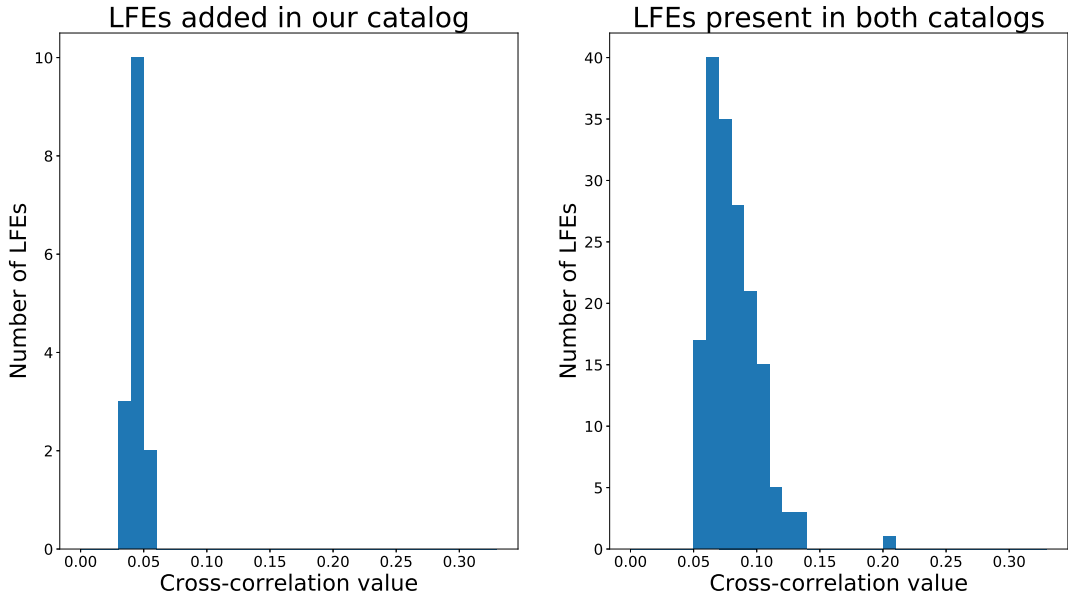


FIGURE 3.2: Cross-correlation values for LFEs added in the catalog for family E (inverted triangle in Figure 3.1) (left) and cross-correlation values for LFEs in the original catalog from Plourde et al. (2015) (right). There were no missing LFEs for this family.

the seismic data is low, we may not see obvious peaks in the cross-correlation signal. However, if we stack the cross-correlation signals for all the channels and all the stations, we can see peaks appearing. Whenever the value of the average cross-correlation is higher than a threshold (we chose a threshold equal to eight times the median absolute deviation of the stacked cross-correlation as was done by Shelly, Beroza, and Ide (2007b)), we inferred that there is an LFE. As two peaks separated by a short period of time may actually correspond to the same LFE, we kept only LFEs that are separated by at least one second and, when two LFEs are separated by less than one second, we keep only the one with the higher value of the stacked cross-correlation.

We first looked for LFEs during the months of March and April 2008, which correspond to the period covered by the catalog from Plourde et al. (2015), and compared our detections with the initial detections from the original catalog of 66 families. For 19 families, we recovered all the LFE detections initially present in the Plourde et al. (2015)'s catalog. For 61 families, we recovered more than 90 % of the initial LFE detections. We also added 74 % more LFEs to the initial number of LFEs in the catalog (when considering all 66 families), but most of added LFEs have a low cross-correlation value and may be false detections. Figure 3.2 shows the cross-correlation values for the LFEs in the original catalog, and for the LFEs that we added to the catalog for family E (inverted triangle in Figure 3.1).

We then looked for LFEs during the period from July 2007 to June 2009, which correspond to the period when the FAME experiment was operating. Using a threshold equal to eight times the median absolute deviation of the stacked cross-correlation may produce false detections, therefore we filtered the LFE detection times before visualizing the two-year-long catalog. As the number of seismic stations recording may change with time as the stations were progressively installed during Summer

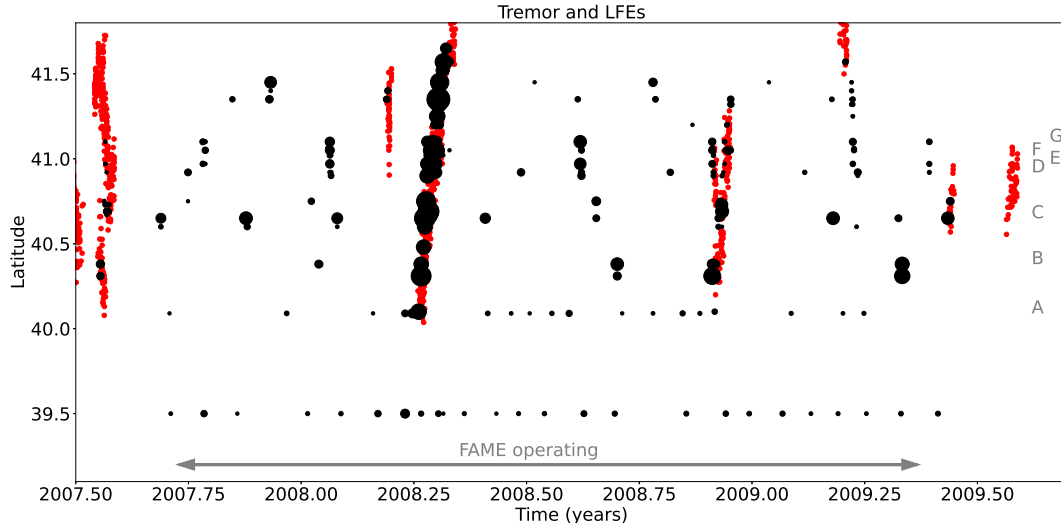


FIGURE 3.3: LFE and tremor detections as a function of time and latitude. Red dots represent tremor detections from the catalog of Boyarko et al. (2015). Black dots represent days where LFEs are detected for a given LFE family. The size of the black dots are proportional to the number of LFEs detected during this day. The double-headed grey arrow represents the time period when the FAME experiment was operating at full capacity. LFE families south of 40N latitude are on the San Andreas fault system. For clarity, we do not show the LFEs for the days when there are less than three LFEs.

and Fall 2007, and then progressively removed during May and June 2009, we kept only LFE detections for which the product of the stacked cross-correlation value by the number of channels recording at that time is higher than a threshold. We will explain later in the text how the threshold is chosen. The threshold is different for each LFE family, but is constant over time for a given LFE family. The resulting LFE catalog for the period 2007-2009 is shown in Figure 3.3. For comparison, we also plotted the tremor detection times from Boyarko et al. (2015). Filtering the catalog has removed about 84 % of the LFEs, compared to the initial catalog where LFEs were detected using the $8 * \text{MAD}$ threshold for the cross-correlation. As a reference, we plotted in the Appendix B (Figure B1) the catalog without filtering the LFEs and the number of channels recording as a function of time (Figure B3).

We note that there is a good spatial and temporal agreement between tremor and LFEs, with LFEs detected during the main tremor episodes. Additional small LFE episodes are also detected between bigger tremor episodes. The LFE families located south on the strike-slip fault from the San Andreas Fault system have much shorter recurrence intervals than the LFE families located on the subduction zone. Additionally, one LFE family located on the southern end of the subduction zone (family A at 40.09N and 34.9km depth) has also shorter recurrence intervals than families located farther north, and behaves more similarly to the strike-slip fault families.

We then used the LFE detections from the 2007-2009 catalog to make new templates for the permanent stations of the three seismic networks: Berkeley Digital Seismic Network (BK), Northern California Seismic Network (NC), and Plate Boundary Observatory Strain and Seismic Data (PB). For a given LFE family, we took the

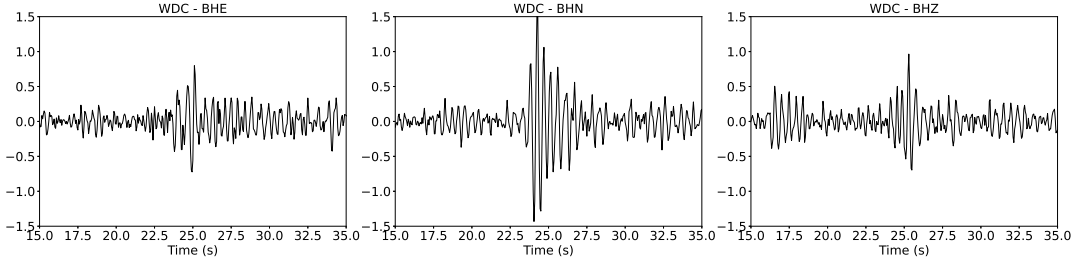


FIGURE 3.4: Low-frequency earthquake template for station WDC and family A (square in Figure 3.1) for the three channels BHE, BHN and BHZ (left to right). We can clearly see a P-wave arrival and an S-wave arrival about 7 seconds later. The P-wave has a higher amplitude on the vertical component, and the S-wave has a higher amplitude on the horizontal components.

150 LFE detection times with the best cross-correlation value, we downloaded one minute of seismic data around each detection, and linearly stacked the waveforms to obtain the templates. We looked for templates for both one-component stations and three-component stations.

For most families, we find that we can obtain good templates with high signal-to-noise ratio for several stations. Only nine families have four or less seismic stations with good templates. Examples of templates are given in Figure 3.4 for station WDC and family A (square in Figure 3.1). To obtain the above catalog, we used one-minute-long templates, which included noise before and after the seismic wave arrivals. To increase the cross-correlation values between the templates and the data, we thus reduced the length of the templates to 25 to 40 seconds, depending on the maximum distance from the source to the stations. The 2007-2009 FAME catalog has thus been established with cross correlations over one-minute-long templates while the 2004-2011 networks catalog has been established with cross correlations over shorter templates with average duration equal to 30 seconds. We did not use stations more than 100 kilometers away from the epicenter of an LFE family, as the template would be unlikely to have a good signal-to-noise ratio. We then used this new, shorter templates for the permanent stations to make an LFE catalog for the period 2007-2009.

3.4 Results

Once we have obtained a catalog for the period 2007-2009 using the data from the permanent seismic networks, we compare the LFE detections between the two catalogs: the FAME catalog (obtained with data from the FAME experiment) and the networks catalog (obtained from data from the permanent networks). As we may have many false detections, we try to eliminate some of them by assuming that LFEs present in both catalogs are always true detections. Then we define two thresholds: the first threshold is chosen such that half the LFE detections above the threshold in the FAME catalog are also in the network catalog, the second threshold is chosen such that half the LFE detections above the threshold (and occurring during 2007-2009) in the network catalog are also in the FAME catalog. If we filter the catalogs

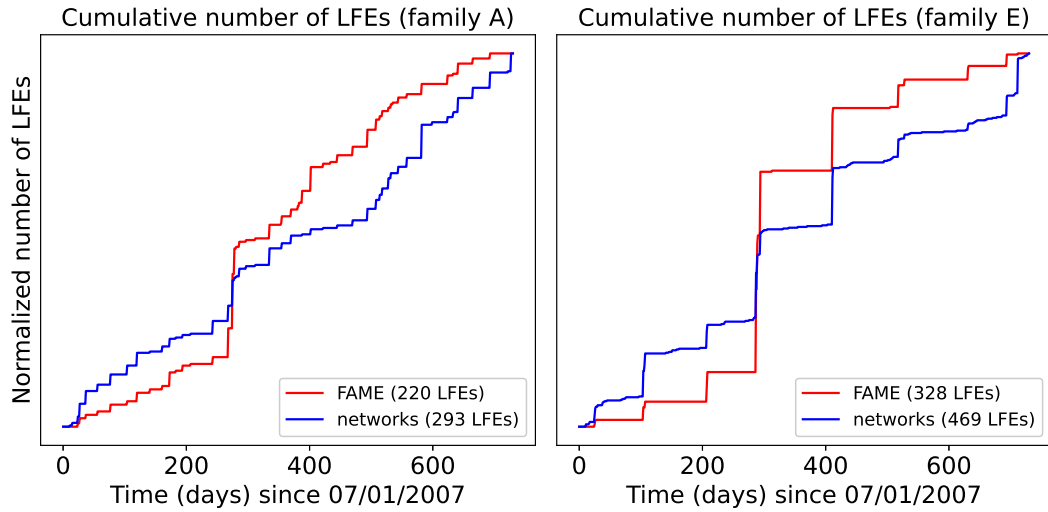


FIGURE 3.5: Normalized cumulative number of LFEs over the period July 2007-July 2009 for the FAME catalog (red) and the network catalog (blue) for family A (square in Figure 3.1) and family E (inverted triangle in Figure 3.1). The cumulative number of LFEs has been divided by the total number of LFEs so that both curves start at 0 and end at 1, in order to get a better match between the LFE bursts in both catalogs.

and keep only detections above the thresholds, we are now confident that at least half of the LFE detections are true detections. Thus there are two thresholds per LFE family (given in Table B3 of the Appendix B). As the number of stations recording may vary over time (especially for the permanent networks catalog), we keep only the LFE detections such that the associated cross correlation multiplied by the number of channels recording at that time is higher than the threshold. Thus, if there are few stations recordings at some time, the cross correlation must be higher for the LFE to be considered as a true detection. We then compared the normalized number of LFEs obtained with the two catalogs. Examples are given in Figure 3.5 for families A (square in Figure 3.1) and E (inverted triangle in Figure 3.1). Although the number of LFEs during each cluster of LFEs may not be the same, we clearly see for family E that the timing of the clusters are the same for both catalogs. Family A has much shorter recurrence times but most clusters of LFEs are present in both catalogs as well: forty clusters are present in both catalogs, three clusters are present in the FAME catalog but not in the networks catalog and one cluster is present in the networks catalog but not in the FAME catalog.

For most of the families located on the subduction zone, we obtained a good agreement between both catalogs. We eliminate six families for which too few permanent stations have good templates, and it was not possible to detect LFEs with the available templates. However, we were able to detect most LFE clusters even without the presence of the temporary stations from the FAME network. We are thus confident that we can detect LFEs before 2007 and after 2009. In the following, we focus on the period 2004-2011. In November 2011, several one-component stations stopped recording and the number of available stations started decreasing, which is why we did not look for LFE after that date. The resulting LFE catalog for the

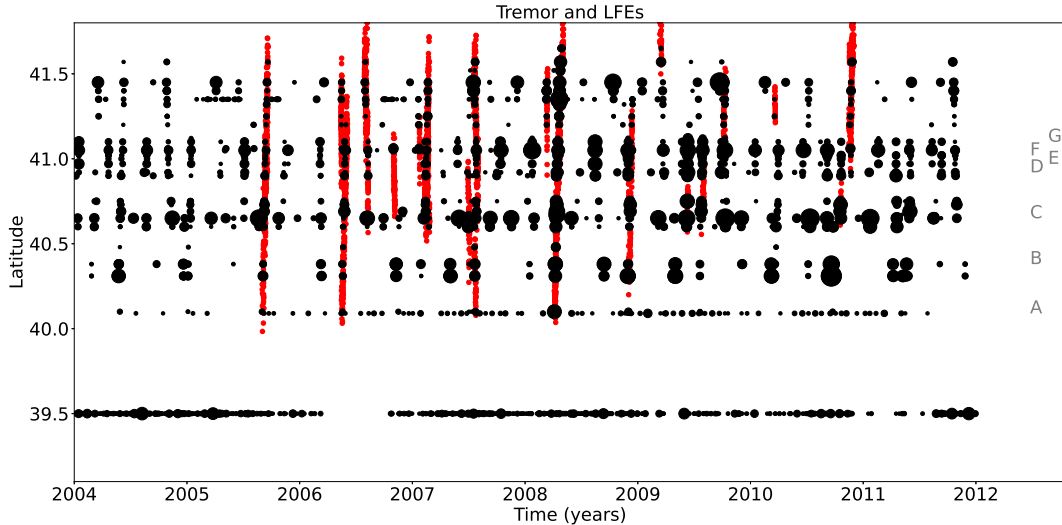


FIGURE 3.6: LFE and tremor detections as a function of time and latitude. Red dots represent tremor detections from the catalog of Boyarko et al. (2015). Black dots represent days where LFEs are detected for a given LFE family. The size of the black dots are proportional to the number of LFEs detected during this day. For clarity, we do not show the LFEs for the days when there are less than three LFEs.

period 2004-2011 is shown in Figure 3.6. For comparison, we also plotted the tremor detection times from Boyarko et al. (2015). Figure 3.7 shows the details of six big ETS events in 2004, 2005, 2006, 2007 and 2008. The catalog shown in Figure 3.6 has been filtered using the threshold computed above. Filtering the catalog has removed about 63 % of the LFEs, compared to the initial catalog where LFEs were detected using the $8 * \text{MAD}$ threshold for the cross-correlation. As a reference, we plotted in the Appendix B (Figure B2) the catalog without filtering the LFEs and the number of channels recording as a function of time (Figure B4).

3.5 Discussion

We were able to detect LFE clusters propagating from North to South or from South to North whenever there is a tremor episode in the Boyarko et al. (2015) catalog. We were also able to detect several LFE episodes in 2004-2005 before the beginning of the Boyarko et al. (2015) catalog. In particular, the LFE episode in January 2005 propagating South to North from latitude 40.1 to latitude 41.2 is also present in the ETS catalog from Brudzinski and Allen (2007). We also see one LFE episode in May-June 2004, propagating South to North from latitude 40.1 to 41.6, and one LFE episode in November 2004, propagating North to South from latitude 41.6 to 40.4. The first of these episodes is also in the ETS catalog from Brudzinski and Allen (2007). The main characteristics of the six biggest episodes shown in Figure 3.7 are given in Table 3.1.

It is known that tectonic tremor can be triggered by surface waves from distant and regional earthquakes, as has been observed in Cascadia (Rubinstein et al., 2009), the San Andreas (Peng et al., 2009; Guilhem, Peng, and Nadeau, 2010), and Nankai

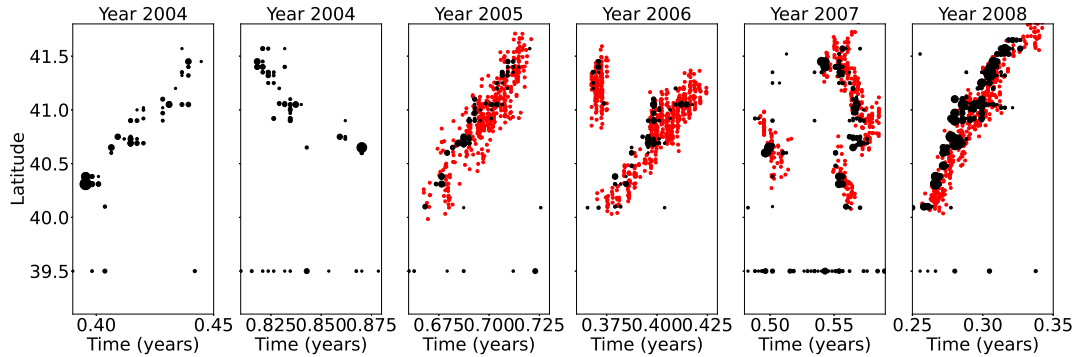


FIGURE 3.7: LFE and tremor detections as a function of time and latitude for six ETS events. Red dots represent tremor detections from the catalog of Boyarko et al. (2015). Black dots represent days where LFEs are detected for a given LFE family. The size of the black dots are proportional to the number of LFEs detected during this day. For clarity, we do not show the LFEs for the days when there are less than three LFEs. The tremor catalog of Boyarko et al. (2015) starts in 2005. This is why no tremor detections can be shown for the two ETS events in 2004.

TABLE 3.1: Main LFEs episodes between 2004 and 2011.

Begin time	End time	Direction	Southern limit	Northern limit
End May 2004	Mid June 2004	South to North	40.1	41.6
Early November 2004	End November 2004	North to South	40.4	41.6
Early September 2005	End September 2005	South to North	40.1	41.6
Mid April 2006	End April 2006	South to North	40.1	41.5
Early July 2007	End July 2007	North to South	40.1	41.6
Early April 2008	End April 2008	South to North	40.1	41.7

(Miyazawa, Brodsky, and Mori, 2008; Han et al., 2014). LFE activity on the San Andreas fault also increased during several months after the 2004 Parkfield earthquake (Shelly, 2017). We looked for regional earthquakes with magnitude higher than 5 during the period covered by the catalog to verify whether this phenomenon is also observed in southern Cascadia. The characteristics of the earthquakes we looked at are given in Table 3.2. We also looked at distant earthquakes with large magnitude, which characteristics are given in Table 3.3.

TABLE 3.2: Nearby regional earthquakes between 2004 and 2011.

Magnitude	Time	Latitude	Longitude	Depth (km)
7.2	2005-06-15 02:50:54	41.292N	125.953W	16.0
6.6	2005-06-17 06:21:42	40.773N	126.574W	12.0
6.5	2010-01-10 00:27:39	40.652N	124.693W	28.7
5.9	2010-02-04 20:20:21	40.412N	124.961W	23.0
5.4	2008-04-30 03:03:06	40.836N	123.497W	27.8
5.0	2006-07-19 11:41:43	40.281N	124.433W	20.1

Although we observe an increase in LFE activity for some families several days after the earthquakes (except the 2008 one where no activity is observed after the

TABLE 3.3: Teleseismic earthquakes between 2004 and 2011.

Magnitude	Time	Latitude	Longitude	Depth (km)
9.1	2011-03-11 05:46:24	38.297N	142.373E	29.0
9.1	2004-12-26 00:58:53	3.295N	95.982E	30.0
8.8	2010-02-27 06:34:11	36.122S	72.898W	22.9
8.6	2005-03-28 16:09:36	2.085N	97.108E	30.0
7.9	2008-05-12 06:28:01	31.002N	103.322E	19.0

earthquake), it does not seem that this activity is linked to the earthquake. Indeed, the LFE clusters occur a few days after the earthquake and not immediately after as is the case for the Parkfield earthquake, and they affect only a few families. The reason may be due to the distance between the LFE families and the epicenters of the regional earthquakes. Indeed, for the Parkfield earthquake, an increase in LFE activity was observed for LFE families up to 45km away from the epicenter, but not farther away. Moreover, the Parkfield earthquake was more shallow (8.1km deep) than the regional earthquakes used in this study. For the 2003 M6.5 San Simeon earthquake, no increase in LFE activity in the San Andreas LFE families was observed in the hours following the earthquake. This was also a shallow earthquake (8.4km deep) but the epicenter was farther away from the LFE families (60 to 100 km). For southern Cascadia, the closest epicenter (2008) is located 50 km away from the closest LFE families. Based on what was observed for the San Andreas LFE families, this distance may be too large for a regional earthquake to trigger an increase in LFE activity. We do not see any change in LFE activity after the large teleseismic earthquakes. There was not any change in LFE activity for the San Andreas LFE families either.

In northern Cascadia, it has been observed that there is an increase in activity downdip of the plate boundary compared to up dip, both for tremor (Wech and Creager, 2011) and LFEs (Sweet et al., 2019). We want to verify whether we can see an increase of LFE activity for the downdip LFE families compared to the up-dip LFE families. Most families in the northern and central part of the study area are well aligned along the strike direction, however families in the southern part of the subduction zone are more distant from each other. We first look at three families aligned at latitude about 40.4N (group B, triangles in Figure 3.1) and show the number of LFEs per day in the left column of Figure 3.8. We then look at five families aligned at latitude about 40.7N (group C, diamonds in Figure 3.1) and show the number of LFEs per day in the middle column of Figure 3.8. Finally, we look at five families aligned at latitude about 41.05N (group G, pentagons in Figure 3.1) and show the number of LFEs per day in the right column of Figure 3.8. For all three sets of families, LFE clusters are more frequent for the easternmost family than for the westernmost family, as was also the case in northern Cascadia (Sweet et al., 2019). It is more difficult to compare cluster size and swarm duration as the number of stations and the quality of the templates are different for each family, and may have a strong influence on the number of LFEs detected. To summarize the findings, we plot in Figure 3.9 the average time between LFE clusters as a function of the distance in the eastern direction from the western limit of the tremor. We assume that there is an LFE cluster every time that at least five LFEs are recorded during a given day. If two clusters are separated by less than five days, we assume that this is a single cluster. We clearly see that the average time between LFE clusters decreases with the down dip distance. The southernmost family A is also added in Figure 3.9, but does

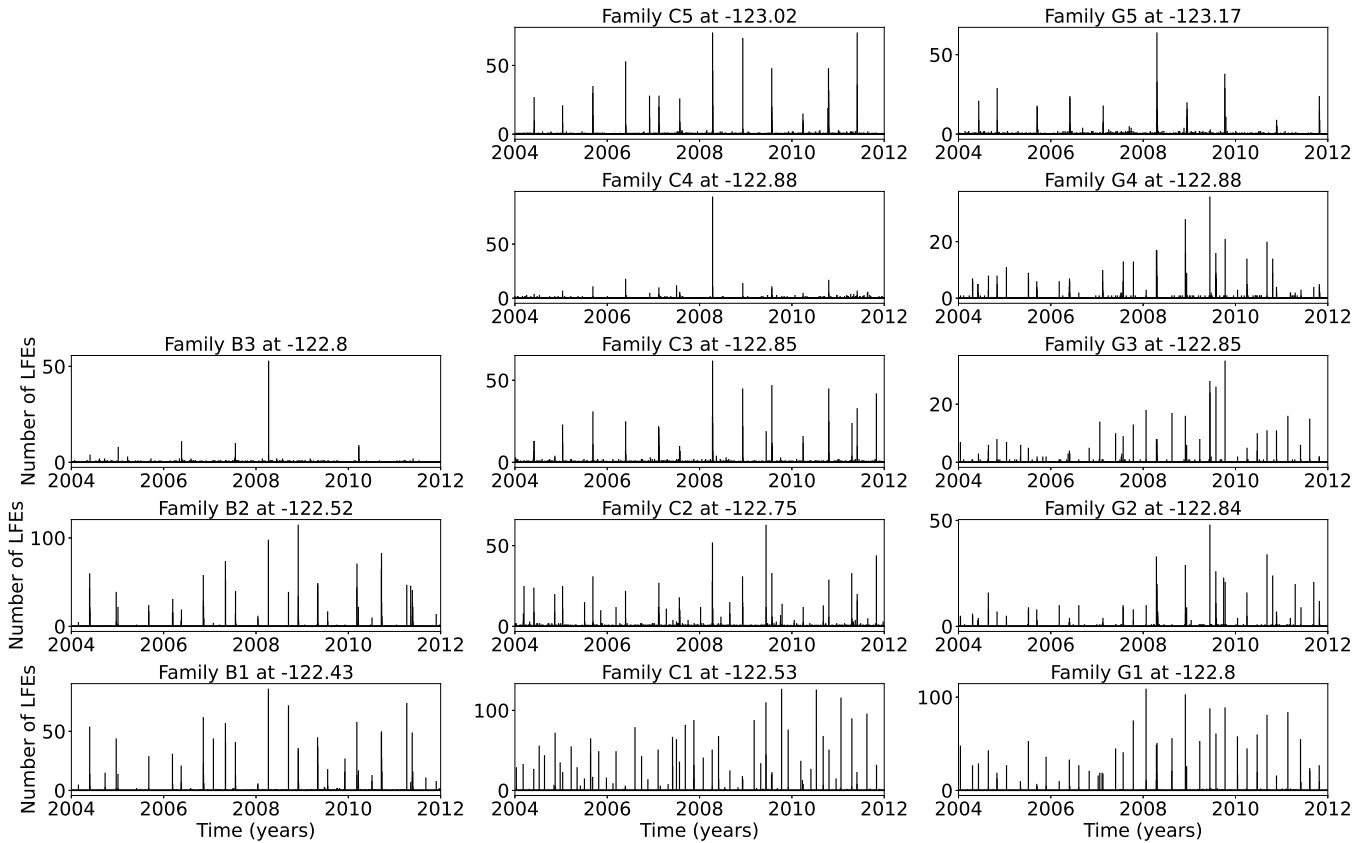


FIGURE 3.8: Left: Daily number of LFEs over the period 2004–2011 for the three LFE families in group C (triangles in Figure 3.1). Middle: Daily number of LFEs for the five LFE families in group D (diamonds in Figure 3.1). Right: Daily number of LFEs for the five LFE families in group E (pentagons in Figure 3.1). Down-dip families (lower rows) typically have far more LFE swarms than up-dip families (upper rows).

not fit the general trend.

The occurrence and amplitude of tectonic tremor can be modulated by small stress changes (about 1 kPa) associated with ocean or solid earth tides (Shelly, Beroza, and Ide, 2007a; Houston et al., 2011; Houston, 2015). Sensitivity of LFE families activity to tidal stress changes has also been observed in northern Cascadia (Royer, Thomas, and Bostock, 2015), and on the San Andreas fault (Thomas et al., 2012). We used calculated stresses from elastic deformations due to both water loads and body tides in the solid Earth along the Cascadia subduction zone. The stress computation is done following the method described in Houston (2015). The resulting full stress tensors are projected to normal and shear (in the plate convergence direction) stresses on the interface, as well as mean stress (one-third the tensor trace). The change in Coulomb stress (positive promotes shear failure) ΔCFF is then computed:

$$\Delta CFF = \Delta\tau + \mu (\Delta\sigma - B\Delta\sigma_m) \quad (3.1)$$

where $\Delta\tau$ is the change in shear stress on the fault plane in the slip direction,

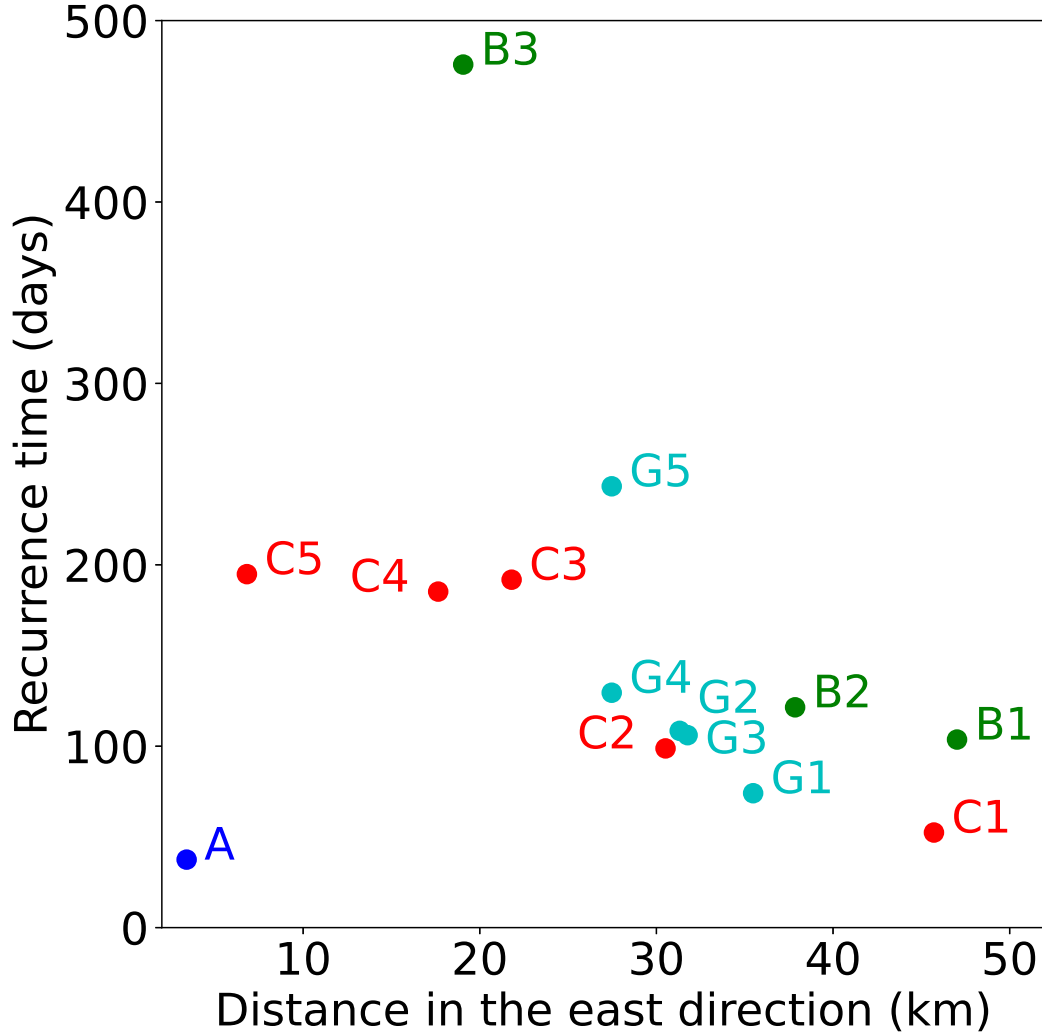


FIGURE 3.9: Average time between LFE clusters as a function of distance in the eastern direction from the westward limit of tremor for the three LFE families in group B (triangles in Figure 3.1), the five LFE families in group C (diamonds in Figure 3.1), and the five LFE families in group G (pentagons in Figure 3.1). Family A (square in Figure 3.1) has much shorter time intervals between LFE clusters.

$\Delta\sigma$ is the change in fault normal stress (positive is tensile), μ is the coefficient of intrinsic friction, $\Delta\sigma_m$ is the change in mean stress and B is the Skempton's coefficient (Houston, 2015). We take the values $\mu = 0.1$ and $B = 0.5$ for the friction and the Skempton's coefficient, as was done by Houston (2015). We then divided the values of tidal Coulomb stress change into 20 stress bins and computed for each LFE family the number of LFEs occurring at a time when the value of the stress was in a given bin. We also computed what would be the expected number of LFEs occurring if the tidal stress changes have no influence on LFE activity. As noted by Houston (2015), tremor sensitivity to stress perturbations changes during an ETS event, with an increase in sensitivity to tidal stress as slip accumulates over several days. We thus choose to only consider the later part of the 2008 ETS event, using only LFEs that occurred between 1.5 and 11.5 days after the arrival of the tremor front. As there are only a few LFEs, it is not always obvious to see the influence of tidal stress on LFE activity. However, Figure 3.10 shows the number of LFEs occurring during each stress bin (blue bars) and the expected number of LFEs (black line) for six families with a relatively high number of LFEs. For most of the families, a positive Coulomb stress change (promoting shear failure) is associated with an increase in LFE activity. However, this is not the case for the southernmost LFE family A, for which a negative Coulomb stress change is associated with an increase in LFE activity. To better highlight the behavior of family A, we also consider the whole LFE catalog and plot the observed and expected number of LFEs as a function of tidal stress. We clearly see that these LFEs tend to occur during times when predicted tidal Coulomb stress is discouraging slip on the plate boundary. We tried to relocate this LFE family using new templates obtained from LFEs present in both the 2007-2009 FAME catalog and the 2004-2011 networks catalog. We locate the family using S minus P times for each station, or using P-P times between stations, or using a combination of both. The family may be located 30 to 50 kilometers east from the initial location given by Plourde et al. (2015). The depth is 20-25 kilometers, that is shallower than the location given by Plourde et al. (2015) and shallower than the plate boundary. However, this does not change the pattern observed for the correlation between tidal stress changes and LFE activity. We hypothesize that LFE family A may not be located on the subduction zone and may be on a nearby crustal fault. If this was the case, the fault plane assumed for the tidal stress calculation would not be appropriate, which would explain the different pattern for this LFE family. The LFE families located on the San Andreas fault by Shelly (2017) have a depth of 15 to 30 kilometers, so the depth of the LFE family A is compatible with a location on a crustal fault.

3.6 Conclusion

In this study, we used the templates obtained by Plourde et al. (2015) using data recorded by the FAME network in Northern California during an episode of high tremor activity in April 2008, and we extended their catalog to the whole two years (2007-2009) during which the seismic stations were installed. We then used the two-year-long catalog to create templates for stations from the permanent seismic networks, and used the seismic data recorded by these stations to extend the catalog before and after the FAME experiment. We observe LFEs every time that there is tectonic tremor on the tremor catalog from Boyarko et al. (2015), and several additional smaller LFE episodes. Whereas the LFE families from the subduction zone are mainly active during the big Episodic Tremor and Slip events, the southernmost

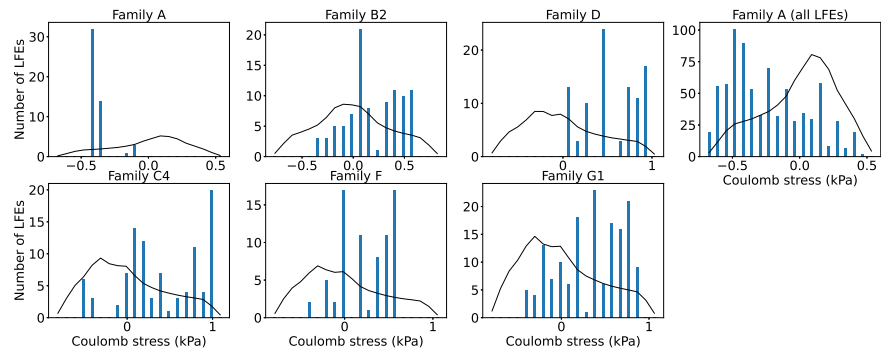


FIGURE 3.10: Number of LFEs for families A, B2, D, C4, F and G1 observed (blue bars) and expected (black line) for each stress bin of tidal Coulomb stress change

family is more active, with repeating events about once a month. Downdip families are also more active than up dip families. Tidal stress changes seem to be correlated with LFE activity in the later part of the 2008 ETS event.

Chapter 4

Detection of slow-slip events using wavelet analysis of GNSS recordings

As ordinary earthquakes, slow-slip events are caused by slip on a fault (e.g. the plate boundary between a tectonic plate subducting under another tectonic plate). However, they take a much longer time (several days to several years) to happen relative to ordinary earthquakes, and the seismic waves they generate are much weaker than the seismic waves generated by ordinary earthquakes, and may not be detectable. A slow-slip event on the plate boundary is inferred to happen when there is a reversal of the direction of motion at Global Navigation Satellite System (GNSS) stations, compared to the inter-seismic surface displacement. In many places, tectonic tremor is observed in relation to slow-slip and can be used as a proxy to study slow-slip events of moderate magnitude where surface deformation is hidden in GNSS noise. However, there are regions where there is no clear relationship between tremor and slow-slip occurrence. For instance, in northern New Zealand, the tremor activity does not seem to increase during the slow-slip events, and seem to be located downdip of the geodetically inferred slip area. In regions where no clear relationship between tremor and slow-slip occurrence is observed, tremor-based methods to detect slow-slip cannot be applied, and we need other methods to be able to better detect and quantify slow-slip. Wavelets methods such as the Discrete Wavelet Transform (DWT) and the Maximal Overlap Discrete Wavelet Transform (MODWT) are mathematical tools for analyzing time series simultaneously in the time and the frequency domain by observing how weighted differences of a time series vary from one period to the next. In this chapter, wavelet methods are used to analyze GNSS time series and seismic recordings of slow-slip events in Cascadia. A MODWT transform is applied to the detrended GNSS data and the wavelet details are stacked over several nearby GNSS stations. As an independent check on the timing of slow-slip events, the cumulative number of tremor in the vicinity of the GNSS stations is computed, detrended, and transformed using the MODWT. In both time series, there are simultaneous waveforms whose timing corresponds to the timing of slow-slip events. A slow-slip event is assumed to happen whenever there is a positive peak followed by a negative peak in the wavelet signal. There is a good correlation between slow-slip events detected with only GNSS data, and slow-slip events detected with only tremor data for northern Cascadia. The wavelet-based detection method detects well events of magnitude higher than 6 as determined by independent event catalogs (e.g. (Michel, Gualandi, and Avouac, 2019)).

This chapter is currently under revision for Bulletin of the Seismological Society

of America:

Ducellier, A., Creager, K. C., & Schmidt, D. A. - Detection of slow-slip events using wavelet analysis of GNSS recordings. *In revision for Bulletin of the Seismological Society of America.*

This work was funded by the grant from the National Science Foundation EAR-1358512. I would like to thank Professor Donald Percival for introducing me to wavelet methods during his excellent class on Wavelets: Data Analysis, Algorithms and Theory taught at University of Washington. The GPS recordings used for this analysis can be downloaded from the PANGA website (GPS/GNSS Network and Geodesy Laboratory: Central Washington University, other / seismic network, 1996). The Python scripts used to analyze the data and make the figures can be found on my Github account (Ducellier, 2022b). Figure 4.4 was created using GMT (Wessel and Smith, 1991).

4.1 Introduction

slow-slip events are a new feature discovered in the last two decades in many subduction zones thanks to recordings of the displacement of Earth's surface by dense Global Navigation Satellite System (GNSS) networks. As with ordinary earthquakes, slow-slip events represent slip on a fault, for instance the plate boundary between a tectonic plate subducting under another tectonic plate. However, they take a much longer time (several days to several years) to happen relative to ordinary earthquakes. They have a relatively short recurrence time (months to years) compared to the recurrence time of regular earthquakes (up to several hundreds of years), allowing scientists to observe and study many complete event cycles, which is typically not possible to explore with traditional earthquake catalogs (Beroza and Ide, 2011). A slow-slip event on the plate boundary is inferred to happen when there is a reversal of the direction of motion at GNSS stations, compared to the secular interseismic motion. slow-slip events have been observed in many places, such as Cascadia, Nankai (southwest Japan), Alaska, Costa Rica, Mexico, and New Zealand (Beroza and Ide, 2011; Audet and Kim, 2016).

In many places, tectonic tremor is also observed in relation to slow-slip, but it is more abundant in some places. Tremor is a long (several seconds to many minutes), low amplitude seismic signal, with emergent onsets, and an absence of clear impulsive phases. Tectonic tremor have been explained as a swarm of small, low-frequency earthquakes (LFEs) (Shelly, Beroza, and Ide, 2007b), which are small magnitude earthquakes ($M \sim 1$) for which frequency content (1-10 Hz) is lower than for ordinary earthquakes (up to 20 Hz). In subduction zones such as Nankai and Cascadia, tectonic tremor observations are spatially and temporally correlated with slow-slip observations (Obara, 2002; Rogers and Dragert, 2003). Due to this correlation, these paired phenomena have been called Episodic Tremor and Slip (ETS). However, this is not always the case. For instance, in northern New Zealand, tremor are more challenging to detect, and seem to be located downdip of the slow-slip on the plate boundary (Todd and Schwartz, 2016). In Alaska, the tremor zone only partially overlaps the long-term slow-slip zone and there does not appear to be any temporal correlation between tremor and slow-slip occurrence (Wech, 2016).

In Cascadia, there are robust signals in both GNSS and tremor. This is also the case in Nankai, where tiltmeters are used instead of GNSS. It is thus possible to use tremor as a proxy to observe slow-slip events that are not directly observed in the GNSS data. For instance, Aguiar, Melbourne, and Scrivner (2009) studied 23 ETS events in Cascadia with more than 50 hours of tectonic tremor. For all these events, they computed both the GPS-estimated moment release and the cumulative number of hours of tectonic tremor recorded. They observed a linear relationship between moment release and number of hours of tremor for ETS events of moment magnitude 6.3 to 6.8. Based on this linear relationship, it is possible to infer the existence of smaller slow-slip events of magnitude 5-6 occurring simultaneously with smaller tremor bursts of duration 1 to 50 hours occurring in between the big ETS events, and for which there is no detectable signal in the GPS data.

Frank (2016) divided GPS time series observations from Cascadia and Guerrero, Mexico, into two groups: the first group contains days with abundant tremor and LFEs, the second group contains days when the number of tremor or LFEs is lower than a threshold. He then stacked separately the two groups of daily observations and observed a cumulative displacement in the direction corresponding to the loading period when few tremor or LFEs are observed and the surface deformation corresponds to the secular plate motion. He also observed a cumulative displacement in the opposite direction corresponding to the release period when tremor and LFEs are observed. He was thus able to observe a reverse displacement corresponding to smaller slow-slip events not directly observable in the GPS data for individual events.

However, these methods cannot be applied to detect slow-slip events in places where tremor and slow-slip occurrence are not well spatially and temporally correlated, tremor is not abundant, or the seismic network is not robust enough. We thus need other methods to be able to better detect and quantify slow-slip.

Wavelets methods such as the Discrete Wavelet Transform (DWT) are mathematical tools for analyzing time series simultaneously in the time and the frequency domain by observing how weighted differences of a time series vary from one period to the next. Wavelet methods have been widely used for geophysical applications (e.g. (Kumar and Foufoula-Georgiou, 1997)). However, few studies have used wavelet methods to analyze recordings of slow-slip, and their scope was limited to the detection of the bigger (magnitude 6-7) short-term (a few weeks) events (Szeliga et al., 2008; Ohtani, McGuire, and Segall, 2010; Wei, McGuire, and Richardson, 2012; Alba et al., 2019).

Szeliga et al. (2008) determined the timing and the amplitude of 34 slow-slip events throughout the Cascadia subduction zone between 1997 and 2005 using wavelets. They modeled the GPS time series by the sum of a linear trend, annual and biannual sinusoids representing seasonal effects, Heaviside step functions corresponding to earthquakes and hardware upgrades, and a residual signal. They then applied a Gaussian wavelet transform to the residual time series to get the exact timing of slow-slip at each GPS station. The idea is that the wavelet transform allows us to analyze the signal both in the time and the frequency domains. A sharp change in the signal will be localized and seen at all levels of the wavelet decomposition, contrary to what happens with the periodic sinusoids of the Fourier transform.

Instead of using wavelets in the time domain, Ohtani, McGuire, and Segall (2010) used 2D wavelet functions in the spatial domain to detect slow-slip events. They designed the Network Stain Filter (NSF) to detect transient deformation signals from large-scale geodetic arrays. They modeled the position of the GPS station by the sum of the secular velocity, a spatially coherent field, site-specific noise, reference frame errors, and observation errors. The spatial displacement field is modeled by the sum of basis wavelets with time-varying weights. Their method has been successfully used to detect a transient event in the Boso peninsula, Japan, and a slow-slip event in the Alaska subduction zone (Wei, McGuire, and Richardson, 2012).

Finally, Alba et al. (2019) used hourly water level records from four tide gauges in the Juan de Fuca Straight and the Puget Sound to determine relative vertical displacements associated with ETS events between 1996 and 2011. Their main idea is that the tidal level measured at a given gauge is the sum of a noise component at multiple timescales (tides, ocean and atmospheric noise) and an uplift signal due to the ETS events. The noise component is assumed to be coherent between all tidal gauges, while the tectonic uplift signal is different provided that the gauges are far enough from each other. By stacking the tidal records after removing tides, the uplift signals cancel each other while the noise signal is amplified. By stacking the details of the DWT decomposition, instead of stacking the raw tidal record, each of the components of the noise at different time scales is retrieved and can then be removed from the raw records to obtain the uplift signal. The authors were then able to clearly see a difference in uplift between the two tidal gauges at Port Angeles and Port Townsend.

In our study, we use a similar approach to previous studies with a different reasoning. We only stack signals at nearby GPS stations, assuming that the longitudinal displacement due to the ETS events will then be the same at each of the GPS stations considered. We suppose that some of the noise component is different at each GPS station and will be eliminated by the stacking. Finally, we assume that the noise and the longitudinal displacement due to the ETS events and the secular plate motion have different time scales, so that the wavelet decomposition will act as a bandpass filter to retrieve the displacement signal and highlight the ETS events. We use wavelet methods to analyze GPS and tremor recordings of slow-slip events in Cascadia. Our objective is to verify that there is a good correlation between slow-slip events detected with only GNSS data, and slow-slip events detected with only tremor data. We thus want to demonstrate that the wavelet-based detection method can be applied to detect slow-slip events that may currently be obscured using standard methods.

4.2 Data

We focused our study on northwest Washington State. For the GNSS data, we used the GPS time series provided by the Pacific Northwest Geodetic Array, Central Washington University. These are network solutions in ITRF2008 with phase ambiguities resolved. Solutions are computed with JPL/NASA orbits and satellite clocks. North, East, and Vertical directions are available. However, as the direction of the secular plate motion is close to the East direction, we only used the East direction of the GPS time series for the data analysis, as it has the best signal-to-noise ratio.

The wavelet method works best with data with zero mean, and no sharp discontinuities; so we use the cleaned dataset, that is GPS times series with linear trends, steps due to earthquakes or hardware upgrades, and annual and semi-annual sinusoids signals simultaneously estimated and removed following Szeliga et al. (2004). For the tremor data, we used the tremor catalog from the Pacific Northwest Seismic Network (PNSN) (Wech, 2010).

4.3 Method

4.3.1 The Maximal Overlap Discrete Wavelet Transform

The Discrete Wavelet Transform (DWT) is an orthonormal transform that transforms a time series X_t with $t = 0, \dots, N - 1$ into a vector of wavelet coefficients W_i with $i = 0, \dots, N - 1$. If we denote J the level of the wavelet decomposition, and the number of observations is equal to $N = n * 2^J$, where n is some integer higher or equal to 1, the vector of wavelet coefficients can be decomposed into J wavelet vectors W_j of lengths $\frac{N}{2}, \frac{N}{4}, \dots, \frac{N}{2^J}$, and one scaling vector V_J of length $\frac{N}{2^J}$. Each wavelet vector W_j is associated with changes on time scale $\tau_j = dt2^{j-1}$, where dt is the time step of the time series, and corresponds to the filtering of the original time series with a filter with nominal frequency interval $[\frac{1}{dt2^{j+1}}, \frac{1}{dt2^j}]$. The scaling vector V_J is associated with averages in time scale $\lambda_J = dt2^J$, and corresponds to the filtering of the original time series with a filter with nominal frequency interval $[0, \frac{1}{dt2^{J+1}}]$. Wavelet vectors can be further decomposed into details and smooths, which are more easily interpretable. We define for $j = 1, \dots, J$ the j th wavelet detail D_j , which is a vector of length N , and is associated to time scale $\tau_j = dt2^{j-1}$. Similarly, we can define for $j = 1, \dots, J$ the j th wavelet smooth S_j , which is a vector of length N , and is associated to scales $\tau_{j+1} = dt2^{j+1}$ and higher. The basic idea is to reapply to W_j the wavelet filter that was used to construct W_j from the initial time series X . Together, the details and the smooths define the multiresolution analysis (MRA) of X :

$$X = \sum_{j=1}^J D_j + S_J \quad (4.1)$$

The DWT presents several disadvantages. First, the length of the time series must be a multiple of 2^J where J is the level of the DWT decomposition. Second, the time step of the wavelet vector W_j is $dt2^j$, which may not correspond to the time when some interesting phenomenon is visible on the original time series. Third, when we circularly shift the time series, the corresponding wavelet coefficients, details and smooths are not a circularly shifted version of the wavelet coefficients, details and smooths of the original time series. Thus, the values of the wavelet coefficients, details and smooths are strongly dependent on the time when we start experimentally gathering the data. Finally, when we filter the time series to obtain the details D_j and smooths S_j , we introduce a phase shift, which makes it difficult to line up meaningfully the features of the MRA with the original time series.

To overcome the disadvantages described above, we use instead the Maximal Overlap Discrete Wavelet Transform (MODWT). The MODWT transforms the time series X_t ($t = 0, \dots, N - 1$) into J wavelet vectors \tilde{W}_j ($j = 1, \dots, J$) of length N and a scaling vector \tilde{V}_J of length N . As is the case for the DWT, each wavelet vector \tilde{W}_j

is associated with changes on scale $\tau_j = dt2^{j-1}$, and corresponds to the filtering of the original time series with a filter with nominal frequency interval $[\frac{1}{dt2^{j+1}}; \frac{1}{dt2^j}]$. The scaling vector \tilde{V}_j is associated with averages in scale $\lambda_j = dt2^j$, and corresponds to the filtering of the original time series with a filter with nominal frequency interval $[0; \frac{1}{dt2^{j+1}}]$. As is the case for the DWT, we can write the MRA:

$$X = \sum_{j=1}^J \tilde{D}_j + \tilde{S}_j \quad (4.2)$$

The MODWT of a time series can be defined for any length N . The time step of the wavelet vectors \tilde{W}_j and the scaling vector \tilde{V}_j is equal to the time step of the original time series. When we circularly shift the time series, the corresponding wavelet vectors, scaling vector, details and smooths are shifted by the same amount. The details and smooths are associated with a zero phase filter, making it easy to line up meaningfully the features of the MRA with the original time series. The wavelet methods for time series analysis are explained in a more detailed way in (Percival and Walden, 2000)).

4.3.2 Application to synthetic data

To illustrate the wavelet transform method, we first apply the MODWT to synthetic data. As slow-slip events occur in Cascadia on a regular basis, every twelve to eighteen months, we create a synthetic signal of period $T = 500$ days. To reproduce the ground displacement observed on the longitudinal component of GPS stations in Cascadia, we divide each period into two parts: In the first part of duration $T - N$, the displacement is linearly increasing and corresponds to the inter seismic plate motion in the eastern direction; in the second part of duration N , the displacement is linearly decreasing and corresponds to a slow-slip event on a reverse fault at depth triggering a ground displacement in the western direction. To see the effect of the duration of the slow-slip event, we use different values for $N = 5, 10, 20, 40$ days. The amplitude of the set is normalized to 1. Figure 4.1 shows the synthetics, the details D_j of the wavelet decomposition for levels 1 to 10, and the smooth S_{10} for the four durations of a slow-slip event.

The ramp-like signal is transformed through the wavelet filtering into a waveform with first a positive peak and then a negative peak. The shape of the waveform is the same for every level of the wavelet decomposition, but the width of the waveform increases with the scale level. For the 8th level of the wavelet decomposition, the width of the waveform is nearly as large as the time between two events. At larger scales, the waveforms start to merge two contiguous events together, and make the wavelet decomposition less interpretable. For an event of duration 5 days, the wavelet details at levels higher than 3 have a larger amplitude than the wavelet details at lower scales. For an event of duration 10 days, the wavelet details at levels higher than 4 have a larger amplitude than the wavelet details at lower scales. For an event of duration 20 days, the wavelet details at levels higher than 5 have a larger amplitude than the wavelet details at lower scales. For an event of duration 40 days, the wavelet details at levels higher than 6 have a larger amplitude than the wavelet details at lower scales. Thus, the scale levels at which an event is being seen in the wavelet details give us an indication about the duration (and the magnitude) of the slow-slip event. The big slow-slip events of magnitude 6-7 typically trigger a signal

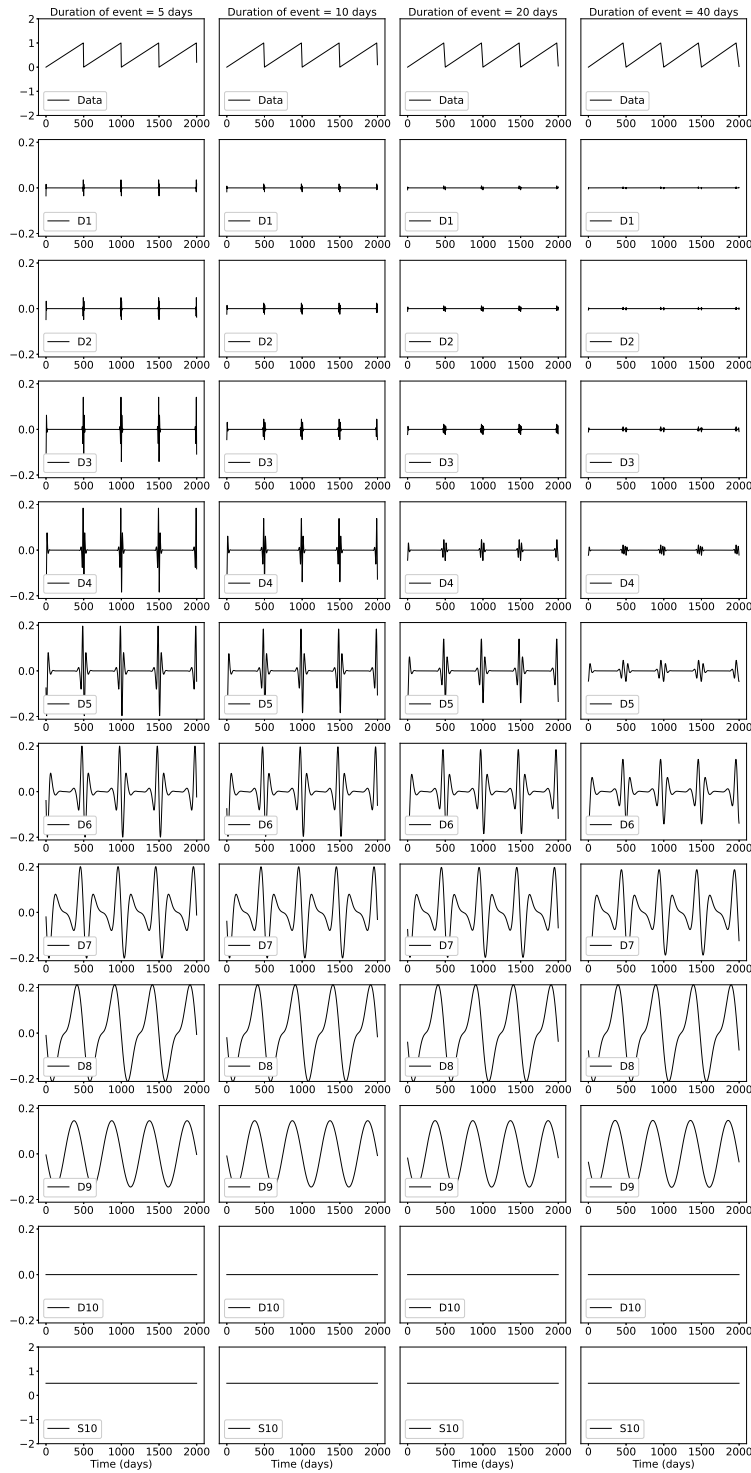


FIGURE 4.1: Demonstration of a wavelet decomposition for a synthetic dataset. A synthetic time series is created (top row) with steps of period 500 days, and transient durations of 5 days (left), 10 days, 20 days, and 40 days (right). The resulting details and smooths are shown in increasing level. The amplitude of the synthetic time series is normalized to 1, and the details and smooths show the relative amplitude.

that lasts about one week at an individual GPS station, and the whole event lasts several weeks. We expect them to start being visible at the level 5 of the wavelet decomposition, but to not be noticeable at lower time scales.

4.3.3 MODWT of GPS and tremor data

The DWT and MODWT methods must be used on a continuous time series, without gaps in the recordings. To deal with the gaps in the GNSS recordings, we simply replace the missing values by interpolation. The value for the first day for which data are missing is equal to the mean of the five days before the gap. The value for the last day for which data are missing is equal to the mean of the five days after the gap. The remaining missing values are computed by doing a linear interpolation of the first and the last values and adding a Gaussian noise component with mean zero and standard deviation equal to the standard deviation of the whole time series. The straight line starts at and ends at . We verify how the wavelet details may be affected by looking at a GPS time series without missing values and compared the wavelet details with and without removing some data points. Station PGC5 recorded continuous 1390 days between 2009 and 2013 without any missing values. We first computed the wavelet details without missing values. Then, we removed ten neighboring values, replaced them using the method described above (linear interpolation plus Gaussian noise), and computed the wavelet details with the replaced values. Figure 4.2 shows a comparison of the two wavelet details for two different locations of the missing values. We can see that there are visible differences in the time series itself, and in the details at the smallest levels of the wavelet decomposition. However, the differences between the wavelet details with and without missing values get smaller and smaller with increasing levels of details, and are barely visible for the levels that are most relevant (levels 6 and above). We thus conclude that we can easily replace the missing values in the GNSS time series without introducing false detections of slow-slip events.

We then applied the wavelet filtering to real GPS data. Figure 4.3 shows the longitudinal displacement for GPS station PGC5, located in southern Vancouver Island, the details of the wavelet decomposition for levels 1 to 8, and the smooth. In the data, we can see a sharp drop in displacement whenever there is a documented slow-slip event. For levels 5 to 8, which correspond to time scales 16, 32, 64 and 128 days, we can see in the details a positive peak followed by a negative peak whenever there is a drop in displacement in the data. We thus verify that the wavelet method can detect steps in the time series associated with slow-slip events.

To increase the signal-to-noise ratio and better detect slow-slip events, we stack the signal from several neighboring GPS stations. We choose to focus on GPS stations located close enough to the tremor zone to get a sufficiently high amplitude of the slow-slip signal. We choose 16 points along the 40 km depth contour of the plate boundary (model from Preston et al. (2003)) with spacing equal 0.1 degree in latitude (red triangles on Figure 4.4). Then we took all the GPS stations located in a 50 km radius for a given point, compute the wavelet details for the longitudinal displacement of each station, and stack each detail over the GPS stations. We thus have a stacked detail for each level 1 to 10 of the wavelet decomposition.

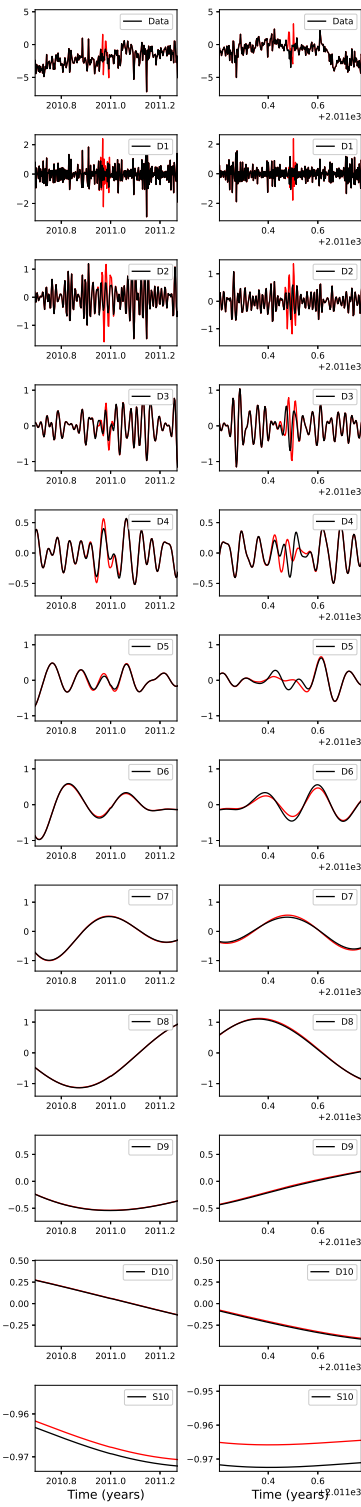


FIGURE 4.2: Top: Data from GPS station PGC5 without missing values (black) and with missing values replaced by the sum of a straight line and a Gaussian noise component (red) for two locations of the missing values (left and right). The corresponding ten details and smooths of the wavelet composition are shown in increasing levels for the original data (black) and for the missing values replaced by linear interpolation plus Gaussian noise (red).

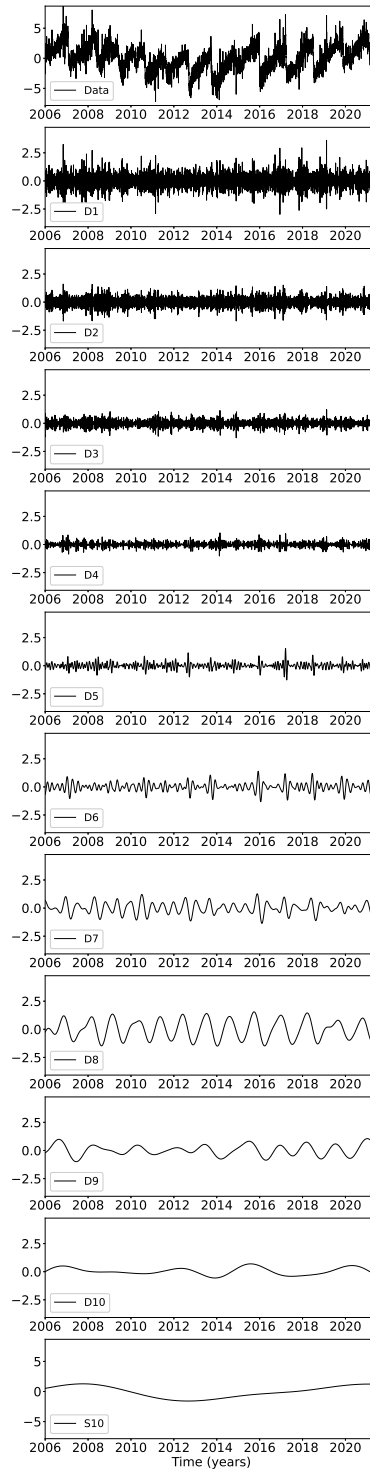


FIGURE 4.3: Top: Longitudinal displacement recorded at GPS station PGC5. The resulting details and smooth of the wavelet decomposition are shown in increasing level.

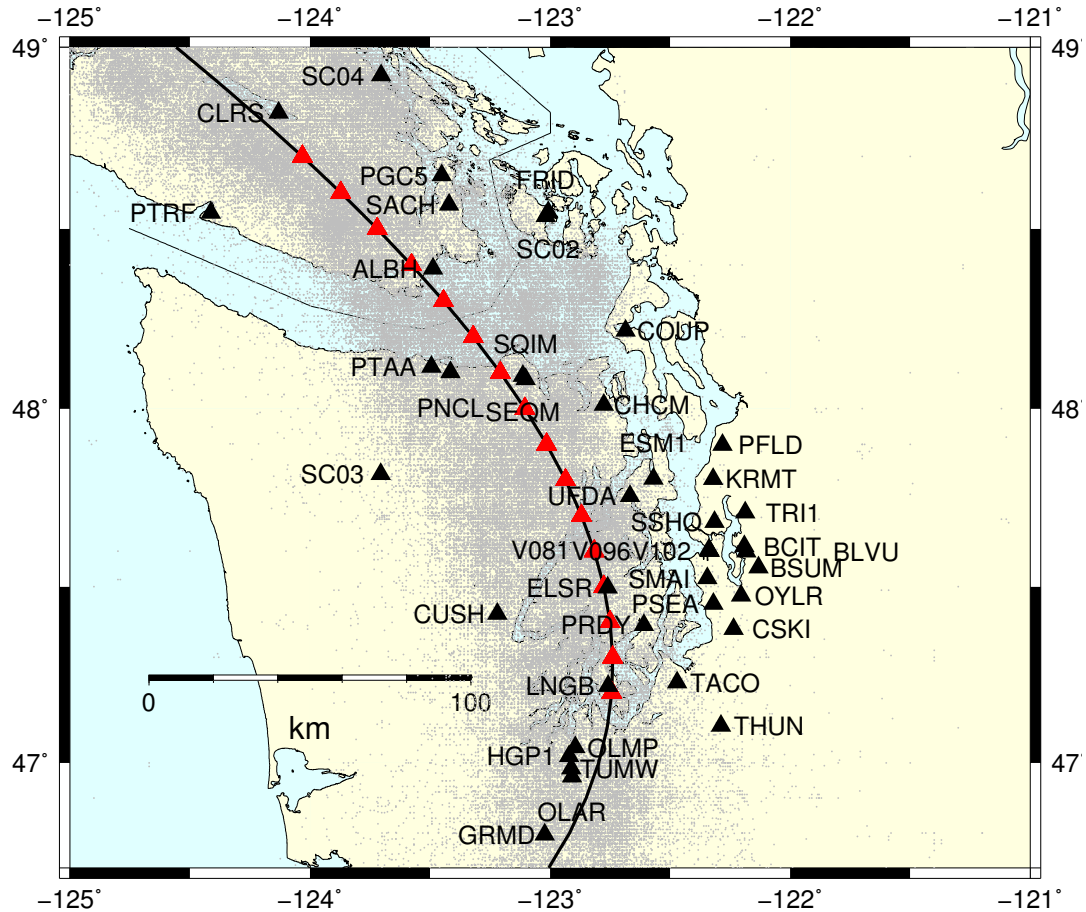


FIGURE 4.4: GPS stations used in this study (black triangles). The black line represents the 40 km depth contour of the plate boundary model by Preston et al. (2003). The red triangles are the locations where we stack the GPS data. The small grey dots are all the tremor locations from the PNSN catalog.

To assess the success of the wavelet decomposition for detecting slow-slip events in GPS time series, we validate the approach by comparing to an independent proxy for ETS events. We took all the tremor epicenters located within a 50 km radius centered on one of the 16 locations marked by red triangles on Figure 4.4. Then we computed the cumulative number of tremor within this circle. Finally, we removed a linear trend from the cumulative tremor count, and applied the wavelet transform. Figure 4.5 shows an example of the wavelet decomposition for the third northernmost location on Figure 4.4 (which is closest to GPS station PGC5). Contrary to what happens for the GPS data, we see a sharp increase in the time series whenever there is a tremor episode, which translates into a negative peak followed by a positive peak in the wavelet details.

4.4 Results

We stacked the 8th level detail of the wavelet decomposition of the displacement over all the GPS stations located in a 50 km radius of a given point, for the 16 locations indicated in Figure 4.3. The result is shown in the top panel of Figure 4.6, where each line represents one of the locations along strike. To better highlight the peaks in the wavelet details, we highlighted in red the time intervals where the amplitude of the stacked detail is higher than a threshold, and in blue the time intervals where the amplitude of the stacked detail is lower than minus the threshold. To compare the GPS signal with the tremor signal, we plotted the 8th level detail of the wavelet decomposition of the tremor count on the bottom panel of Figure 4.6. We multiplied by -1 the cumulative tremor count for the wavelet decomposition in order to be able to match positive peaks with positive peaks and negative peaks with negative peaks. In the tremor catalog from the PNSN, there are 17 tremor events with more than 150 hours of tremor recorded. The events are summarized in Table 4.1. The time of the event is the start date plus half the duration of the event.

Although the latitudinal extension of the events is not always the same for the GPS data and for the tremor data, we identify the same 13 events in both 8th wavelet decompositions for the 8th level: January 2007, May 2008, May 2009, August 2010, August 2011, September 2012, September 2013, August-November 2014, January 2016, March 2017, June 2018, March-November 2019, and October 2020-January 2021. Although there are two events in the tremor catalog in August 2014 and November 2014, these two events are not distinguishable in the 8th level details and look more like a single event slowly propagating from South to North. The same phenomenon is observed in 2019 when two tremor events in March and November 2019 are merged into a single event propagating slowly from South to North. In 2020-2021, the wavelet decomposition of the tremor shows one event in the south in October-November 2020 and one event in the North in January 2021, but in the wavelet decomposition of the GPS data, these three events look like a single event propagating slowly from South to North.

A similar comparison is shown for the wavelet decomposition of the GPS data and the wavelet decomposition of the tremor count data for the 7th level and the 6th level respectively (Figures 4.7 and 4.8). The events are harder to see in the 7th level than in the 8th level, both for the GPS data and the tremor count data. The wavelet decomposition is more noisy for the GPS data between 2010 and 2012, but it does

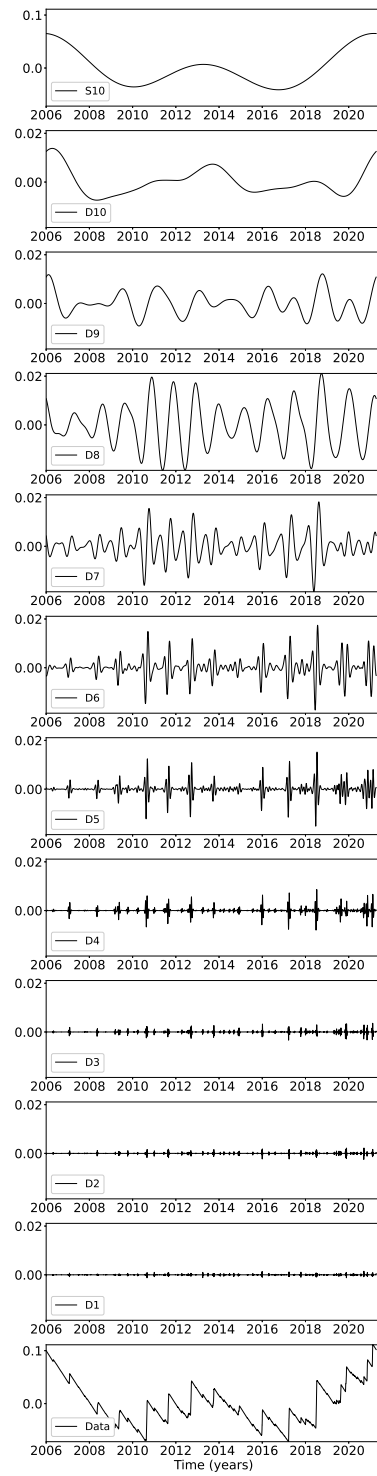


FIGURE 4.5: Details and smooth of the wavelet decomposition of the detrended cumulative tremor count around the third northernmost red triangles on Figure 4.3 (latitude 48.5).

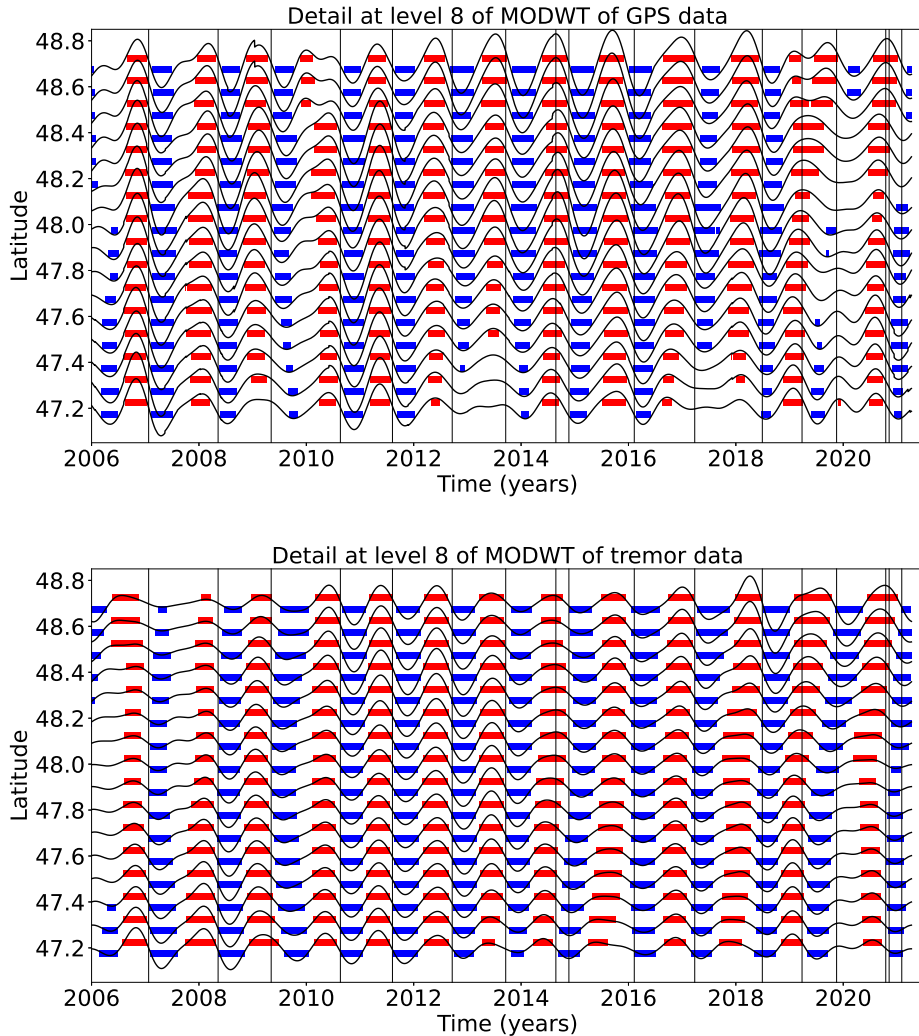


FIGURE 4.6: Top: Stacked 8th level details of the wavelet decomposition of the displacement over all the GPS stations located in a 50 km radius of a given point, for the 16 red triangles indicated in Figure 4.4. Bottom: 8th level detail multiplied by -1 of the cumulative tremor count in a 50 km radius of a given point for the same 16 locations. The black lines represent the timings of the ETS events from Table 4.1. We mark by a red rectangle every time where the amplitude is higher than a threshold of 0.4 (for the GPS) or 0.003 (for the tremor). We mark by a blue rectangle every time where the amplitude is lower than minus the threshold.

TABLE 4.1: Episodic Tremor and Slip events with $M > 6$ identified by MODWT in both the GPS and the tremor data. The duration and the number of tremor are from the tremor catalog of the PNSN. The event number and the magnitude are from the slow-slip catalog of Michel, Gualandi, and Avouac (2019).

Time	Duration (days)	Number of tremor (hours)	Event number	Magnitude
2007.06	28	398	3	6.68
2008.36	25	402	10	6.56
2009.35	24	248	16	6.49
2010.63	29	518	24	6.54
2011.60	37	479	30	6.47
2012.72	37	620	34	6.54
2013.71	27	423	41	6.58
2014.65	15	190	48	6.03
2014.89	38	385	51	6.40
2016.11	43	421	54	6.79
2017.23	19	279	59	6.61
2018.49	22	381		
2019.23	34	195		
2019.88	16	205		
2020.79	26	193		
2020.86	12	162		
2021.09	14	230		

not seem that there are more slow-slip events visible in the 7th level.

For the 6th level detail, we see an additional event in the South in Fall 2009 that is present both in the GPS and the tremor data. It may correspond to the northern extent of a big ETS event occurring in Fall 2009 south of the study area (event 19 in the Michel, Gualandi, and Avouac (2019) catalog). There are three small signals in the GPS data in Winter 2012, Fall 2017, and Winter 2020 that are not present in the tremor data, and may be false detections. To summarize, we assume that true detections are events present in both GPS and tremor time series, and false detections are events present in the GPS but not in the tremor time series. Then, all the 13 events present on the 8th level detail of the wavelet decomposition are true detections and 14 of the 17 events present on the 6th level detail of the wavelet decomposition are true detections.

4.5 Discussion

To better evaluate the number of true and false detections, we convert the wavelet details into binary time series. If the absolute value of the wavelet detail is higher than a threshold, we replace the value by 1 (for positive values) or -1 (for negative values), otherwise we replace the value by 0. We do this on both the wavelet details of the GPS data and of the tremor data. Then we decide that if both the GPS and the tremor time series take the value 1 (or both take the value -1), we have a true detection (true positive, TP). If the GPS and the tremor time series have opposite signs, or if the absolute value of the GPS time series is 1 but the value of the tremor time series is 0, we have a false detection (false positive, FP). If both time series take

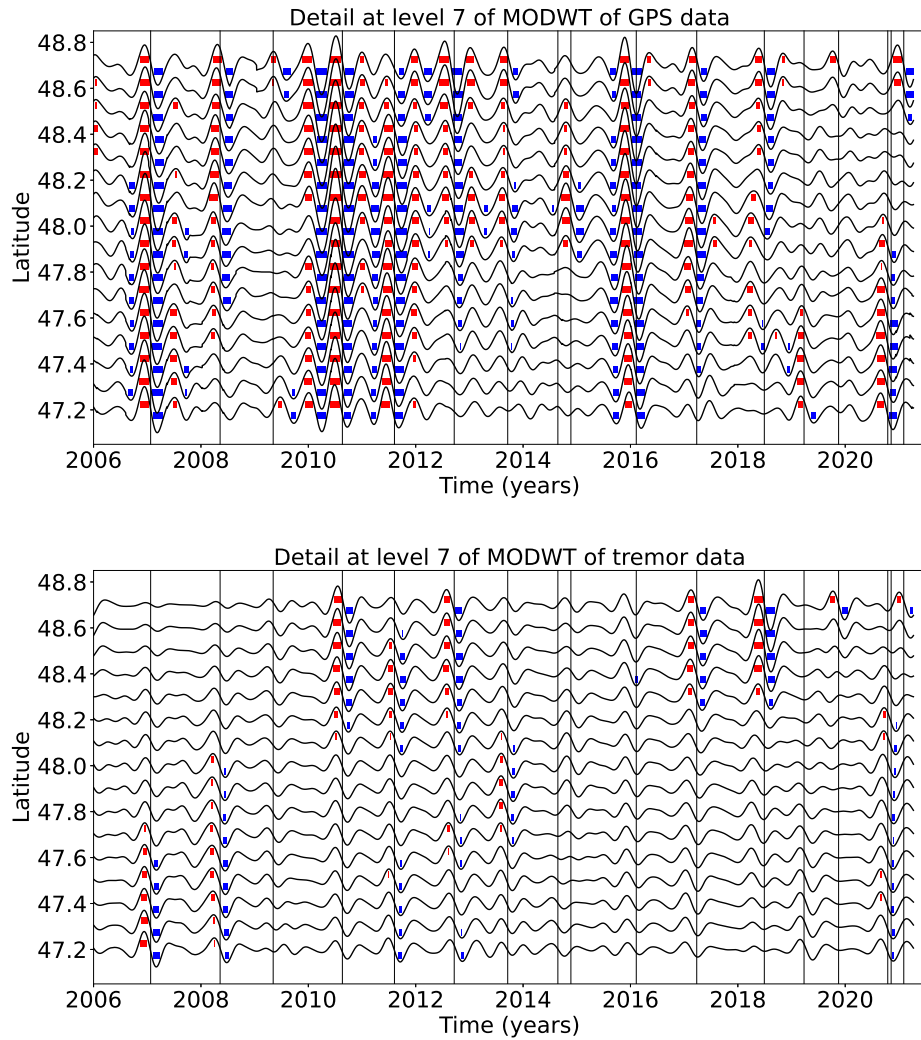


FIGURE 4.7: Same as Figure 4.6 but for the 7th level detail. The thresholds are 0.5 (for the GPS) and 0.01 (for the tremor).

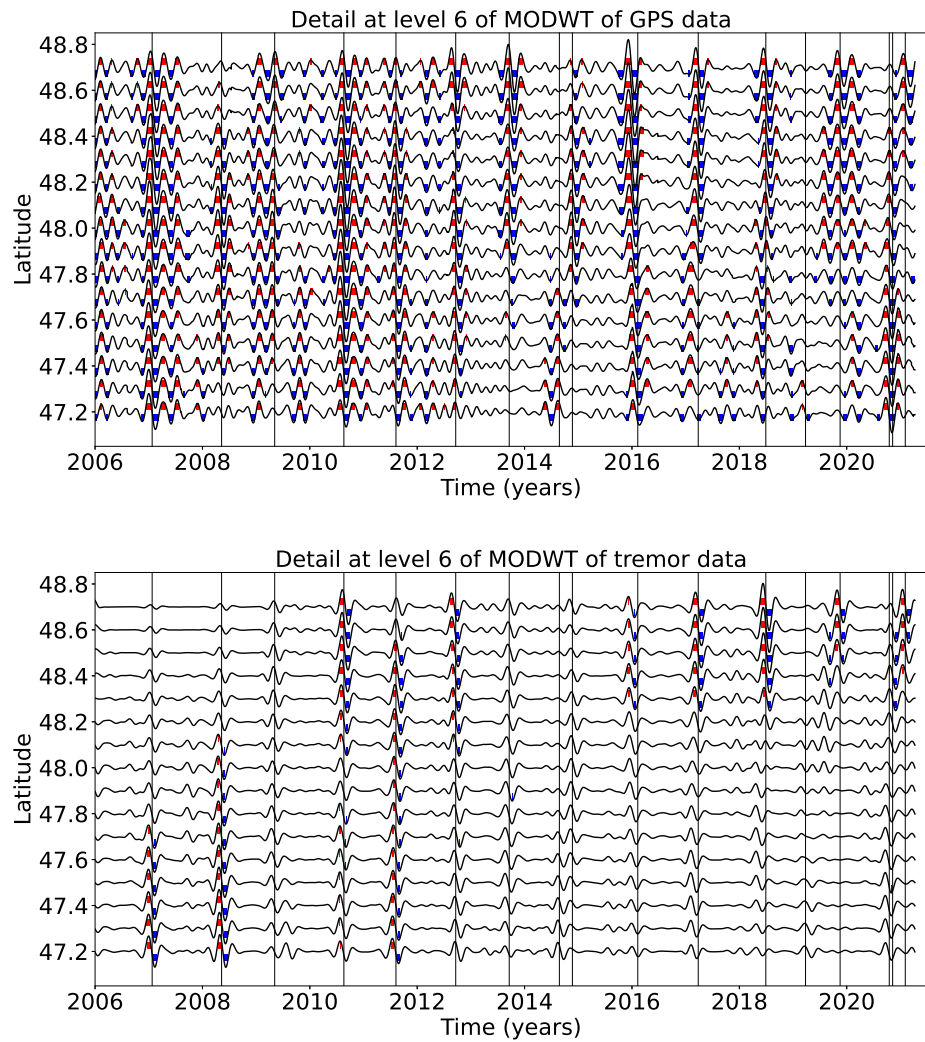


FIGURE 4.8: Same as Figure 4.6 but for the 6th level detail. The thresholds are 0.3 (for the GPS) and 0.009 (for the tremor).

the value 0, we do not have detection (true negative, TN). If the GPS time series take the value 0, but the absolute value of the tremor time series is 1, we miss a detection (false negative, FN). We then define the sensitivity (true positive rate) and the specificity (equal to 1 minus the false positive rate) as:

$$\begin{aligned} \text{sensitivity} &= \frac{TP}{TP + FN} \\ \text{specificity} &= \frac{TN}{TN + FP} \end{aligned} \quad (4.3)$$

We can then evaluate the quality of the detections obtained with our method by plotting a receiver operating characteristic curve (ROC curve). The ROC curve is widely used for binary classification problems in statistics and machine learning. We calculate an ROC value by varying the values of the threshold (here the two thresholds used to convert the GPS and the tremor time series into binary time series), computing the corresponding values of the true positive rate and the false positive rate (equal to 1 minus the specificity), and plotting the true positive rate as a function of the false positive rate. If the classification was made randomly, all the points would fall on the first diagonal. If the classifier was perfect, the corresponding point would fall on the top left corner of the graph with true positive rate equal to 1 and false positive rate equal to 0. The bigger the area under the curve, the better the classification method is.

As the slow-slip events are better seen on levels 6, 7 and 8 of the wavelet decomposition, we first add the wavelet details corresponding to levels 6 to 8, and transform the resulting time series into a binary time series. We apply this transform to both the GPS and the tremor time series with varying thresholds. We then plot the ROC curve on Figure 4.9, each dot representing a different threshold. The corresponding sums of the wavelet details for the GPS data and the tremor data are shown on Figure 4.10. We can see that there is a trade-off between sensitivity and specificity as we vary the threshold. If we decrease the false positive rate, we also decrease the number of true events detected. If we increase the number of true events detected, we also increase the false positive rate. In Figure 4.10, we have chosen thresholds for the GPS time series and the tremor time series such that the specificity is higher than 0.75, and the sensitivity is the highest possible, that is we have chosen the thresholds corresponding to the dot that is farthest from the diagonal, which is random.

In addition to the magnitude 6 events discussed above, Michel, Gualandi, and Avouac (2019) have also identified several magnitude 5 events using a variational Bayesian Independent Component Analysis (vbICA) decomposition of the signal. As we expect smaller magnitude events to be more visible at smaller time scales of the wavelet decomposition (level 5), we verify for all these events whether a signal can be seen at the same time as the time given in their catalog. Most of these magnitude 5 events are also sub-events of bigger magnitude 6 events. Table 4.2 summarizes for each event its timing, its number and its magnitude as indicated in the catalog from Michel, Gualandi, and Avouac (2019), and whether it is part of a bigger magnitude 6 event. Figure 4.11 shows the 5th level detail wavelet decomposition of the GPS data. Red lines show the timing of the big ETS events from Table 4.1, and blue lines show the timing of the small slow-slip events from Table 4.2.

All 14 events that are sub-events of a bigger event are visible at level 5. However, this may be because the bigger events are clearly seen at levels 6 to 8, and also at

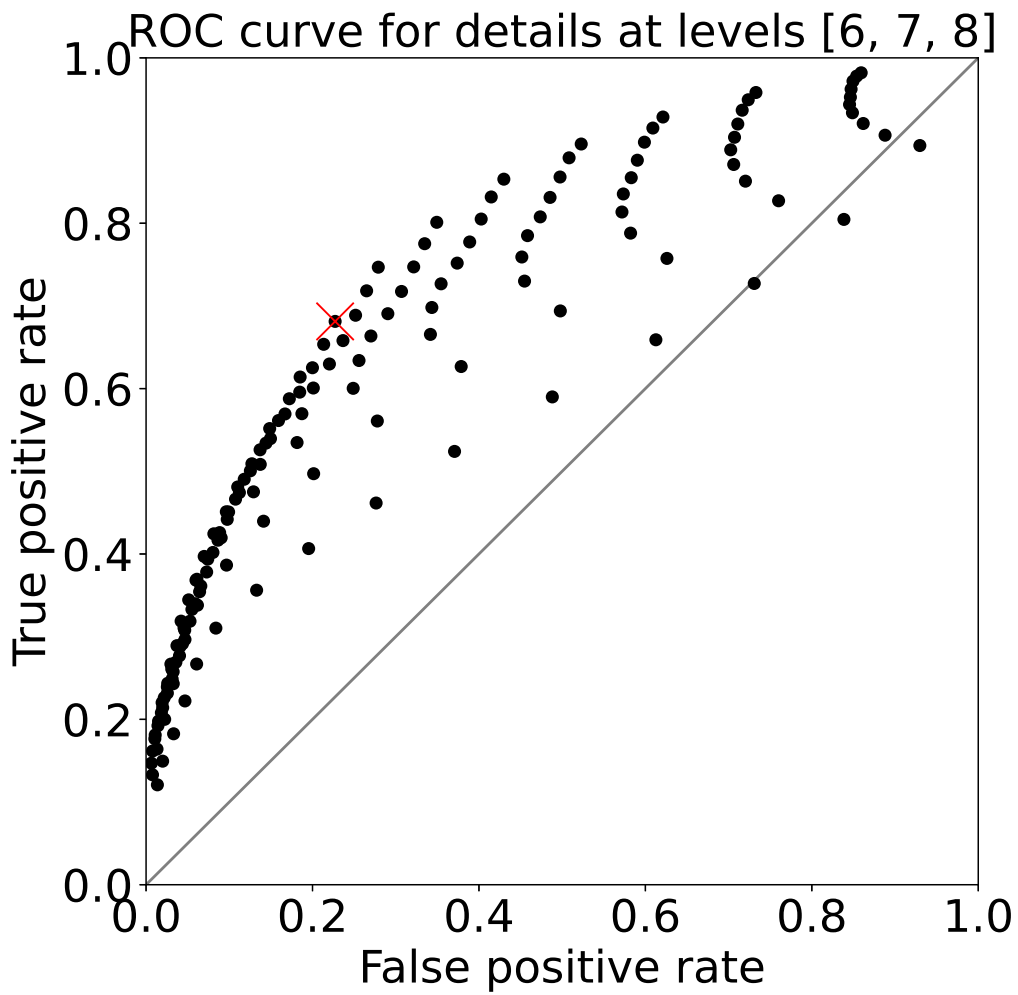


FIGURE 4.9: ROC curve for the sum of the 6th, 7th, and 8th level details of the wavelet decomposition. Each black dot represents the true positive rate of event detections and the false positive rate of event detections for a given pair of thresholds (for the GPS and for the tremor). The red cross marks the true positive rate and the false positive rate obtained with the thresholds used to make Figure 4.10.

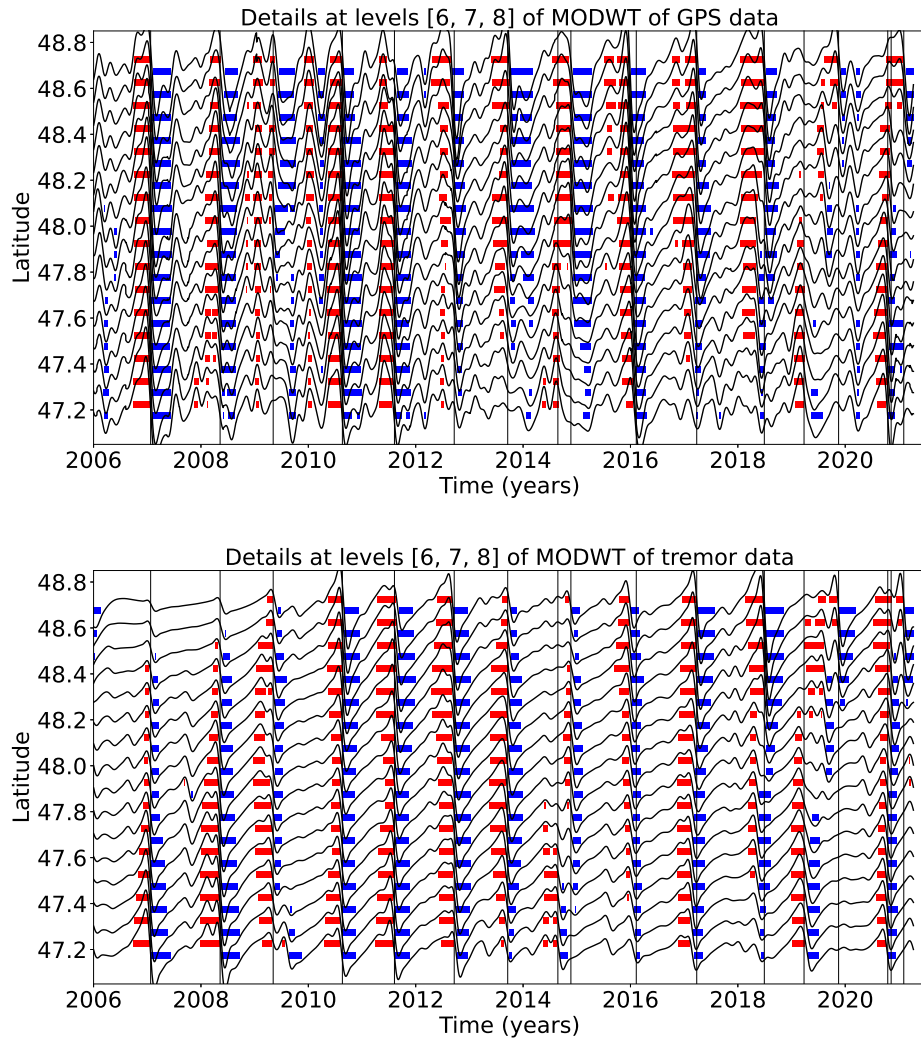


FIGURE 4.10: Same as Figure 4.6 but for the sum of the 6th, 7th and 8th level details. The thresholds are 0.8 (for the GPS) and 0.01 (for the tremor).

TABLE 4.2: Magnitude 5 events from Michel, Gualandi, and Avouac (2019).

Time	Event number	Magnitude	Sub-event of bigger event
2007.06	1	5.64	Yes
2007.08	2	5.91	Yes
2008.38	11	5.50	Yes
2009.16	14	5.50	No
2009.36	17	5.32	Yes
2010.63	25	5.76	Yes
2011.66	31	5.61	Yes
2011.66	32	5.32	Yes
2012.69	35	5.56	Yes
2013.74	42	5.71	Yes
2014.69	49	5.31	Yes
2014.93	52	5.39	Yes
2016.03	57	5.80	Yes
2017.13	60	5.43	Yes
2017.22	61	5.37	Yes

smaller time scales. The one small event that is not part of a bigger event (Winter 2009) is visible at level 5 of the wavelet decomposition. However, some other events that are not in the catalog of Michel, Gualandi, and Avouac (2019)'s catalog are also visible in late 2007, early 2010, early 2012, and late 2016. Therefore, it is difficult to differentiate between a true detection and a false detection, and to conclude whether the method can indeed detect events of magnitude 5.

In Figure 4.10, we see four smaller events that are not in the catalog of Michel, Gualandi, and Avouac (2019): at about 2007.5, there is a negative peak followed by a positive peak (that is an event in the opposite direction of what would be expected from slow-slip), at about 2010.2, 2012.2 and 2020.2, there are positive peaks followed by negative peaks for all the sixteen locations studied in this paper. Looking back at the original GPS data, there is a small increase in the displacement in the eastern direction that lasts about one or two months at about 2007.5. However, the direction of the displacement does not correspond to a slow-slip event, and another cause should be found to explain this signal. There is a decrease in displacement that lasts several months at about 2010.2. This transient may correspond to a long duration slow-slip event. There is a small decrease in displacement at about 2012.2. Its amplitude is small but the duration and direction correspond to a slow-slip event, so this transient could be a very small slow-slip event. Finally, there is also a small decrease in displacement at about 2020.2 that is difficult to interpret.

4.6 Conclusion

In this paper, we develop and test a new approach for detecting transient events in GNSS time series, such as slow-slip events. We used wavelet methods to analyze GNSS time series and tremor recordings of slow-slip events in Cascadia. We used detrended GNSS data, applied the MODWT transform, and stacked the wavelet details over several nearby GNSS stations. As an independent check on the timing of slow-slip events, we also computed the cumulative number of tremor in the vicinity

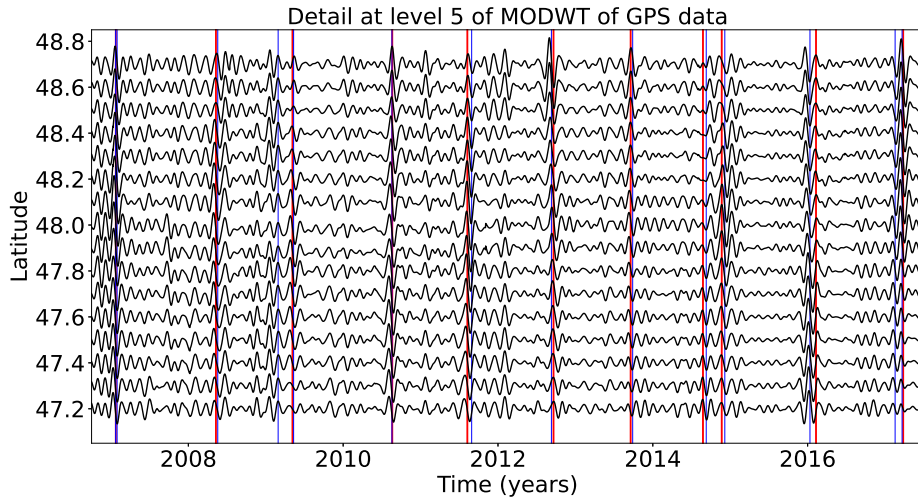


FIGURE 4.11: Stacked 5th level details of the wavelet decomposition of the displacement over all the GPS stations located in a 50 km radius of a given point, for the 16 red triangles indicated in Figure 4.4. The red lines represent the timings of the ETS events from Table 4.1. The blue lines represent the timings of the magnitude 5 events from the catalog of Michel, Gualandi, and Avouac (2019).

of the GNSS stations, detrended this signal, and applied the MODWT transform. In both time series, we could then see simultaneous waveforms whose timing corresponds to the timing of slow-slip events. We assumed that there is a slow-slip event whenever the wavelet signal gets above a threshold. We verified that there is a good correlation between slow-slip events detected with only GNSS data, and slow-slip events detected with only tremor data. The wavelet-based detection method detects all the events of magnitude higher than 6 as determined by independent event catalogs (e.g. Michel, Gualandi, and Avouac (2019)). We detected signals in the GPS data that could be magnitude 5 events, but it is not easy to differentiate between true detections and false detections.

Chapter 5

Perspectives

In the second chapter of this thesis, a method to estimate the depth of the source of the tectonic tremor, and the depth extent of the region from which the tremor originates, was developed using S minus P times determined from lag times of stacked cross-correlations of horizontal and vertical components of seismic recordings from small aperture arrays in the Olympic Peninsula, Washington. The source of the tremor was located close to the plate boundary in a region no more than two to three kilometers thick. The source of the tremor is thus distributed over a slightly wider depth range than the low-frequency earthquakes. However, due to the depth uncertainty, it is difficult to conclude whether the tremor is located near the top of the subducting oceanic crust, in the lower continental crust just above the plate boundary, in a layer distributed above and below the plate boundary, or confined to a very narrow plate boundary. The location of the tremor relative to the low-velocity layer also observed near the plate boundary remains uncertain. Tremor and low-frequency earthquake depths are consistent with filling a volume in the upper subducted crust that is characterized by high fluid pressure and very low S-wave velocities described as the preferred model by Bostock (2013). Secondary peaks in the cross-correlation functions were sometimes identified at smaller time lags (two to four seconds) and could correspond to the time lag between a directed wave and a reflected wave, but no signal was systematically observed for all the source-array locations. Thus, it is not clear whether a secondary wave arrival is actually observed or whether this is just an artifact due to the low signal-to-noise ratio. To improve the signal processing method, it would be interesting to use methods that have already been applied to the analysis of recordings of volcanic tremor, like the Maximal Overlap Discrete Wavelet Packet Transform (MODWPT) (Jones, Carniel, and Malone, 2012) or Independent Component Analysis (ICA) (De Lauro et al., 2016).

In the third chapter of this thesis, templates obtained by Plourde et al. (2015) using data recorded by the EarthScope Flexible Array Mendocino Experiment (FAME) network in Northern California during an episode of high tremor activity in April 2008, were used to extend their catalog to the whole two years (2007-2009) during which the seismic stations were installed. The two-year-long catalog was then used to create templates for stations from the permanent seismic networks, and the seismic data recorded by these stations was used to extend the catalog before and after the FAME experiment. Low-frequency earthquakes were observed every time that there is tectonic tremor on the tremor catalog from Boyarko et al. (2015), and several additional smaller low-frequency earthquake episodes were also observed. Whereas the low-frequency earthquake families from the subduction zone are mainly active during the big Episodic Tremor and Slip events, the southernmost family is more active, with repeating events about once a month. Downdip families

are also more active than up dip families. Tidal stress changes seem to be correlated with low-frequency earthquake activity in the later part of the 2008 Episodic Tremor and Slip event. A thorough analysis of the relation between tidal forcing and low-frequency earthquakes is warranted as the predicted tidal stresses are far smaller than in northern Cascadia, but tidal stress still appears to have a strong influence on low-frequency earthquake activity. As more stations were added to the permanent networks, new templates can be computed and the catalog could be extended iteratively until present. If the catalog is extended to the present, a direct comparison with the revised PNSN catalog (2017 to present) would be especially interesting because, in the revised catalog, tremor are more active in southern Cascadia than in central or northern Cascadia. The same procedure that I used in southern Cascadia could also be applied in regions where low-frequency earthquake templates have been established with a temporary network, for instance in the Olympic peninsula (Chestler and Creager, 2017a; Chestler and Creager, 2017b). Now that a longer low-frequency earthquake catalog has been established, statistical analyses of low-frequency earthquake occurrence times could be carried out. The statistical characterization of low-frequency earthquake occurrence could provide important constraints on future mechanical models of slow earthquake phenomena.

In the fourth chapter of this thesis, a new approach for detecting transient events in Global Navigation Satellite System (GNSS) time series, such as slow-slip events, was developed and tested. Wavelet methods were used to analyze GNSS time series and tremor recordings of slow-slip events in Cascadia. GNSS data were detrended, transformed using the Maximal Overlap Discrete Wavelet (MODWT) transform, and the wavelet details were stacked over several nearby GNSS stations. As an independent check on the timing of slow-slip events, the cumulative number of tremor in the vicinity of the GNSS stations was computed, this signal was detrended, and the MODWT transform was applied. In both time series, simultaneous waveforms whose timing corresponds to the timing of slow-slip events could be seen. It is assumed that there is a slow-slip event whenever the wavelet signal gets above a threshold. There was a good correlation between slow-slip events detected with only GNSS data, and slow-slip events detected with only tremor data. The wavelet-based detection method detected all events of magnitude higher than 6 as determined by independent event catalogs (e.g. (Michel, Gualandi, and Avouac, 2019)). Signals in the GNSS data that could be magnitude 5 events were also detected, but it is not easy to differentiate between true detections and false detections. The wavelet detector could now be applied in regions where tremor and slow-slip occurrence are not well spatially and temporally correlated, tremor is not abundant, or the seismic network is not robust enough, and we must rely on the GNSS data to detect possible slow-slip events. The method could also be extended by applying wavelet-based denoising methods to the GNSS data, or using more advanced wavelet methods such as the wavelet scattering transform.

Appendix A

Supplement for Chapter 2

TABLE A.1: Depths, thicknesses and S-to-P time lags

Latitude grid	Longitude grid	Depth	Thickness	S-to-P time lag	Latitude array	Longitude array
48.00568	-123.42002	31.54815	1.65708	5.61941	48.00568	-123.08435
48.05060	-123.42002	33.39968	4.14569	5.83762	48.00568	-123.08435
47.96077	-123.35288	33.60503	2.62958	5.41716	48.00568	-123.08435
48.00568	-123.35288	35.01803	0.50788	5.57185	48.00568	-123.08435
48.05060	-123.35288	35.71534	0.82604	5.64570	48.00568	-123.08435
48.09551	-123.35288	35.39573	0.86434	5.58676	48.00568	-123.08435
47.87093	-123.28575	34.96605	1.92117	5.53694	48.00568	-123.08435
47.91585	-123.28575	32.62490	2.44170	5.21036	48.00568	-123.08435
47.96077	-123.28575	36.59168	1.37536	5.48916	48.00568	-123.08435
48.00568	-123.28575	35.89275	0.91314	5.37334	48.00568	-123.08435
48.05060	-123.28575	36.78619	0.91691	5.50867	48.00568	-123.08435
48.09551	-123.28575	35.53476	0.50862	5.51101	48.00568	-123.08435
47.87093	-123.21862	31.67542	1.92960	5.11195	48.00568	-123.08435
47.96077	-123.21862	34.93296	1.77697	5.09618	48.00568	-123.08435
48.00568	-123.21862	34.22632	0.49926	4.96042	48.00568	-123.08435
48.05060	-123.21862	36.91445	0.91123	5.31363	48.00568	-123.08435
48.09551	-123.21862	35.68358	1.01354	5.31189	48.00568	-123.08435
47.87093	-123.15149	33.98015	2.03779	5.20434	48.00568	-123.08435
47.91585	-123.15149	36.14101	1.37292	5.22875	48.00568	-123.08435
47.96077	-123.15149	36.46074	1.50402	5.10543	48.00568	-123.08435
47.91585	-123.08435	36.49842	2.17686	5.21478	48.00568	-123.08435
47.96077	-123.08435	35.58549	1.80173	4.98303	48.00568	-123.08435
47.87093	-123.01722	35.26231	2.29227	5.34418	48.00568	-123.08435
47.91585	-123.01722	34.62103	1.36685	5.06163	48.00568	-123.08435
47.96077	-123.01722	35.68984	2.22221	5.01622	48.00568	-123.08435
47.87093	-122.95009	33.98689	2.33013	5.35153	48.00568	-123.08435
47.91585	-122.95009	36.14334	0.93014	5.36226	48.00568	-123.08435
47.96077	-122.95009	38.23725	1.87431	5.45880	48.00568	-123.08435
47.82602	-122.81583	31.56048	2.61761	5.86262	48.00568	-123.08435
47.82253	-123.26401	35.74926	2.11541	5.68370	47.95728	-122.92866
47.86745	-123.26401	41.08041	2.87814	5.98238	47.95728	-122.92866
47.77762	-123.19694	34.56016	3.64623	5.52653	47.95728	-122.92866
47.82253	-123.19694	35.43658	2.03552	5.34851	47.95728	-122.92866
47.86745	-123.19694	39.94581	1.62455	5.58794	47.95728	-122.92866
47.91236	-123.19694	41.07722	1.71031	5.59555	47.95728	-122.92866
47.95728	-123.19694	42.49709	2.11620	5.68647	47.95728	-122.92866
48.00220	-123.19694	39.01816	1.71031	5.41247	47.95728	-122.92866
48.00220	-123.12987	40.86172	2.03982	5.33767	47.95728	-122.92866
47.77762	-123.06280	33.16434	2.14594	4.95932	47.95728	-122.92866
47.82253	-123.06280	34.74994	2.03436	4.85144	47.95728	-122.92866
47.95728	-123.06280	37.24059	1.35377	4.74856	47.95728	-122.92866
48.00220	-123.06280	38.05635	1.99664	4.88688	47.95728	-122.92866

Latitude grid	Longitude grid	Depth	Thickness	S-to-P time lag	Latitude array	Longitude array
47.91236	-122.99573	38.01949	0.44119	4.73018	47.95728	-122.92866
47.95728	-122.99573	38.77925	1.31783	4.79975	47.95728	-122.92866
48.00220	-122.99573	38.64337	1.76475	4.80089	47.95728	-122.92866
47.95728	-122.92866	38.35029	1.30400	4.70989	47.95728	-122.92866
48.00220	-122.92866	42.14840	1.51672	5.15039	47.95728	-122.92866
48.04711	-122.92866	42.26119	1.80503	5.26400	47.95728	-122.92866
48.05084	-123.31312	36.42203	1.44052	4.75103	48.00593	-123.31312
48.05084	-123.24599	36.42969	0.00000	4.77488	48.00593	-123.31312
48.09576	-123.24599	37.39737	1.90200	5.02892	48.00593	-123.31312
48.18559	-123.24599	47.25344	2.15282	6.17857	48.00593	-123.31312
48.23051	-123.24599	44.02860	1.42896	6.19100	48.00593	-123.31312
48.09576	-123.17885	35.08858	1.44200	4.94872	48.00593	-123.31312
48.14068	-123.17885	47.15230	3.02958	6.05049	48.00593	-123.31312
48.18559	-123.17885	42.57948	2.37736	5.95615	48.00593	-123.31312
48.02202	-122.91146	50.93325	1.36283	6.18599	47.93219	-123.04553
48.06693	-122.91146	49.24794	1.91613	6.19655	47.93219	-123.04553
48.05494	-123.53161	29.51566	0.93316	3.50649	48.05494	-123.46442
48.05494	-123.46442	33.80796	0.46297	4.05934	48.05494	-123.46442
47.97304	-123.33976	35.03636	0.00000	5.27955	47.97304	-123.13849
47.79337	-123.27267	31.40335	1.23311	5.23324	47.97304	-123.13849
47.83829	-123.27267	33.70694	1.21786	5.32252	47.97304	-123.13849
47.88320	-123.27267	35.90145	0.92566	5.33576	47.97304	-123.13849
47.92812	-123.27267	36.15617	0.00000	5.23042	47.97304	-123.13849
47.74846	-123.20558	22.82810	1.31211	5.19491	47.97304	-123.13849
47.79337	-123.20558	34.26325	3.64025	5.47604	47.97304	-123.13849
47.83829	-123.20558	34.71200	1.05090	5.28416	47.97304	-123.13849
47.88320	-123.20558	36.22529	0.45562	5.23800	47.97304	-123.13849
47.92812	-123.20558	38.98809	0.00000	5.38327	47.97304	-123.13849
47.88320	-123.13849	36.68302	0.88185	5.23505	47.97304	-123.13849
47.92812	-123.13849	36.54505	1.36479	5.09592	47.97304	-123.13849
47.92812	-123.07140	39.29662	0.41989	5.41719	47.97304	-123.13849
47.97304	-123.07140	39.87510	0.00000	5.46192	47.97304	-123.13849
47.88320	-123.00431	33.30555	2.26548	5.05178	47.97304	-123.13849
47.92812	-123.00431	38.03179	1.36685	5.43625	47.97304	-123.13849
47.92812	-122.93722	35.87715	2.91725	5.41123	47.97304	-123.13849

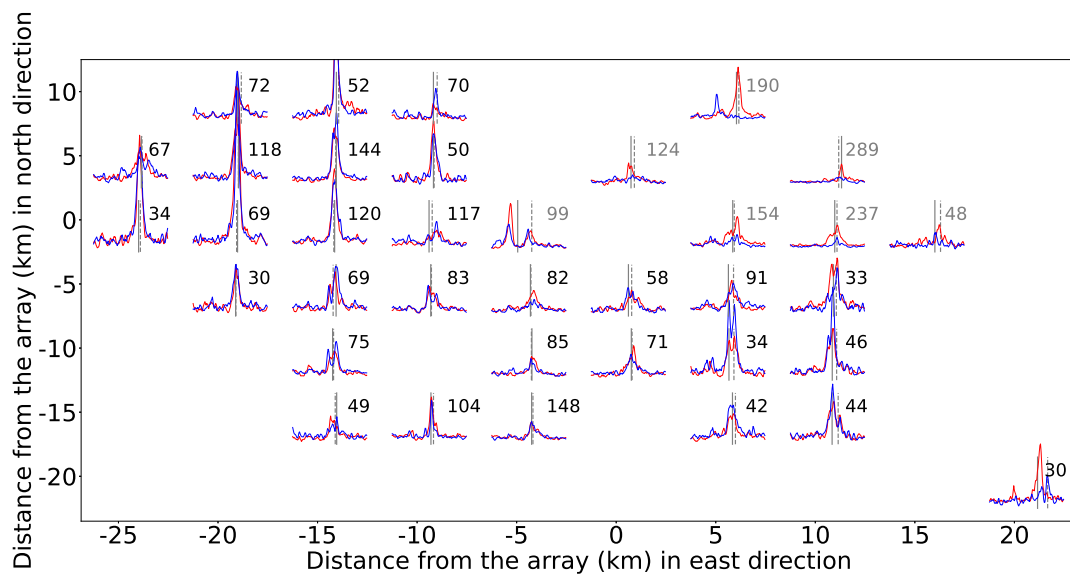


FIGURE A.1: Stacks of the envelopes of the cross correlation signals for different positions of the tremor source relative to the Burnt Hill array. See caption of Figure 2.4 from the main text for an explanation of this figure.

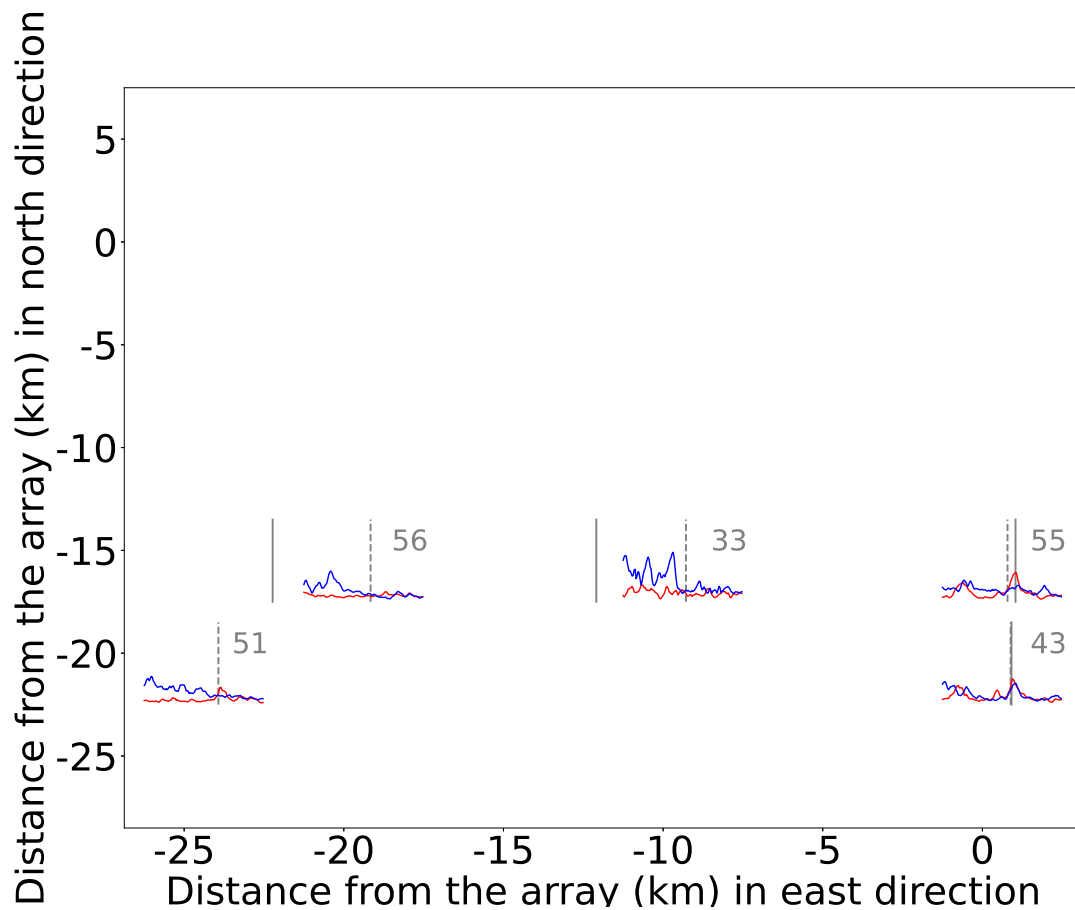


FIGURE A.2: Stacks of the envelopes of the cross correlation signals for different positions of the tremor source relative to the Cat Lake array. See caption of Figure 2.4 from the main text for an explanation of this figure.

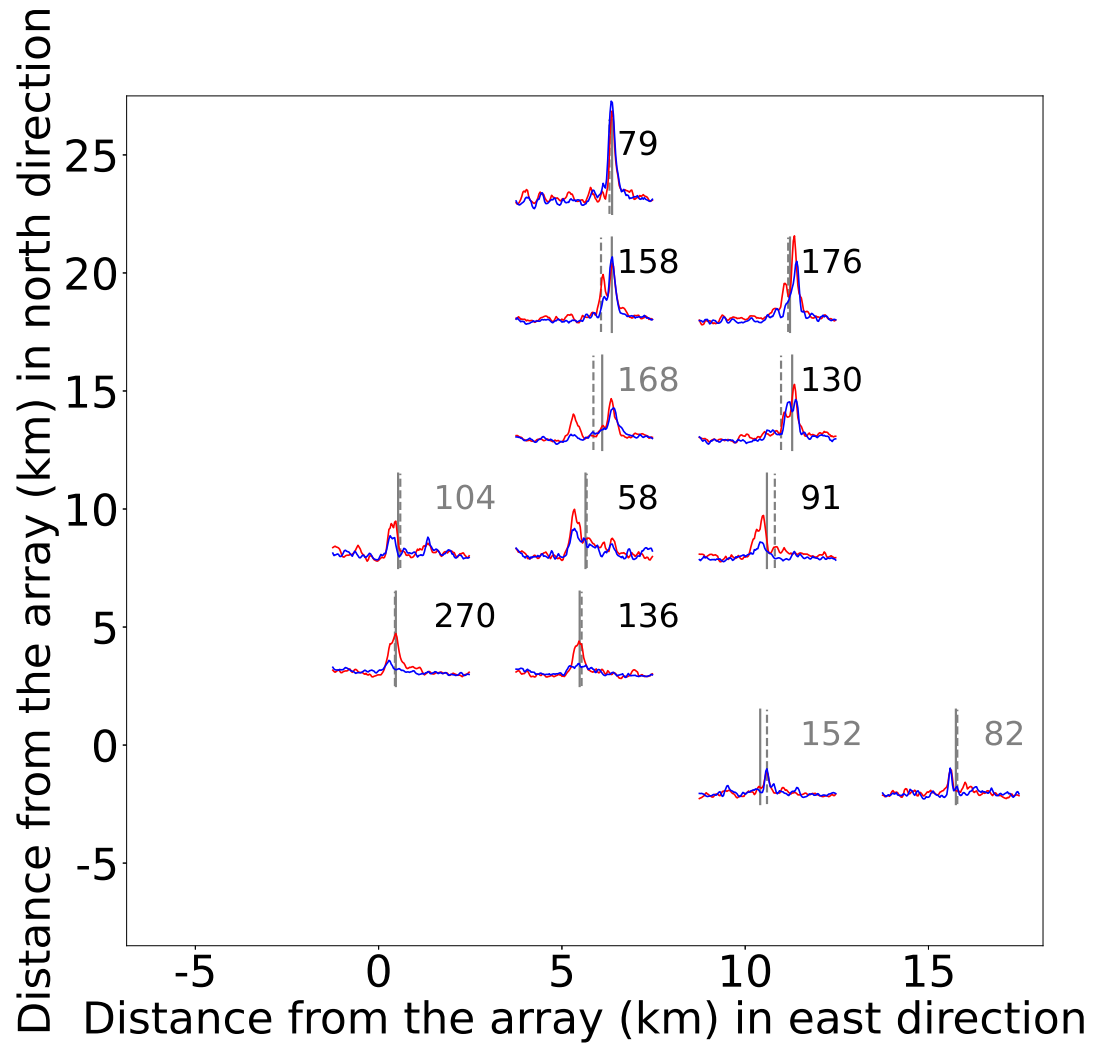


FIGURE A.3: Stacks of the envelopes of the cross correlation signals for different positions of the tremor source relative to the Danz Ranch array. See caption of Figure 2.4 from the main text for an explanation of this figure.

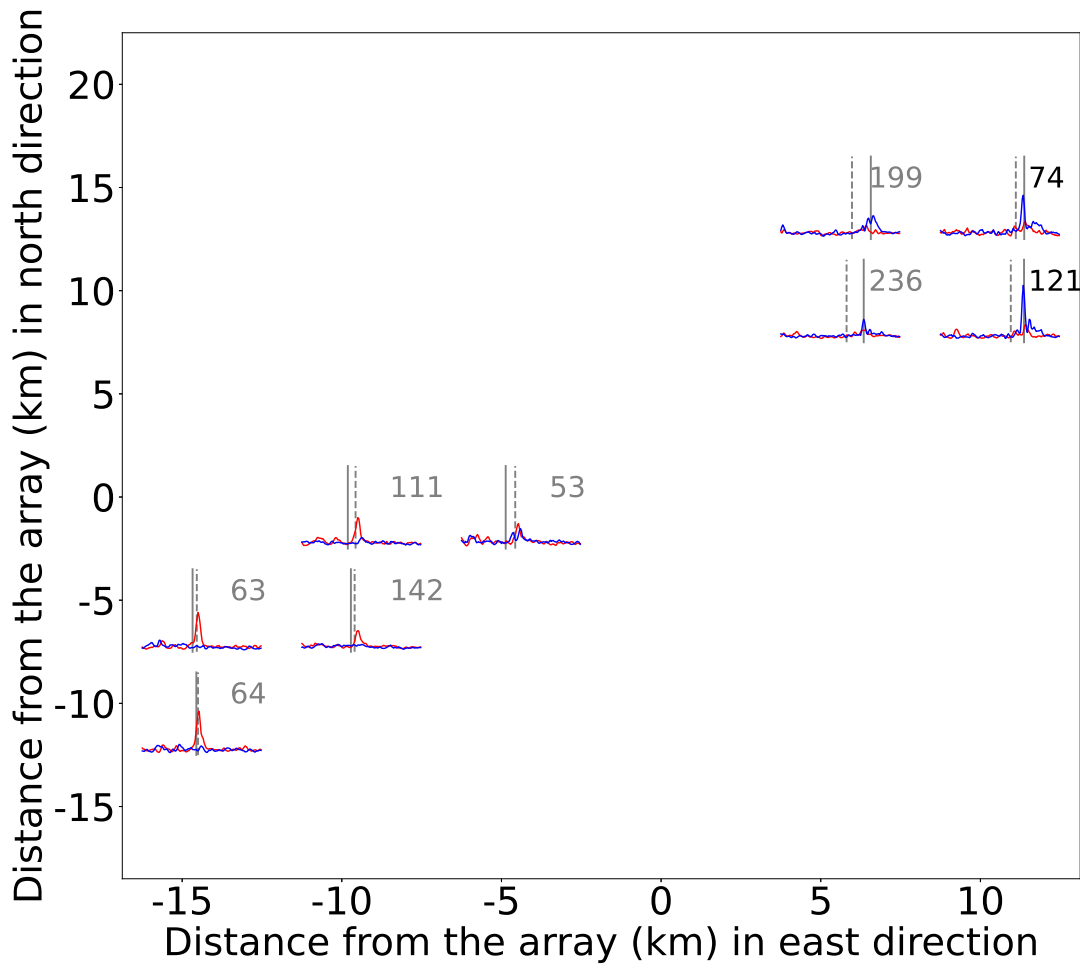


FIGURE A.4: Stacks of the envelopes of the cross correlation signals for different positions of the tremor source relative to the Gold Creek array. See caption of Figure 2.4 from the main text for an explanation of this figure.

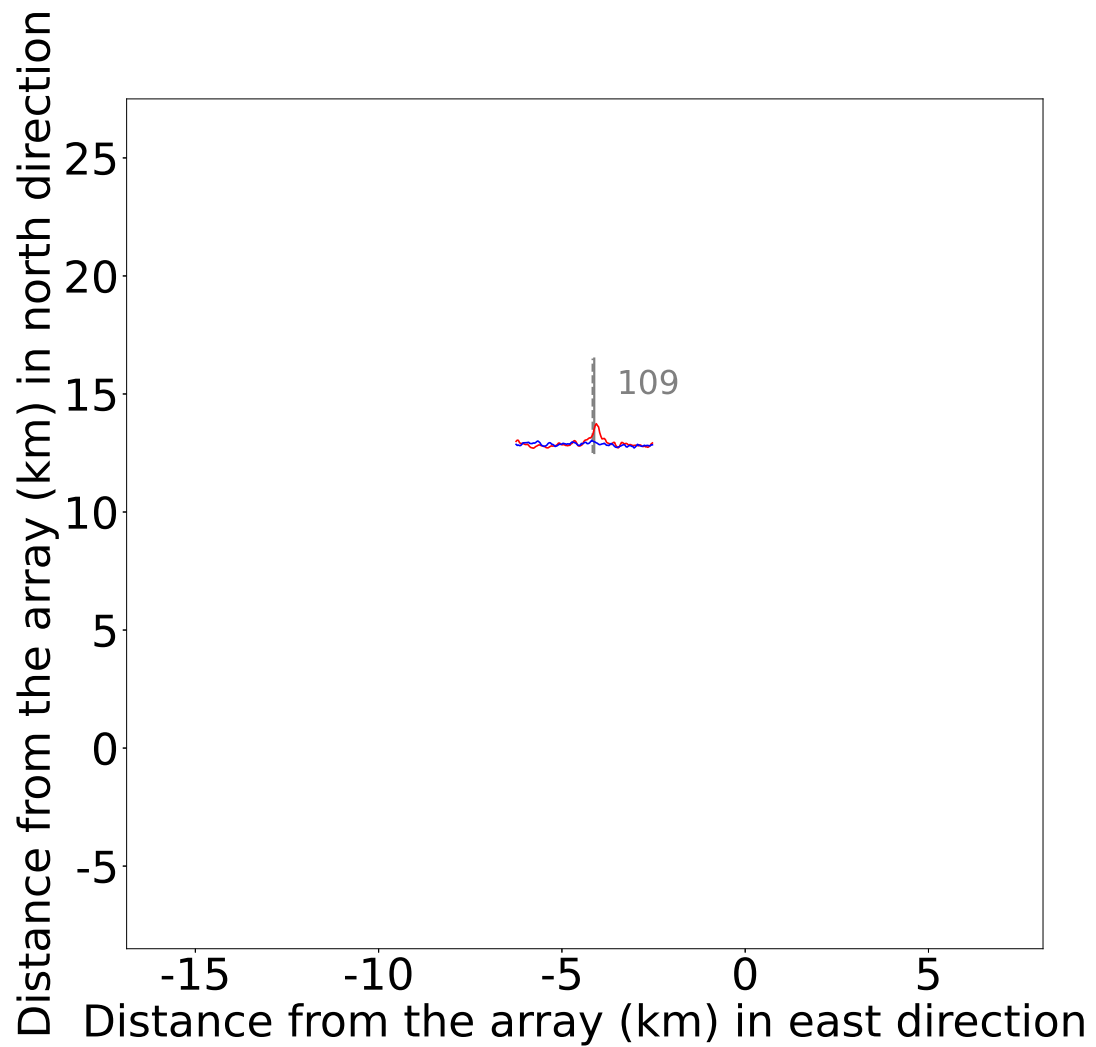


FIGURE A.5: Stacks of the envelopes of the cross correlation signals for different positions of the tremor source relative to the Lost Cause array. See caption of Figure 2.4 from the main text for an explanation of this figure.

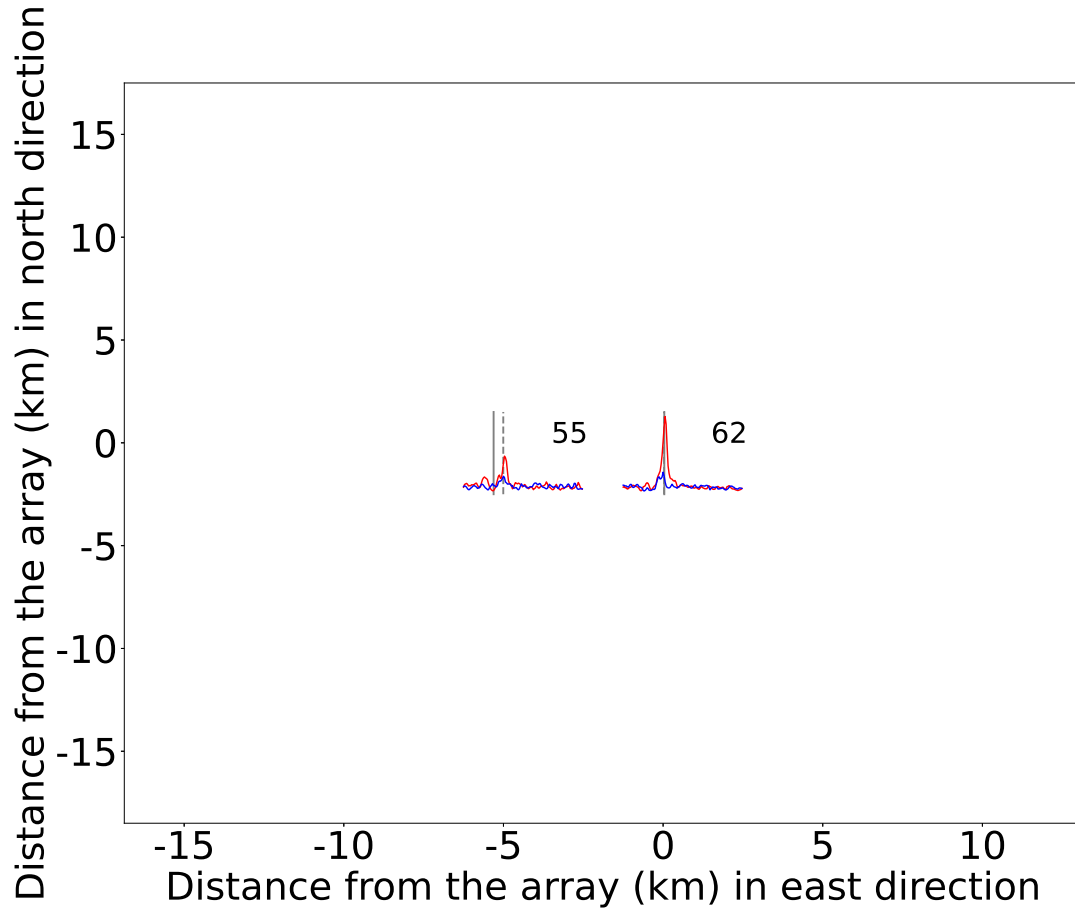


FIGURE A.6: Stacks of the envelopes of the cross correlation signals for different positions of the tremor source relative to the Port Angeles array. See caption of Figure 2.4 from the main text for an explanation of this figure.

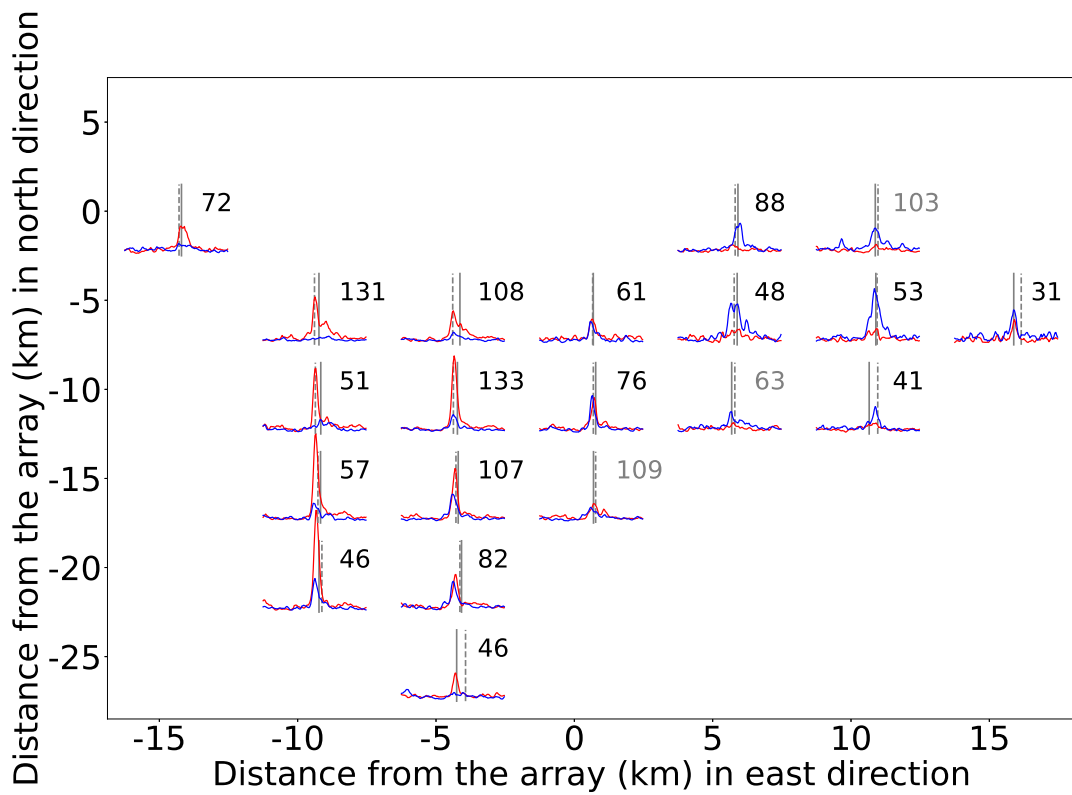


FIGURE A.7: Stacks of the envelopes of the cross correlation signals for different positions of the tremor source relative to the Three Bumps array. See caption of Figure 2.4 from the main text for an explanation of this figure.

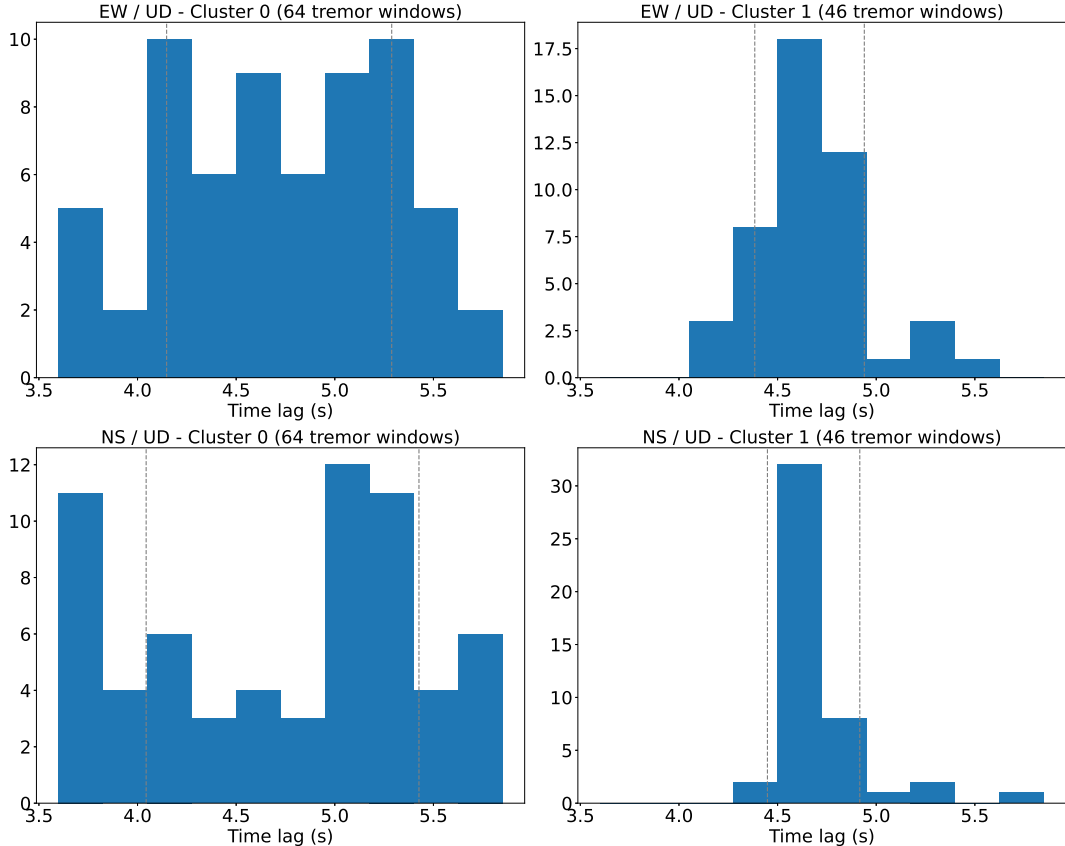


FIGURE A.8: Time lags between the time corresponding to the maximum absolute value for the cross-correlation function and the time corresponding to the maximum absolute value for the stacked cross-correlation are computed for each time window for which the source of the tremor is located on a grid cell. The distribution of the time lags is shown for the time windows in cluster 0 (that is the time windows that do not fit well with the stack, left panel) and in cluster 1 (that is the time windows that fit well with the stack, right panel). Top panels are the cross-correlation of the EW component with the vertical component, and bottom panels are the cross-correlation of the NS component with the vertical component. The grey dashed lines correspond to the mean plus or minus the standard deviation. The array and the grid cell are the same as in Figures 2.1 and 2.2 from the main text

Appendix B

Supplement for Chapter 3

TABLE B.1: Temporary stations used for the 2007-2009 catalog. The data centers providing the seismic waveforms are the Incorporated Research Institutions for Seismology (IRIS) (Alan Levander, 2007), and the Northern California Earthquake Data Center (NCEDC), doi:10.7932/NCEDC.

Station	Network	Channels	Location	Data center	Latitude	Longitude	Begin time	End time
B039	PB	EH1,EH2,EHZ	–	IRIS	41.4667	-122.4847	2007-10-15	3000-01-01
KCPB	NC	HHE,HHN,HHZ	–	NCEDC	39.6863	-123.5824	2002-10-17	3000-01-01
KHBB	NC	HHE,HHN,HHZ	–	NCEDC	40.6599	-123.2197	2003-09-11	3000-01-01
KRMB	NC	HHE,HHN,HHZ	–	NCEDC	41.5230	-123.9080	2001-06-16	3000-01-01
KSBX	NC	HHE,HHN,HHZ	–	NCEDC	41.8304	-123.8769	2001-07-13	3000-01-01
ME01	XQ	BHE,BHN,BHZ	01	IRIS	41.7752	-123.4034	2007-07-31	2009-06-12
ME02	XQ	BHE,BHN,BHZ	01	IRIS	41.6898	-122.3372	2007-07-22	2009-05-20
ME03	XQ	BHE,BHN,BHZ	01	IRIS	41.702	-123.881	2007-09-27	2009-06-13
ME04	XQ	BHE,BHN,BHZ	01	IRIS	41.355	-123.514	2007-07-23	2009-06-12
ME08	XQ	BHE,BHN,BHZ	01	IRIS	40.222	-123.305	2007-07-22	2009-06-03
ME09	XQ	BHE,BHN,BHZ	01	IRIS	41.086	-122.726	2007-07-21	2009-05-14
ME10	XQ	BHE,BHN,BHZ	01	IRIS	40.9591	-122.4619	2007-10-31	2009-06-12
ME12	XQ	BHE,BHN,BHZ	01	IRIS	40.104	-122.498	2007-07-20	2009-06-12
ME13	XQ	BHE,BHN,BHZ	01	IRIS	40.764	-122.918	2007-07-22	2009-06-12
ME16	XQ	BHE,BHN,BHZ	01	IRIS	40.577	-122.087	2007-07-20	2008-10-14
ME24	XQ	BHE,BHN,BHZ	01	IRIS	40.359	-122.047	2007-07-19	2009-05-15
ME26	XQ	BHE,BHN,BHZ	01	IRIS	40.157	-122.099	2007-07-26	2009-02-17
ME27	XQ	BHE,BHN,BHZ	01	IRIS	40.453	-123.155	2008-01-01	2009-06-13
ME28	XQ	BHE,BHN,BHZ	01	IRIS	40.327	-122.471	2007-07-20	2009-05-14
ME29	XQ	BHE,BHN,BHZ	01	IRIS	41.142	-123.1408	2007-09-21	2009-06-13
ME30	XQ	BHE,BHN,BHZ	01	IRIS	40.843	-123.565	2007-07-24	2009-06-22
ME42	XQ	BHE,BHN,BHZ	01	IRIS	39.7145	-123.273	2007-07-15	2009-06-16
ME43	XQ	BHE,BHN,BHZ	01	IRIS	39.5703	-123.175	2007-09-16	2009-06-16
ME44	XQ	BHE,BHN,BHZ	01	IRIS	39.4928	-123.187	2007-09-16	2009-06-15
ME45	XQ	BHE,BHN,BHZ	01	IRIS	39.4666	-122.9595	2007-09-12	2009-06-09
ME46	XQ	BHE,BHN,BHZ	01	IRIS	39.196	-122.968	2007-09-25	2009-06-11
ME47	XQ	BHE,BHN,BHZ	01	IRIS	39.1124	-122.8106	2007-09-25	2008-09-17
ME49	XQ	BHE,BHN,BHZ	01	IRIS	39.8633	-123.7194	2007-09-25	2009-06-08
ME52	XQ	BHE,BHN,BHZ	01	IRIS	39.3228	-123.2191	2008-02-21	2009-07-08
ME54	XQ	BHE,BHN,BHZ	01	IRIS	39.0132	-123.3779	2007-09-24	2009-03-03
ME57	XQ	BHE,BHN,BHZ	01	IRIS	39.9118	-122.5676	2007-10-24	2009-06-11
WDC	BK	BHE,BHN,BHZ	–	NCEDC	40.5799	-122.5411	1992-09-17	2011-05-06
YBH	BK	BHE,BHN,BHZ	–	NCEDC	41.7320	-122.7104	1993-07-24	2011-06-03

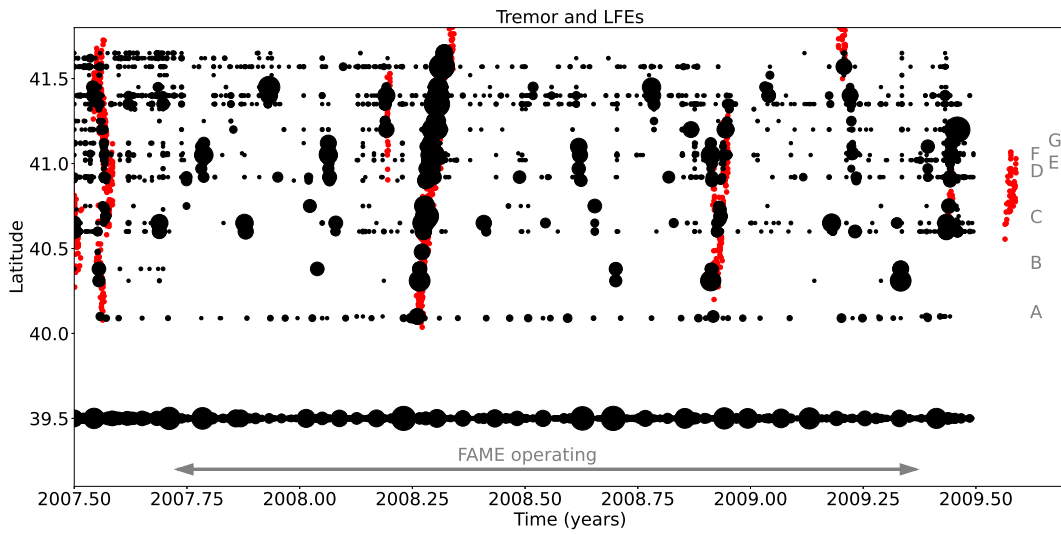


FIGURE B.1: Same as Figure 3.3, but without filtering the LFEs. There are many false detections at the beginning and the end of the catalog because the FAME stations were not yet installed / already removed.

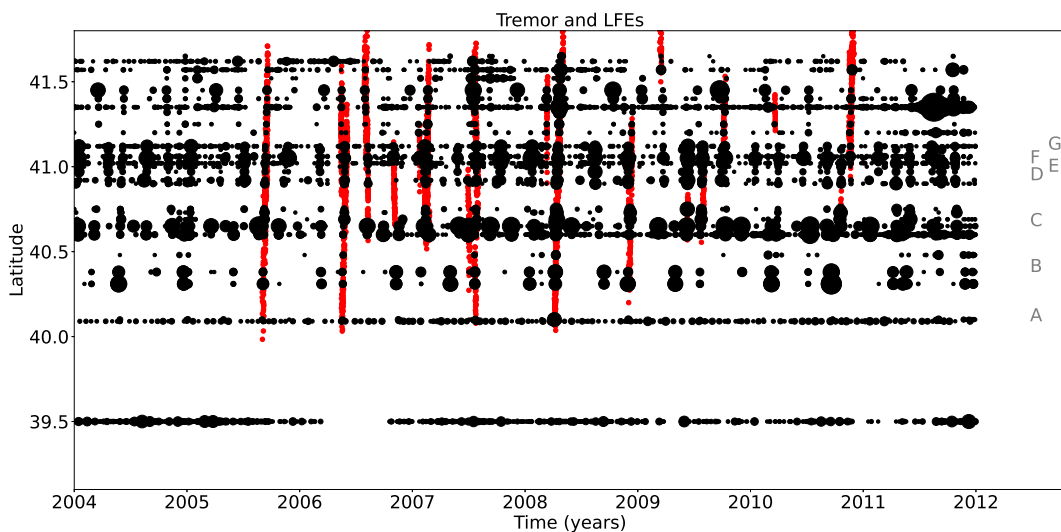


FIGURE B.2: Same as Figure 3.6, but without filtering the LFEs.

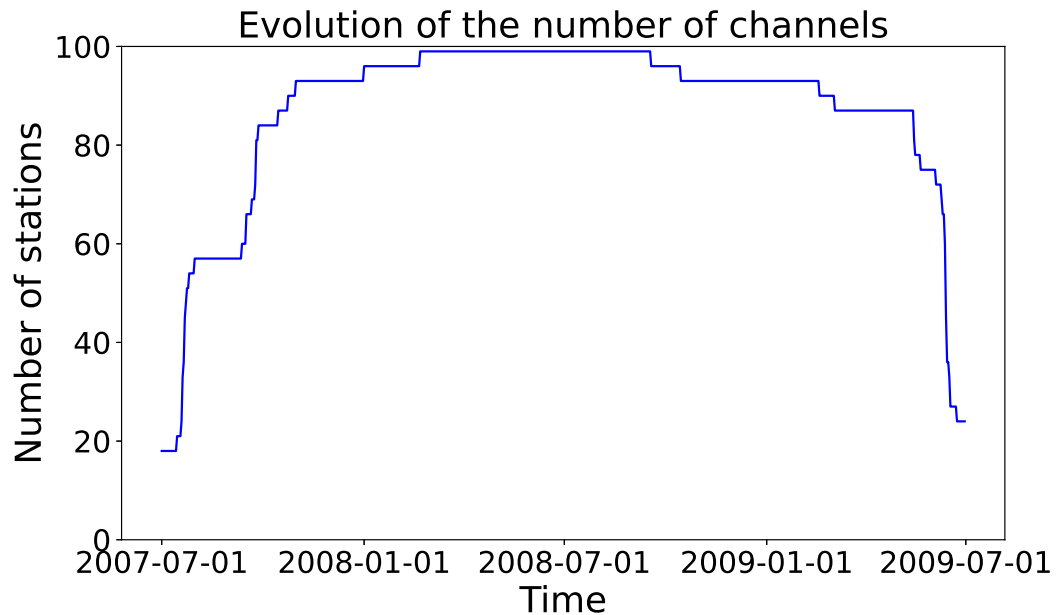


FIGURE B.3: Evolution of the number of channels available for the computation of the 2007-2009 catalog using the temporary FAME stations.

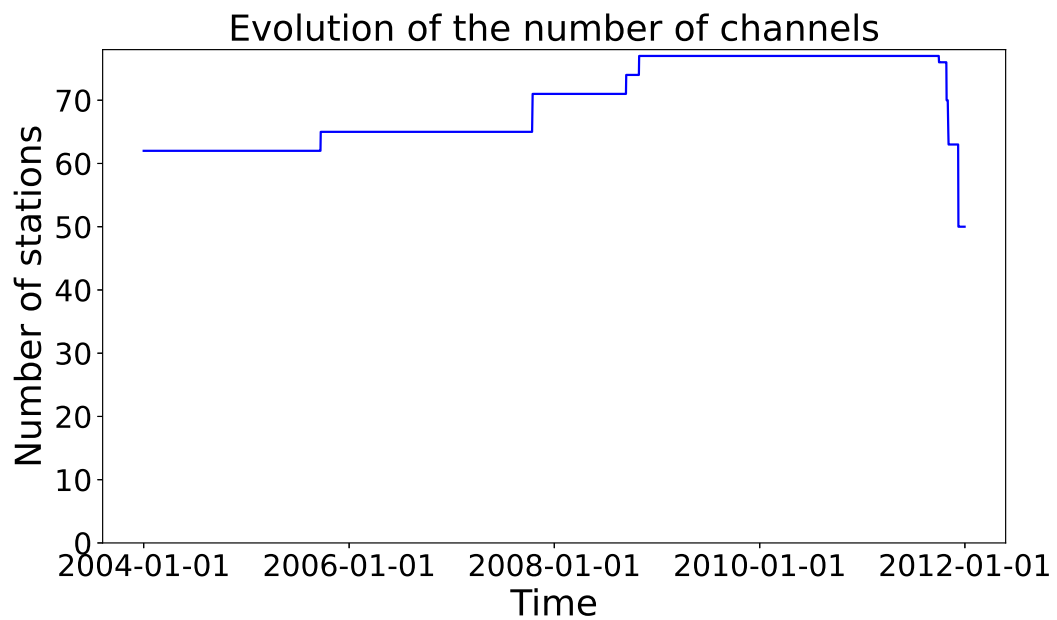


FIGURE B.4: Evolution of the number of channels available for the computation of the 2004-2011 catalog using the permanent stations.

TABLE B.2: Permanent stations used for the 2004-2011 catalog. The data centers providing the seismic waveforms are the Incorporated Research Institutions for Seismology (IRIS) (Alan Levander, 2007), and the Northern California Earthquake Data Center (NCEDC), doi:10.7932/NCEDC.

Station	Network	Channels	Location	Data center	Latitude	Longitude	Begin time	End time
B039	PB	EH1,EH2,EHZ	-	IRIS	41.4667	-122.4847	2007-10-15	3000-01-01
B040	PB	EH1,EH2,EHZ	-	IRIS	41.8308	-122.4205	2007-10-16	3000-01-01
B933	PB	EH1,EH2,EHZ	-	IRIS	40.0600	-123.9690	2008-09-13	3000-01-01
B935	PB	EH1,EH2,EHZ	-	IRIS	40.4787	-123.5732	2008-10-29	3000-01-01
GASB	BK	BHE,BHN,BHZ	-	NCEDC	39.65471	-122.71595	2005-09-22	2011-06-16
GASB	BK	BHE,BHN,BHZ	0	NCEDC	39.65471	-122.71595	2011-06-16	3000-01-01
GBB	NC	EHZ	-	NCEDC	39.80127	-122.34550	2000-12-06	3000-01-01
GHM	NC	EHZ	-	NCEDC	39.49545	-122.93096	1984-01-01	3000-01-01
GRO	NC	EHZ	-	NCEDC	39.91684	-122.67117	1990-12-13	3000-01-01
GSN	NC	EHZ	-	NCEDC	38.94040	-123.19245	1984-01-01	2018-12-11
GTC	NC	SHZ	-	NCEDC	39.39944	-123.55532	1996-08-01	2011-10-27
GVV	NC	EHZ	-	NCEDC	39.77510	-122.67551	2002-04-28	3000-01-01
HOPS	BK	BHE,BHN,BHZ	-	NCEDC	38.99349	-123.07234	1994-10-21	2010-06-16
HOPS	BK	BHE,BHN,BHZ	0	NCEDC	38.99349	-123.07234	2010-06-16	3000-01-01
JCC	BK	BHE,BHN,BHZ	-	NCEDC	40.81745	-124.02955	2001-04-11	2010-08-19
JCC	BK	BHE,BHN,BHZ	0	NCEDC	40.81745	-124.02955	2010-08-19	3000-01-01
KBN	NC	SHZ	-	NCEDC	39.89237	-123.19503	1994-11-28	2011-10-27
KBS	NC	SHZ	-	NCEDC	39.91719	-123.59561	2002-10-17	2011-10-27
KCPB	NC	HHE,HHN,HHZ	-	NCEDC	39.68631	-123.58242	2002-10-17	3000-01-01
KCS	NC	SHZ	-	NCEDC	40.53791	-123.51394	1994-11-28	2011-11-01
KFP	NC	SHZ	-	NCEDC	39.63889	-123.42514	1994-11-28	2011-10-27
KHBB	NC	HHE,HHN,HHZ	-	NCEDC	40.65990	-123.21966	2003-09-11	3000-01-01
KHMB	NC	HHE,HHN,HHZ	-	NCEDC	40.87475	-123.73259	2002-06-13	3000-01-01
KIP	NC	SHZ	-	NCEDC	39.80841	-123.48130	1994-11-28	2011-10-27
KKP	NC	SHZ	-	NCEDC	40.14579	-123.46965	1994-11-28	2011-11-01
KOM	NC	SHZ	-	NCEDC	41.27872	-123.45315	1994-11-28	2011-11-02
KPP	NC	SHZ	-	NCEDC	40.34579	-123.36328	1994-11-28	2011-11-01
KRK	NC	SHZ	-	NCEDC	39.56315	-123.18367	1994-11-28	2011-10-27
KRMB	NC	HHE,HHN,HHZ	-	NCEDC	41.52296	-123.90797	2001-06-16	3000-01-01
KRP	NC	HHE,HHN,HHZ	-	NCEDC	41.15765	-124.02330	2002-06-12	3000-01-01
KSXB	NC	HHE,HHN,HHZ	-	NCEDC	41.83038	-123.87688	2001-07-13	3000-01-01
KTR	NC	SHZ	-	NCEDC	41.90847	-123.37755	1994-11-28	2011-11-02
LAM	NC	SHZ	-	NCEDC	41.60987	-122.62559	1994-11-28	2011-09-30
LBF	NC	SHZ	-	NCEDC	41.34707	-121.89098	1994-11-28	2011-11-03
LBK	NC	SHZ	-	NCEDC	41.08382	-122.66731	1994-11-28	2011-12-08
LBP	NC	SHZ	-	NCEDC	40.31671	-122.88193	1994-11-28	2011-12-08
LDB	NC	SHZ	-	NCEDC	40.43105	-121.78632	1994-11-28	2011-12-08
LGB	NC	SHZ	-	NCEDC	41.33418	-122.18771	2001-10-20	2011-11-03
LGP	NC	SHZ	-	NCEDC	40.91228	-122.82949	1994-11-28	2011-12-08
LPG	NC	SHZ	-	NCEDC	40.14514	-122.68788	1994-11-28	2011-12-08
LRB	NC	SHZ	-	NCEDC	40.14323	-122.55772	1994-11-28	2011-12-08
LRR	NC	SHZ	-	NCEDC	40.46630	-121.62230	1994-11-28	2011-12-08
LSF	NC	SHZ	-	NCEDC	40.65817	-122.52371	1994-11-28	2011-12-08
LSH	NC	SHZ	-	NCEDC	40.79294	-122.03943	2002-03-28	2011-12-08
LSR	NC	SHZ	-	NCEDC	41.10696	-122.27062	1994-11-28	2011-12-08
LTC	NC	SHZ	-	NCEDC	40.20842	-122.12548	2002-03-28	2011-12-08
LVR	NC	SHZ	-	NCEDC	40.03937	-122.67250	1994-11-28	2011-12-08
LWH	NC	SHZ	-	NCEDC	40.64180	-121.94857	1994-11-28	2011-12-08
WDC	BK	BHE,BHN,BHZ	-	NCEDC	40.57988	-122.54113	1992-09-17	2011-05-06
WDC	BK	BHE,BHN,BHZ	0	NCEDC	40.57988	-122.54113	2011-05-06	3000-01-01
YBH	BK	BHE,BHN,BHZ	-	NCEDC	41.73204	-122.71039	1993-07-24	2011-06-03
YBH	BK	BHE,BHN,BHZ	0	NCEDC	41.73204	-122.71039	2011-06-03	3000-01-01

TABLE B.3: Thresholds used to clean the catalogs. An LFE is kept in the catalog if its cross-correlation value multiplied by the number of channels recording when it was detected is higher than the threshold. The threshold is missing for the families for which there were not enough permanent stations with good templates to obtain reliable LFE detections.

Family	Threshold 2007-2009 FAME catalog	Threshold 2007-2009 networks catalog
080401.05.050	1.4	1.9
080405.11.042	2.0	1.6
080408.08.007	1.7	1.5
080408.15.023	2.0	1.3
080408.08.029	2.3	1.4
080408.16.026	1.8	1.4
080410.01.050	3.5	1.3
080410.09.032	3.9	1.4
080410.12.039	1.9	1.3
080410.12.040	5.4	2.3
080411.04.013	3.4	1.5
080411.04.023	3.6	1.5
080410.13.055	1.9	1.3
080412.03.029	2.2	1.0
080412.11.038	2.2	1.3
080412.22.047	3.2	1.5
080413.13.026	2.2	1.3
080412.22.040	3.5	1.6
080413.07.015	2.0	1.6
080413.07.023	1.8	1.4
080413.16.058	2.2	0.1
080413.18.013	2.6	1.2
080413.20.036	2.1	1.1
080414.12.016	2.0	1.2
080414.12.020	1.5	1.2
080414.10.058	1.8	1.2
080414.18.003	NA	NA
080415.11.006	4.6	1.6
080415.11.008	3.0	1.8
080415.24.028	2.5	1.7
080416.15.003	2.8	1.7
080418.03.001	5.0	1.5
080415.19.030	2.9	1.9
080419.24.054	3.4	2.2
080416.13.033	3.9	2.0
080417.15.043	3.3	1.7
080418.02.049	3.7	1.6
080419.04.046	3.5	1.5
080420.01.019	2.3	1.6
080420.04.009	2.2	1.4
080420.05.032	3.0	1.8
080420.08.042	1.8	1.5
080421.14.048	2.1	1.6

Family	Threshold 2007-2009 FAME catalog	Threshold 2007-2009 networks catalog
080421.15.050	1.9	1.5
080421.16.053	3.0	1.4
080421.16.054	2.3	1.4
080421.17.056	2.1	1.3
080421.23.033	2.7	1.4
080422.13.003	3.2	1.7
080422.12.039	1.7	1.1
080422.13.043	2.7	1.6
080422.15.030	2.0	1.5
080424.04.058	3.3	1.8
080424.05.060	2.2	1.7
080426.05.008	1.8	1.6
080426.06.027	2.1	1.8
080426.20.030	1.5	1.7
080427.04.052	2.5	1.5
080427.13.036	2.1	1.5
080427.20.043	2.5	2.0
080429.15.005	NA	NA
080326.07.004	NA	NA
080326.07.048	NA	NA
080326.08.015	2.7	1.0
080326.09.007	NA	NA
080328.09.029	NA	NA

Bibliography

- Aguiar, A. C., T. I. Melbourne, and C. W. Scrivner (2009). "Moment release rate of Cascadia tremor constrained by GPS". In: *J. Geophys. Res.* 114, B00A05.
- Alba, S., R. J. Weldon, D. Livelybrooks, and D. A. Schmidt (2019). "Cascadia ETS events seen in tidal records (1980–2011)". In: *Bull. Seismol. Soc. Am.* 109.2, pp. 812–821.
- Audet, P. and R. Bürgmann (2014). "Possible control of subduction zone slow-earthquake periodicity by silica enrichment". In: *Nature* 510, pp. 389–393.
- Audet, P. and Y. H. Kim (2016). "Teleseismic constraints on the geological environment of deep episodic slow earthquakes in subduction zone forearcs: A review". In: *Tectonophysics* 670, pp. 1–15.
- Audet, P., M. G. Bostock, N. I. Christensen, and S. M. Peacock (2009). "Seismic evidence for overpressured subducted oceanic crust and megathrust fault sealing". In: *Nature* 457, pp. 76–78.
- Baratin, L. M., C. J. Chamberlain, J. Townend, and M. K. Savage (2018). "Focal mechanisms and inter-event times of low-frequency earthquakes reveal quasi-continuous deformation and triggered slow slip on the deep Alpine Fault". In: *Earth and Planetary Science Letters* 484, pp. 111–123.
- Beroza, G. C. and S. Ide (2011). "Slow earthquakes and nonvolcanic tremor". In: *Annu. Rev. Earth Planet. Sci.* 39, pp. 271–296.
- Beroza, G. C. and T. H. Jordan (1990). "Searching for slow and silent earthquakes using free oscillations". In: *Journal of Geophysical Research: Solid Earth* 95.B3, pp. 2485–2510.
- Bostock, M. G. (2013). "The Moho in subduction zones". In: *Tectonophysics* 609, pp. 547–557.
- Bostock, M. G., A. A. Royer, E. H. Hearn, and S. M. Peacock (2012). "Low frequency earthquakes below southern Vancouver Island". In: *Geochemistry Geophysics Geosystems* 13, Q11007.
- Bostock, M. G., A. M. Thomas, G. Savard, L. Chuang, and A. M. Rubin (2015). "Magnitudes and moment-duration scaling of low-frequency earthquakes beneath southern Vancouver Island". In: *Journal of Geophysical Research: Solid Earth* 120, pp. 6329–6350.
- Boyarko, D. C., M. R. Brudzinski, R. W. Porritt, R. M. Allen, and A. M. Tréhu (2015). "Automated detection and location of tectonic tremor along the entire Cascadia margin from 2005 to 2011". In: *Earth and Planetary Science Letters* 430, pp. 160–170.
- Brudzinski, M. R. and R. M. Allen (2007). "Segmentation in episodic tremor and slip all along Cascadia". In: *Geology* 35.10, pp. 907–910.
- Cassidy, J. F. and M. G. Bostock (1996). "Shear-wave splitting above the subducting Juan de Fuca plate". In: *Geophysical Research Letters* 23.9, pp. 941–944.
- Chestler, S. R. and K. C. Creager (2017a). "Evidence for a scale-limited low-frequency earthquake source process". In: *Journal of Geophysical Research. Solid Earth* 122, pp. 3099–3114.
- (2017b). "A model for low-frequency earthquake slip". In: *Geochemistry, Geophysics, Geosystems* 18, pp. 4690–4708.

- De Lauro, E., S. De Martino, M. Falanga, and S. Petrosino (2016). "Fast wavefield decomposition of volcano-tectonic earthquakes into polarized P and S waves by Independent Component Analysis". In: *Tectonophysics* 690, pp. 355–361.
- Dragert, H., K. Wang, and T. S. James (2001). "A silent slip event on the deeper Cascadia subduction interface". In: *Science* 292.5521, pp. 1525–1528.
- Ducellier, Ariane (2021). *ArianeDucellier/timelags: Revised manuscript*. Version v2.0. DOI: [10.5281/zenodo.5725990](https://doi.org/10.5281/zenodo.5725990). URL: <https://doi.org/10.5281/zenodo.5725990>.
- (2022a). *ArianeDucellier/catalog: Revised manuscript*. Version v2. DOI: [10.5281/zenodo.5962414](https://doi.org/10.5281/zenodo.5962414). URL: <https://doi.org/10.5281/zenodo.5962414>.
- (2022b). *ArianeDucellier/slowslip*. URL: <https://github.com/ArianeDucellier/slowslip>.
- Fagereng, Å. and J. F. A. Diener (2011). "Non-volcanic tremor and discontinuous slab dehydration". In: *Geophysical Research Letters* 38, p. L15302.
- Fagereng, Å., G. W. B. Hillary, and J. F. A. Diener (2014). "Brittle-viscous deformation, slow slip, and tremor". In: *Geophysical Research Letters* 41.12, pp. 4159–4167.
- Frank, W. B. (2016). "Slow slip hidden in the noise: The intermittence of tectonic release". In: *Geophys. Res. Lett.* 43, pp. 10125–10133.
- Frank, W. B., N. M. Shapiro, A. L. Husker, V. Kostoglodov, A. Romanenko, and M. Campillo (2014). "Using systematically characterized low-frequency earthquakes as a fault probe in Guerrero, Mexico". In: *Journal of Geophysical Research: Solid Earth* 119, pp. 7686–7700.
- Ghosh, A., J. E. Vidale, and K. C. Creager (2012). "Tremor asperities in the transition zone control evolution of slow earthquakes". In: *Journal of Geophysical Research* 117, B10301.
- Ghosh, A., J. E. Vidale, J. R. Sweet, K. C. Creager, A. G. Wech, and H. Houston (2010a). "Tremor bands sweep Cascadia". In: *Geophysical Research Letters* 37, p. L08301.
- Ghosh, A., J. E. Vidale, J. R. Sweet, K. C. Creager, A. G. Wech, H. Houston, and E. E. Brodsky (2010b). "Rapid, continuous streaking of tremor in Cascadia". In: *Geochemistry, Geophysics, Geosystems* 11, Q12010.
- Gibbons, S. J. and F. Ringdal (2006). "The detection of low magnitude seismic events using array-based waveform correlation". In: *Geophysical Journal International* 165, pp. 149–166.
- GPS/GNSS Network and Geodesy Laboratory: Central Washington University, other / seismic network (1996). *Pacific Northwest Geodetic Array (PANGA)*. DOI: [10.7914/SN/PW](https://doi.org/10.7914/SN/PW). URL: <http://www.panga.cwu.edu/>.
- Guilhem, A., Z. Peng, and R. M. Nadeau (2010). "High-frequency identification of non-volcanic tremor triggered by regional earthquakes". In: *Geophysical Research Letters* 37, p. L16309.
- Han, J., J. E. Vidale, H. Houston, K. Chao, and K. Obara (2014). "Triggering of tremor and inferred slow slip by small earthquakes at the Nankai subduction zone in southwest Japan". In: *Geophysical Research Letters* 41, pp. 8053–8060.
- Hirose, H., K. Hirahara, F. Kimata, N. Fujii, 2, and S. Miyazaki (1999). "A slow thrust slip event following the two 1996 Hyuganada earthquakes beneath the Bungo Channel, southwest Japan". In: *Geophysical Research Letters* 26.21, pp. 3237–3240.
- Houston, H. (2015). "Low friction and fault weakening revealed by rising sensitivity of tremor to tidal stress". In: *Nature Geoscience* 8.5, pp. 409–415.
- Houston, H., B. G. Delbridge, A. G. Wech, and K. C. Creager (2011). "Rapid tremor reversals in Cascadia generated by a weakened plate interface". In: *Nature Geoscience* 4, pp. 404–409.

- Hyndman, R. D., P. A. McCrory, A. Wech, H. Kao, and Ague J. (2015). "Cascadia subducting plate fluids channelled to fore-arc mantle corner: ETS and silica deposition". In: *Journal of Geophysical Research Solid Earth* 120, pp. 4344–4358.
- Ide, S. (2012). "Variety and spatial heterogeneity of tectonic tremor worldwide". In: *Journal of Geophysical Research* 117, B03302.
- Ide, S., D. R. Shelly, and G. C. Beroza (2007). "Mechanism of deep low frequency earthquakes: Further evidence that deep non-volcanic tremor is generated by shear slip on the plate interface". In: *Geophysical Research Letters* 34, p. L03308.
- Ide, S., G. C. Beroza, D. R. Shelly, and T. Uchide (2007). "A scaling law for slow earthquakes". In: *Nature* 447, pp. 76–79.
- Jones, J. P., R. Carniel, and S. D. Malone (2012). "Subband decomposition and reconstruction of continuous volcanic tremor". In: *Journal of Volcanology and Geothermal Research* 213-214, pp. 98–115.
- Kao, H., D.-J. Shan, H. Dragert, G. Rogers, J. F. Cassidy, and K. Ramachandran (2005). "A wide depth distribution of seismic tremors along the northern Cascadia margin". In: *Nature* 436.
- Kao, H., S.-J. Shan, H. Dragert, G. Rogers, J. F. Cassidy, K. Wang, T. S. James, and K. Ramachandran (2006). "Spatial-temporal patterns of seismic tremors in northern Cascadia". In: *Journal of Geophysical Research* 111, B03309.
- Kao, H., S.-J. Shan, H. Dragert, and G. Rogers (2009). "Northern Cascadia episodic tremor and slip: A decade of tremor observations from 1997 to 2007". In: *Journal of Geophysical Research* 114, B00A12.
- Kato, A. and S. Nakagawa (2020). "Detection of deep low-frequency earthquakes in the Nankai subduction zone over 11 years using a matched filter technique". In: *Earth, Planets and Space* 72, p. 128.
- Katsumata, A. and N. Kamaya (2003). "Low-frequency continuous tremor around the Moho discontinuity away from volcanoes in the southwest Japan". In: *Geophysical Research Letters* 30.1, p. 1020.
- Kumar, P. and E. Foufoula-Georgiou (1997). "Wavelet analysis for geophysical applications". In: *Rev. Geophys.* 35.4, pp. 385–412.
- La Rocca, M., K. C. Creager, D. Galluzzo, S. Malone, J. E. Vidale, J. R. Sweet, and A. G. Wech (2009). "Cascadia tremor located near plate interface constrained by S minus P wave times". In: *Science* 323, pp. 620–623.
- Levander, A. (2007). *Seismic and Geodetic Investigations of Mendocino Triple Junction Dynamics*. DOI: [10.7914/SN/XQ_2007](https://doi.org/10.7914/SN/XQ_2007). URL: https://www.fdsn.org/networks/detail/XQ_2007/.
- McCrory, P. A., J. L. Blair, D. H. Oppenheimer, and S. R. Walter (2006). *Depth to the Juan de Fuca slab beneath the Cascadia subduction margin - A 3-D model sorting earthquakes*. Tech. rep. Series 91. U.S. Geological Survey.
- Merrill, R., M. G. Bostock, S. M. Peacock, A. J. Calvert, and N. I. Christensen (2020). "A double difference tomography study of the Washington Forearc: Does Siletzia control crustal seismicity?" In: *Journal of Geophysical Research: Solid Earth* 125, e2020JB019750.
- Michel, S., A. Gualandi, and J.-P. Avouac (2019). "Interseismic coupling and slow slip events on the Cascadia megathrust". In: *Pure Appl. Geophys.* 176, pp. 3867–3891.
- Miller, M. M., T. Melbourne, D. J. Johnson, and W. Q. Sumner (2002). "Periodic slow earthquakes from the Cascadia subduction zone". In: *Science* 295.5564, p. 2423.
- Miyazawa, M., E. E. Brodsky, and J. Mori (2008). "Learning from dynamic triggering of low-frequency tremor in subduction zones". In: *Earth, Planets and Space* 60, e17–e20.

- Nakamura, M. (2017). "Distribution of low-frequency earthquakes accompanying the very low frequency earthquakes along the Ryukyu Trench". In: *Earth, Planets, and Space* 69.1, pp. 1–17.
- Nakata, R., N. Suda, and H. Tsuruoka (2008). "Non-volcanic tremor resulting from the combined effect of Earth tides and slow slip events". In: *Nature Geoscience* 1, pp. 676–678.
- Nikulin, A., V. Levin, and J. Park (2009). "Receiver function study of the Cascadia megathrust: Evidence for localized serpentinization". In: *Geochemistry, Geophysics, Geosystems* 10, Q07004.
- Obara, K. (2002). "Nonvolcanic deep tremor associated with subduction in southwest Japan". In: *Science* 296.5573, pp. 1679–1681.
- Obara, K., H. Hirose, F. Yamamizu, and K. Kasahara (2004). "Episodic slow slip events accompanied by non-volcanic tremors in southwest Japan subduction zone". In: *Geophysical Research Letters* 31, p. L23602.
- Ohta, K. and S. Ide (2017). "Resolving the detailed spatiotemporal slip evolution of deep tremor in Western Japan". In: *Journal of Geophysical Research: Solid Earth* 122.12, pp. 10009–10036.
- Ohtani, R., J. J. McGuire, and P. Segall (2010). "Network strain filter: A new tool for monitoring and detecting transient deformation signals in GPS arrays". In: *J. Geophys. Res.* 115, B12418.
- Peacock, S. M. (2009). "Thermal and metamorphic environment of subduction zone episodic tremor and slip". In: *Journal of Geophysical Research* 114, B00A07.
- Pedregosa, F., G. Varoquaux, A. Gramfort, V. Michel, B. Thirion, O. Grisel, M. Blondel, P. Prettenhofer, R. Weiss, V. Dubourg, J. Vanderplas, A. Passos, D. Cournapeau, M. Brucher, M. Perrot, and E. Duchesnay (2011). "Scikit-learn: Machine Learning in Python". In: *Journal of Machine Learning Research* 12, pp. 2825–2830.
- Peng, Z., J. E. Vidale, A. G. Wech, R. M. Nadeau, and K. C. Creager (2009). "Remote triggering of tremor along the San Andreas Fault in central California". In: *Journal of Geophysical Research* 114, B00A06.
- Percival, D. B. and A. T. Walden (2000). *Wavelet Methods for Time Series Analysis*. Cambridge Series in Statistical and Probabilistic Mathematics. New York, NY, USA: Cambridge University Press.
- Plourde, A. P., M. G. Bostock, P. Audet, and A. M. Thomas (2015). "Low-frequency earthquakes at the southern Cascadia margin". In: *Geophysical Research Letters* 42, pp. 4849–4855.
- Preston, L. A., K. C. Creager, R. S. Crosson, T. M. Brocher, and A. M. Trehu (2003). "Intraslab earthquakes: Dehydration of the Cascadia slab". In: *Science* 302, pp. 1197–1200.
- Rogers, G. and H. Dragert (2003). "Tremor and slip on the Cascadia subduction zone: The chatter of silent slip". In: *Science* 300.5627, pp. 1942–1943.
- Rousseeuw, P. J. and C. Croux (1993). "Alternatives to the median absolute deviation". In: *Journal of the American Statistical Association* 88.424, pp. 1273–1283.
- Rowe, C., J. Moore, and F. Remitti (2013). "The thickness of subduction plate boundary faults from the seafloor into the seismogenic zone". In: *Geology* 41.9, pp. 991–994.
- Royer, A. A. and M. G. Bostock (2014). "A comparative study of low frequency earthquake templates in northern Cascadia". In: *Earth and Planetary Science Letters* 402, pp. 247–256.
- Royer, A. A., A. M. Thomas, and M. G. Bostock (2015). "Tidal modulation and triggering of low-frequency earthquakes in northern Cascadia". In: *Journal of Geophysical Research Solid Earth* 120, pp. 384–405.

- Rubin, A. M. and J. G. Armbruster (2013). "Imaging slow slip fronts in Cascadia with high precision cross-station tremor locations". In: *Geochemistry Geophysics Geosystems* 14, pp. 5371–5392.
- Rubinstein, J. L., J. Gomberg, J. E. Vidale, A. G. Wech, H. Kao, K. C. Creager, and G. Rogers (2009). "Seismic wave triggering of nonvolcanic tremor, episodic tremor and slip, and earthquakes on Vancouver Island". In: *Journal of Geophysical Research Solid Earth* 114, B00A01.
- Sammis, C. G. and M. G. Bostock (2021). "A granular jamming model for low-frequency earthquakes". In: *Journal of Geophysical Research: Solid Earth* 126, e2021JB021963.
- Schimmel, M. and H. Paulssen (1997). "Noise reduction and detection of weak, coherent signals through phase-weighted stacks". In: *Geophysical Journal International* 130, pp. 487–505.
- Shelly, D. R. (2017). "A 15 year catalog of more than 1 million low-frequency earthquakes: Tracking tremor and slip along the deep San Andreas Fault". In: *Journal of Geophysical Research: Solid Earth* 122, pp. 3739–3753.
- Shelly, D. R., G. C. Beroza, and S. Ide (2007a). "Complex evolution of transient slip derived from precise tremor locations in western Shikoku, Japan". In: *Geochemistry, Geophysics, Geosystems* 8, Q10014.
- (2007b). "Non-volcanic tremor and low-frequency earthquake swarms". In: *Nature* 446, pp. 305–307.
- Shelly, D. R., G. C. Beroza, S. Ide, and S. Nakamura (2006). "Low-frequency earthquakes in Shikoku, Japan, and their relationship to episodic tremor and slip". In: *Nature* 442, pp. 188–192.
- Sweet, J. R., K. C. Creager, H. Houston, and S. R. Chestler (2019). "Variations in Cascadia low-frequency earthquake behavior with downdip distance". In: *Geochemistry, Geophysics, Geosystems* 20, pp. 1202–1217.
- Szeliga, W., T. I. Melbourne, M. M. Miller, and V. M. Santillan (2004). "Southern Cascadia episodic slow earthquakes". In: *Geophys. Res. Lett.* 31, p. L16602.
- Szeliga, W., T. Melbourne, M. Santillan, and M. Miller (2008). "GPS constraints on 34 slow slip events within the Cascadia subduction zone, 1997–2005". In: *J. Geophys. Res.* 113, B04404.
- Thomas, A. M., R. M. Nadeau, and R. Bürgmann (2009). "Tremor-tide correlations and near-lithostatic pore pressure on the deep San Andreas fault". In: *Nature* 462, pp. 1048–1051.
- Thomas, A. M., R. Bürgmann, D. R. Shelly, N. M. Beeler, and M. L. Rudolph (2012). "Tidal triggering of low frequency earthquakes near Parkfield, California: Implications for fault mechanics within the brittle-ductile transition". In: *Journal of Geophysical Research* 117, B05301.
- Todd, E. K. and S. Y. Schwartz (2016). "Tectonic tremor along the northern Hikurangi Margin, New Zealand, between 2010 and 2015". In: *J. Geophys. Res. Solid Earth* 121, pp. 8706–8719.
- Van Decar, J. C. and R. S. Crosson (1990). "Determination of teleseismic relative phase arrival times using multi-channel cross-correlation and least squares". In: *Bulletin of the Seismological Society of America* 80.1, pp. 150–169.
- Wech, A. G. (2010). "Interactive tremor monitoring". In: *Seismol. Res. Lett.* 81.4, pp. 664–669.
- (2016). "Extending Alaska's plate boundary; tectonic tremor generated by Yakutat subduction". In: *Geology* 44.7, pp. 587–590.
- Wech, A. G. and K. C. Creager (2007). "Cascadia tremor polarization evidence for plate interface slip". In: *Geophysical Research Letters* 34, p. L22306.

- Wech, A. G. and K. C. Creager (2008). "Automated detection and location of Cascadia tremor". In: *Geophysical Research Letters* 35, p. L20302.
- (2011). "A continuum of stress, strength and slip in the Cascadia subduction zone". In: *Nature Geoscience* 4, pp. 624–628.
- Wei, M., J. J. McGuire, and E. Richardson (2012). "A slow slip event in the south central Alaska Subduction Zone". In: *Geophys. Res. Lett.* 39, p. L15309.
- Wessel, P. and W. H. F. Smith (1991). "Free software helps map and display data". In: *EOS Trans. AGU* 72, p. 441.